2007-12-20

An Airborne Investigation of the Atmospheric Boundary Layer Structure in the Hurricane Force Wind Regime

Jun Zhang
University of Miami, jun.zhang@rsmas.miami.edu

UNIVERSITY OF MIAMI

AN AIRBORNE INVESTIGATION OF THE ATMOSPHERIC BOUNDARY LAYER STRUCTURE IN THE HURRICANE FORCE WIND REGIME

By

Jun Zhang

A DISSERTATION

Submitted to the Faculty
of the University of Miami
in partial fulfillment of the requirements for
the degree of Doctor of Philosophy

Coral Gables, Florida

December 2007

UNIVERSITY OF MIAMI

A dissertation submitted in partial fulfillment of
the requirements for the degree of
Doctor of Philosophy

AN AIRBORNE INVESTIGATION OF THE ATMOSPHERIC BOUNDARY LAYER STRUCTURE IN THE HURRICANE FORCE WIND REGIME

Jun Zhang

Approved:

_____ Dr. William M. Drennan Associate Professor of Applied Marine Physics	_____ Dr. Terri A. Scandura Dean of the Graduate School
_____ Dr. Hans C. Graber Professor of Applied Marine Physics	_____ Dr. Shuyi S. Chen Professor of Meteorology and Physical Oceanography
_____ Dr. Peter G. Black NOAA Scientist, Hurricane Research Division	

ZHANG, JUN (Ph.D., Applied Marine Physics)
An Airborne Investigation of the Atmospheric Boundary Layer Structure in the Hurricane Force Wind Regime
(December 2007)

Abstract of a dissertation at the University of Miami.

Dissertation supervised by Professor William M. Drennan.
No. of pages in text. (149)

As part of the ONR sponsored Coupled Boundary Layer/Air-Sea Transfer (CBLAST) experiment, data from the NOAA WP-3D research aircraft measurements into major Hurricanes in the 2002-2004 seasons are analyzed to investigate the structure of the boundary layer. The turbulent fluxes of momentum and enthalpy are derived using the eddy correlation method. For the first time, the momentum and enthalpy fluxes were directly measured in the boundary layer of a hurricane with wind speeds up to 30 m/s. A new bulk parameterization of the momentum and enthalpy flux is developed.

The vertical structure of turbulence and fluxes are presented for the entire boundary layer in the rain free region between the outer rainbands. The turbulent kinetic energy budget was estimated for the hurricane boundary layer between the outer rainbands. The universal spectra and cospectra of the wind velocity, temperature and humidity are also derived. A case study on the effects of roll vortices on the turbulent fluxes is conducted, which confirmed the existence of the boundary layer rolls and gave the first estimate of their modulation of the momentum and sensible heat flux.

The CBLAST data provided an invaluable perspective on the evaluation and development of the boundary layer parameterization suited for the hurricane models.

Studies on entrainment processes above of the mixed layer and turbulent transport processes induced by the inflow are recommended in the future.

Acknowledgements

I would like to acknowledge the UM Fellowship for providing me the financial support during my first 3 years graduate studies at University of Miami – RSMAS. And I want to thank ONR (N00014-01-F-009) for the support of CBLAST, NASA (work order W-19-835) for additional support, and NOAA-OAR (NA17RJ1226) for providing funds for the LICOR instrument. Also I want to thank all the scientists and workers of NOAA-AOC and NOAA-HRD who supported the CBLAST flight measurements, especially Drs. Frank Marks, Eric Uhlhorn, Mark Powell, John Gamache, and Chris Landsea.

I want to thank Dr. Hans Graber and Dr. Shuyi Chen for their comments and suggestions in my dissertation and for being part of my committee. I also want to thank Dr. Peter Black for his endless guidance as the outside committee member.

Many thanks to the AMP division's faculty, students and staff who provided an excellent environment for my study here. Especially, I want to thank Cyril McCormick, the electronic engineer, for his assistance. And I want to thank Dr. John Wang for being my advisor for the first year of my study at RSMAS.

I also want to acknowledge my colleagues and advisors including Drs. Mark Donelan, Jeff French, Brian Haus, Susanne Lehner, Kristina Katsaros, Edward Walsh, Tim Dunkerton, and David Nolan, for their help and guidance.

Especially I want to thank my advisor Dr. William M. Drennan for his countless hours of guidance, patience and scientific help throughout the years of my study. I am very lucky to be a student of Dr. Drennan, and I'll appreciate his help and guidance all my life.

Finally, I would like to thank my parents for giving me love and education, and my brother for his support. And all my work is dedicated to my wife Yuhui Wen for her endless love and support.

Table of Contents

List of Tables viii

List of Figures ix

CHAPTER 1. INTRODUCTION 1

1.1 Motivation and background……..……. 1

1.2 Review of literature 10

1.2.1 Air-sea interaction in hurricanes…….. 10

1.2.2 Modeling studies of the hurricane boundary layer……... 13

1.2.3 Observations of the hurricane boundary layer structure……... 17

1.2 Objectives of this study ...……. 20

CHAPTER 2. DESCRIPTION OF EXPERIMENT AND DATA 23

2.1 Introduction ……. 23

2.2 Flight patterns…….. 24

2.3 The instrumentation……. 28

2.4 Data collection and analysis method……..... 36

2.4.1 The data…… 36

2.4.2 Analysis methods……. 38

CHAPTER 3. TURBULENT FLUXES 41

3.1 Introduction ……..... 41

3.2 Turbulent fluxes and bulk parameterization ……. 43

3.2.1 Momentum flux..... 47

3.2.2 Latent heat flux……. 52

3.2.3 Sensible heat flux…….. 55

3.2.4 Enthalpy flux…… 57

3.3 Error analysis for the turbulent flux measurement…… 61

3.4 Variability of surface fluxes……..…… 65

CHAPTER 4. ROLLS 75

4.1 Introduction …… 75

4.2 Satellite RADARSAT-1 SAR observation …… 78

4.3 Aircraft observations…….. 81

4.3.1 The study case of rolls…… 81

4.3.2 Evidence of rolls……. 85

4.3.3 Spectral analysis……. 89

4.4 Discussion…… 93

CHAPTER 5. VERTICAL STRUCTURE OF TURBULENCE 96

5.1 Introduction …… 96

5.2 Vertical structure of turbulence and flux…… 97

5.2.1 Scaling…… 97

5.2.2 Vertical profiles of turbulent fluxes..……. 100

5.2.3 Vertical profiles of variances..…… 103

5.3 Characteristics of spectra and cospectra…...…….. 108

5.3.1 Spectra and cospectra……. 108

5.3.2 Universal shape spectra and cospectra……..... 113

CHAPTER 6. TKE BUDGET 121

6.1 Introduction …… 121

6.2 Height dependence of terms in TKE budget…….. 124

6.2.1 Mechanical production ……. 124

6.2.2 Buoyancy production …… 125

6.2.3 Dissipation ……..... 126

6.2.4 The TKE transport …… 127

6.3 The TKE budget ……... ……. 128

CHAPTER 7. SUMMARY OF CONCLUSIONS 130

7.1 Conclusions……. 130

7.2 A conceptual model for the hurricane boundary layer height…… 132

7.2 Future work …… 137

BIBLIOGRAPHY 138

List of Tables

3.1 Summary of data and calculations from 128 flux runs in seven storms..... 44

4.1 Summary of data and calculations for the five flux run legs..... 85

List of Figures

1.1 Dalton number versus 10m neutral wind speed for 5 field experiments…. 4

1.2 Drag coefficient versus 10m neutral wind speed for 8 field experiments... 5

1.3 Laboratory measurements of the neutral stability drag coefficient…… 6

1.4 Surface momentum exchange coefficient as a function of U_{10}……..... 7

2.1 CBLAST survey pattern showing planned expendable probe deployments ...……. 25

2.2 Vertical alignment of planned stepped descent legs..... 26

2.3 Track of N43RF into Hurricane Isabel on 20030914…….. 27

2.4 Sketch of NOAA WP-3D research aircraft instrumentation……... 29

2.5 LICOR package (white box) inside aircraft radome…… 30

2.6 LICOR vapor flux package……..…… 31

2.7 Comparison of absolute humidity from the LI-7500 and slow response aircraft thermistor and chilled-mirror hygrometer system……... 33

2.8 Plot of radiometric sea surface temperature versus altitude for two stepped descents on 12 September…….. 34

2.9 Time series of aircraft altitude, attitude angles (pitch, roll and heading), the three components of the wind vector (u, v and w), and the absolute humidity (measured from the LICOR) for the total flux run period of 02 Sep. 2003……. 38

2.10 Spectra and cospectra of the three components of the wind vector and humidity..... 39

3.1 Total covariance as a function of altitude for twelve individual stepped descents. ……..……. 48

3.2 A comparison of profile-derived and SFMR measured 10-m winds..... 51

3.3 Plot of drag coefficients as a function of wind speed..... 52

3.4 Plot of $\overline{w'q'}$, covariance of specific humidity with vertical velocity, versus altitude z for CBLAST stepped descents..... 53

3.5 Plot of Dalton number vs wind speed, both neutral 10 m..... 54

3.6 Plot of $\overline{w'\theta'}$, covariance of potential temperature with vertical velocity, versus altitude z for CBLAST stepped descents. 55

3.7 Sensible heat flux $\overline{w'\theta'}$ as a function of $U_{10N}(\Theta_0 - \Theta_{10N})$..... 56

3.8 Plot of 10-m neutral Stanton number as a function of 10-m neutral wind. 57

3.9 Plot of the specific enthalpy flux versus altitude z for CBLAST stepped descents. 58

3.10 Plot of 10-m neutral exchange coefficient of enthalpy as a function of 10-m neutral wind..... 59

3.11 Wind speed dependence of C_K/C_D..... 60

3.12 CBLAST stepped descent flight patterns flown in Hurricanes Fabian and Isabel in 2003, plotted in storm-relative coordinates 66

3.13 Vertical profiles of the buoyancy flux. 67

3.14 SST derived from AVHRR satellite, ARGOS buoys, and P3 radiometer.. 68

3.15 Variability of enthalpy flux by storm quadrant..... 69

3.16 Coupled model simulated enthalpy flux by storm quadrant..... 70

3.17 Variability of the friction velocity by storm quadrant..... 72

3.18 Variability of the drag coefficient by storm quadrant..... 72

3.19 Wind direction versus wind stress direction..... 73

4.1 Schematic depicting hurricane boundary layer rolls observed during four hurricane landfalls..... 76

4.2 RADARSAT-1 SAR image of Hurricane Isidore acquired on 23 September 2002 at 23:57 UTC after landfall on the Yucatan Peninsula..... 79

4.3 Analysis result of the SAR image in Fig. 4.2 …… 80

4.4 P3 N43RF aircraft track on top of the GOES-8 visible image…… 82

4.5 Specific humidity (left) and potential temperature (right) from 6 GPS dropsondes dropped from N43RF in the vicinity of the 22 September 2002 boundary layer flight……... 83

4.6 N43RF flight track during Hurricane Isidore on 22 Septermber 2002, 22:10-22:42 UTC, the aircraft altitude, pitch and roll, wind speed and wind direction ……..…… 84

4.7 Time series of the bin-averaged (1 Hz) fluctuations of three dimensional wind velocities, potential temperature and specific humidity and productions of the fluctuations…… 86

4.8 Spectra of velocity, potential temperature and humidity for leg A ……..… 87

4.9 Contour plots of wavelet coefficient amplitude of the vertical velocity against time and frequency…….. 88

4.10 For the cross-wind leg A, Cospectra of the vertical velocity w with the horizontal wind velocity components u and v, potential temperature and humidity …….. 90

4.11 Cumulative cospectral sum of the alongwind and crosswind components of the momentum flux for the N43RF boundary layer flight…….. 91

4.12 Cumulative cospectral sum of the sensible heat flux……...…..…….…. 92

5.1 Schematic diagram showing idealized limits of validity of certain scaling techniques…… 99

5.2 Dimensionless profiles of the coviances of uw and vw ……. 101

5.3 Normalized profiles of the coviances of qw and θw…….. 102

5.4 Dimensionless profiles of velocity variances……..……... 105

5.5 Vertical profiles of variances of temperature and humidity normalized by the mixed layer height…….…… 107

5.6 Vertical variation of the spectra of the vertical velocity and along wind component wind velocity……..…….…. 109

5.7 Vertical variation of the spectra of the specific humidity and potential temperature……..…… 110

5.8 Vertical variation of the cospectra of the alongwind and crosswind component momentum flux……. 111

5.9 Vertical variation of the cospectra of the humidity and sensible heat flux……... 112

5.10 Curves of universal spectra of the three dimensional wind velocities in the scaling of Miyake et al. (1970)…….……. 115

5.11 Curves of universal spectra of humidity and potential temperature…… 117

5.12 Curves of universal cospectra of the alongwind and crosswind component momentum flux……. 118

5.13 Curves of universal cospectra of the humidity and sensible heat flux……. 120

6.1 Vertical profiles of the shear production……..... 124

6.2 Vertical profiles of the buoyancy production…….. 125

6.3 Vertical profiles of the rate of dissipation……..…..…… 126

6.4 Vertical profiles of the TKE flux……. 127

6.5 Vertical profiles of shear production, buoyancy, turbulent transport, rate of dissipation and the residual term of the TKE budget ……. 128

7.1 A conceptual model for the hurricane boundary layer height between the rainbands…….. 134

7.2 A conceptual model for the hurricane boundary layer height varying with storm radius…….. 136

Chapter 1

Introduction

1.1 Motivation and Background

Tropical cyclones interact with the ocean through the boundary layer, obtaining heat and moisture, and transferring momentum to the ocean in the form of currents and waves. An improved knowledge of mechanisms underlying air-sea exchange across the boundary layer is essential for interpreting physical, dynamical and thermal-dynamical processes, and hence for the development of models with realistic prognostic capabilities for forecasting or simulating tropical cyclones. However, the tropical cyclone boundary layer has been the least well-observed part of the storm until now due to the lack of insitu measurements, because it is an extremely difficult environment for aircraft reconnaissance operations and surface based instrumentation to obtain direct measurements of the boundary layer structure due to safety requirements.

There has been no direct aircraft turbulence measurement in the boundary layer of a hurricane or a tropical storm since the measurements of Moss and Merceret (1976, 1977) and Moss (1978) who conducted one stepped descent and measured momentum fluxes at different levels in the boundary layer of the periphery of Tropical Storm Eloise. There have been measurements of the boundary layer structure by airborne radars (Powell, 1990

a, b), but the vertical resolution of them is limited by the sea clutter and instrumentation resolution. Because of inadequate observational coverage, modelers have typically extended physical parameterizations far beyond their validated regime, and little detailed analysis of full-physics model results within the boundary layer has been carried out (Kepert, 2006).

The atmospheric boundary layer is essentially the region of the atmosphere near the surface where the influence of the surface is felt through turbulent exchange of momentum and enthalpy. The boundary layer depth is often defined as the layer near the surface that is almost continuously turbulent (Stull, 1988). The kinetic energy of the large-scale atmospheric circulations cascades down to mesoscale and smaller scale eddies through shear instability. The large range of scales associated with the mechanisms of air-sea exchange across the boundary layer necessarily requires such processes in numerical models to be parameterized. Unless model parameterizations of the surface flux and boundary layer turbulence are complete and well founded, the models will have limited predictive capability under hurricane intensity change.

It has been demonstrated that hurricane intensity in both idealized, axisymmetric, quasi-balanced models (Emanuel, 1995) and "full-physics" nonhydrostatic models (Braun and Tao, 2000) exhibits significant sensitivity to the ratio of the bulk exchange coefficient for enthalpy flux (C_K) to the exchange coefficient for momentum (C_D). Based on the comparison of model predictions with observations of the hurricane intensity for a number of hurricanes, Emanuel (1995) concluded that the ratio C_K/C_D lies in the range 1.2-1.5 in the high wind regime and suggests 0.75 as a lowest threshold to ensure model consistency. Emanuel (1999) pointed out that numerical models are only able to

adequately model hurricane strength by imposing constraints on the turbulent flux of heat and momentum in high wind regimes. The theoretical analyses of Emanuel (2003) conclude that the current (pre 2003) parameterization of the bulk drag and enthalpy coefficients would preclude the existence of category four and stronger hurricanes. Note that the operational GFDL hurricane prediction model (Kurihara et al., 1998) takes the crude approach of using equal roughness lengths for scalars and momentum, which gives $C_K/C_D = 1$.

The air-sea interface fluxes of momentum, sensible heat and latent heat are the most important boundary condition inputs for atmospheric, oceanic, and wave models, especially for the coupled models. Particularly, enthalpy flux plays a fundamental role as the energy source for hurricanes (Schade and Emanuel 1999). However, due to instrumentation limitations and problems with salt and sea spray, measurements of enthalpy flux have been difficult to obtain over the ocean. The data sets that have been published over the past 20 years are rare and show large scatter in plots of the Dalton number (C_E) as shown in Figure 1.1. It is found, based on the data sets available now, that there is no significant dependence on wind speed, so most studies have proposed constant Dalton numbers. In the same way, the bulk sensible heat flux coefficient (C_H), or Stanton number, has been found to take a constant value which is approximately equal to C_E, again independent of wind speed. Note that the bulk coefficient of enthalpy, C_K, is generally assumed to equal to C_E and C_H, which will be verified later in this thesis. The TOGA-COARE bulk flux algorithm (Fairall et al. 1996, 2003), which is generally regarded as the state of the art for parameterizing turbulent air-sea fluxes, has been tested only for 10-m winds up to about 18 m/s. Although the TOGA-COARE flux code and the

analysis by Liu et al. (1979), on which that code is based, suggest the parameterization is valid for higher winds, no analysis has verified this.

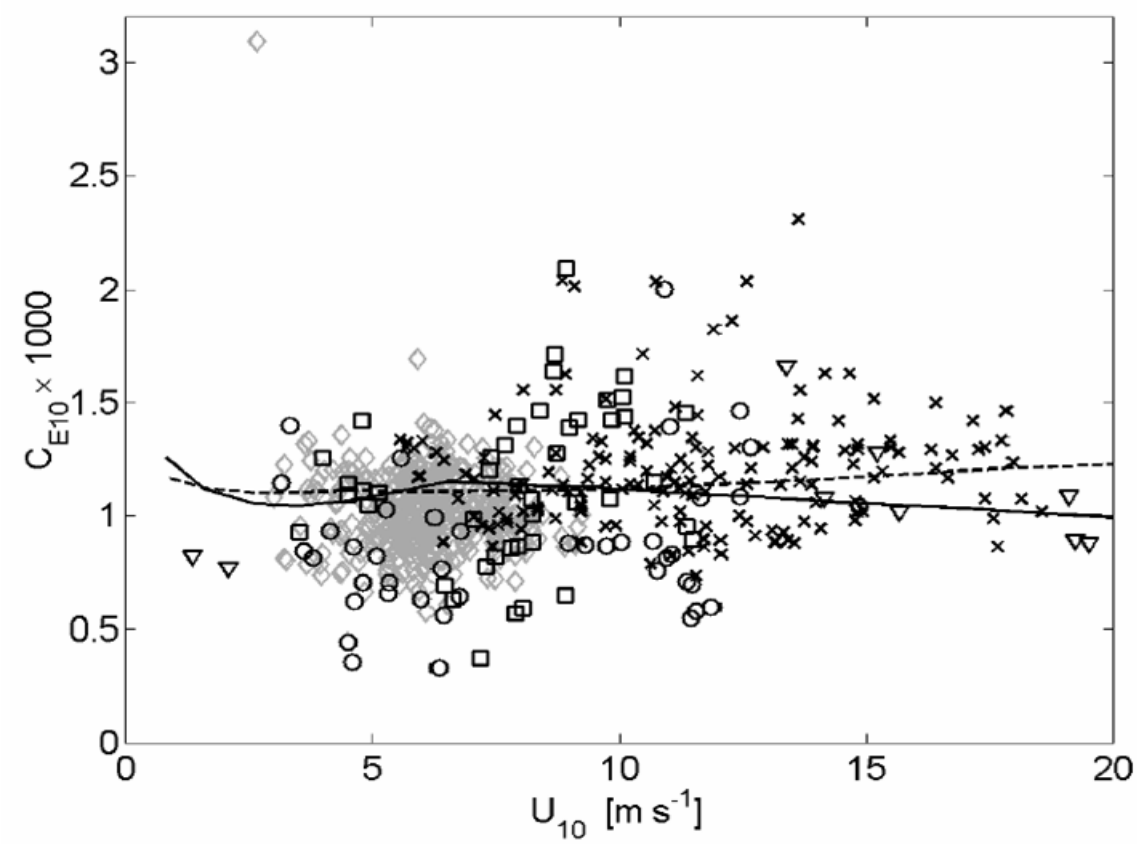

Fig. 1.1. Plot of Dalton number versus wind speed at 10-m height for neutral stability, from five field experiments. The experiments, all using the eddy-correlation method for measuring fluxes, are AGILE (o: Donelan and Drennan 1995), HEXOS (x: DeCosmo et al. 1996), GASEX (◊: McGillis et al. 2004), SOWEX (∇: Banner et al. 1999), and SWADE (□: Katsaros et al. 1993). Data have been corrected for density variations (Webb correction) and (as necessary) for salinity effects. The curves are from Fairall et al. (1996, solid), and Fairall et al. (2003, dashed).

During the past several decades, there have been a much larger number of momentum flux measurements over the sea. The drag coefficients shown in Fig. 1.2, an ensemble from eight field experiments, are typical of most recent campaigns. The experiments are from the small ship R/V *Agile* in Lake Ontario (Donelan and Drennan

1995); Adverse Weather Experiment (AWE), from an Air–Sea Interaction Spar (ASIS) buoy off the Florida coast (Drennan and Shay 2006); flux, état de la mer, et télédétection en conditions de fetch variable (FETCH), from an ASIS buoy in the Mediterranean Sea (Drennan et al. 2003); The Equatorial Pacific Air–Sea CO2 Exchange Experiment (GASEX), from an ASIS buoy (McGillis et al. 2004); HEXOS, from a tower in the North Sea (Smith et al. 1992; Janssen 1997); Risø Air–Sea Exchange (RASEX), from a tower in the Baltic Sea (Johnson et al. 1998); Surface Wave Dynamics Experiment (SWADE), from a ship in the coastal Atlantic (Donelan et al. 1997), and Water–Air Vertical Exchange Study (WAVES), from a tower in Lake Ontario (Drennan et al. 1999).

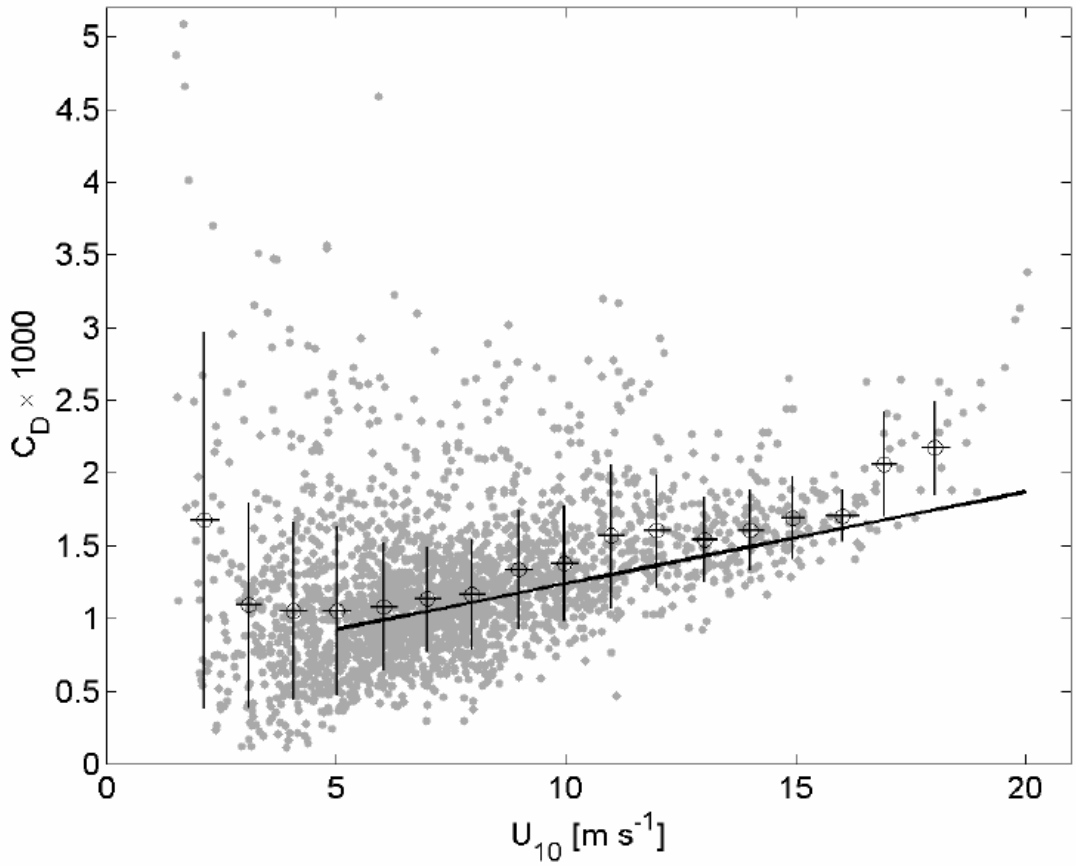

Fig. 1.2. Plot of drag coefficient versus wind speed at 10-m height for neutral stability, from eight field experiments. The experiments, all using the eddy-correlation method for measuring fluxes, are listed in the text. The curve is from Smith (1980). The circles and thin lines show the mean and 1 standard deviation of the data in bins of 1 m s^{-1}.

Although there is again considerable scatter in Fig. 1.2, most data sets show a significant increase in the momentum exchange (drag) coefficient with the 10 m wind speed. The relationship of Smith (1980) between C_D and U_{10}, $1000 \times C_D = 0.063 U_{10} + 0.61$, where both C_D and U_{10} have been adjusted to neutral stability, is representative of most open ocean data sets (e.g. Yelland et al., 1998). The drag is predicted to increase linearly with wind speed, with $C_D \approx 0.0019$ at 20m/s wind speeds. At these wind speeds, the ratio $C_K / C_D \approx C_E / C_D \approx 0.6$, well below the lowest bound proposed by Emanuel (1995).

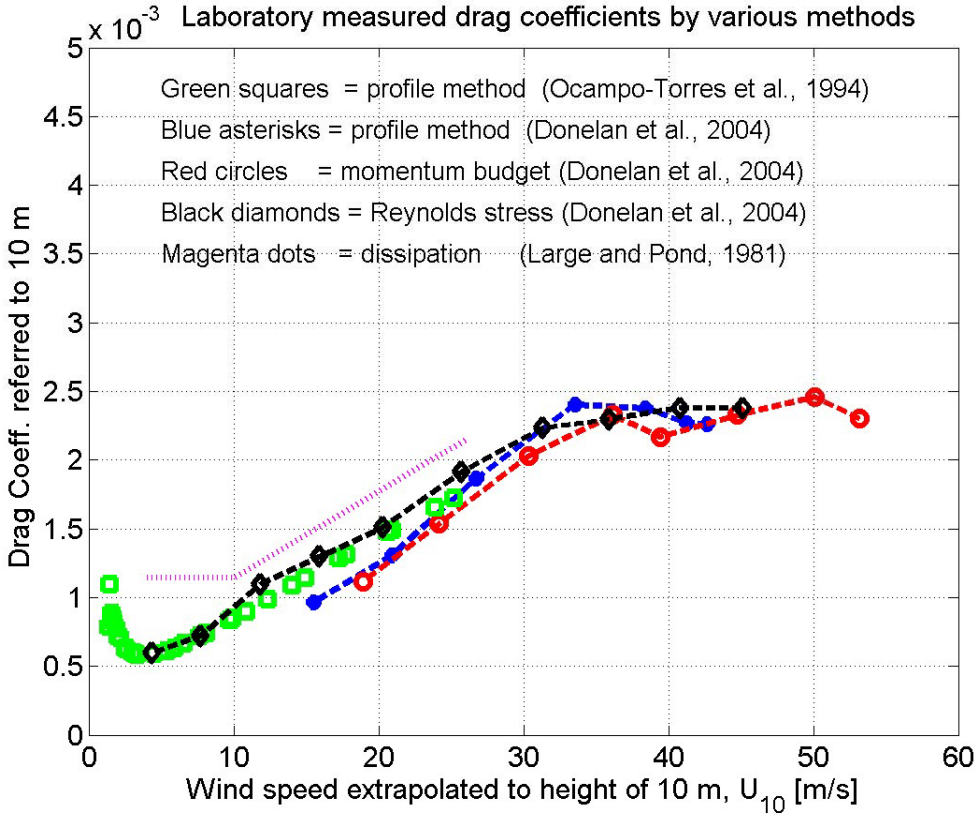

Fig. 1.3. Laboratory measurements of the neutral stability drag coefficient by profile, eddy correlation ("Reynolds") and momentum budget methods. The drag coefficient refers to the wind speed measured at the standard anemometer height of 10 m. The frequently cited drag coefficient formula of Large and Pond (1981) is also shown (See Donelan et al., 2004).

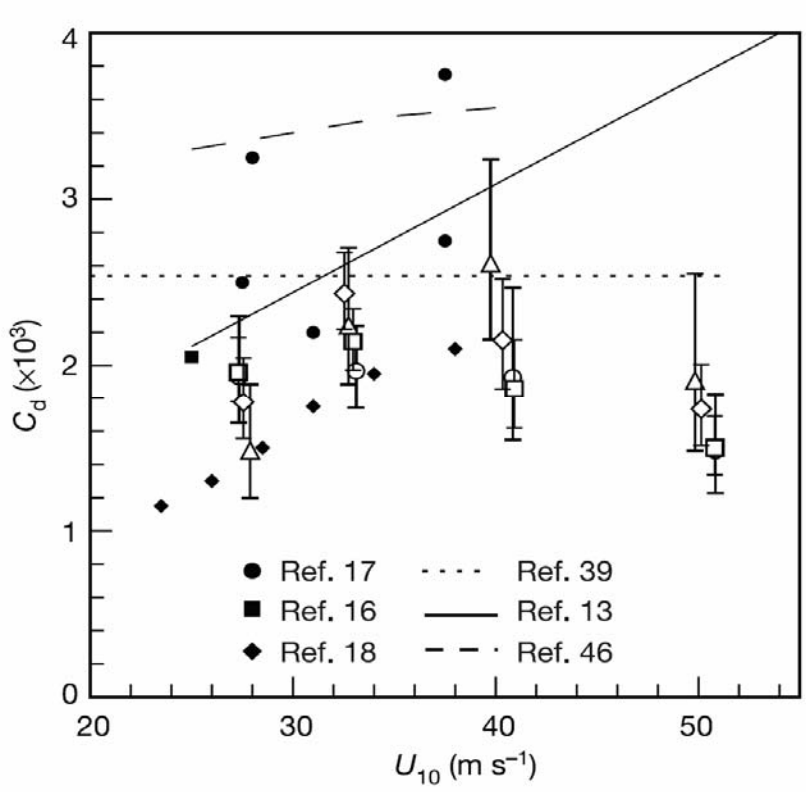

Fig.1.4. Surface momentum exchange coefficient as a function of U_{10}. Vertical bars represent the range of estimates based on 95% confidence limits and symbols. Error bar covered data are from GPS dropsondes observations, Refs. 13 (Large and Pond, 1981), 16 (Palmen et al., 1957), 17 (Miller, 1964), 18 (Hawkins et al., 1968), 39 (Amorocho et al., 1980), and 46 (Shay 1999) represent relationships and values from tropical cyclone budget studies (see Powell et al., 2003 Fig. 3).

The Smith relation represents the result of near-fully developed wave conditions, but underestimates C_D in developing conditions. Drennan et al. (2003) showed that the drag coefficients are 30% larger than those predicted by the Smith relation during strongly forced Mistral winds in the Mediterranean Sea. There is now considerable evidence for a significant wave age enhancement of the drag coefficient (see Donelan 1990; Smith et al. 1992; Drennan et al. 2003). Given that the wave field associated with hurricanes tends to be underdeveloped (duration limited) this effect should decrease the

ratio C_K/C_D even further below the Emanuel threshold. However, recent laboratory work (Fig. 1.3) by Donelan et al. (2004) found C_D to reach a maximum at wind speeds around 35 m/s, then leveling off. The authors attribute this as due to increased sheltering of the wind behind steeper waves. These results support those of Powell et al. (2003) based on extrapolating GPS dropsonde profiles to the surface as shown in Fig. 1.4.

Cione et al. (2000) using observations from deep-water moored buoys in hurricanes, demonstrated that air temperature and theta-e (equivalent potential temperature) values diminish as the gale-force wind radius is reached when air flows toward the eye wall. While air temperature remains almost constant from the gale-force wind radius toward the eye wall, relative humidity increases from 85% to 95%, and theta-e increases by about 8K. Although sensible heat fluxes balance the heat loss due to adiabatic cooling, the latent heat increase only accounts for 50% of the flux required to raise theta-e by 8K. A similar result was found by Barnes and Bogner (2001) from GPS dropsonde observations in hurricane Bonnie. This implies a problem with the exchange coefficients, such as strong downward heat fluxes across the top of the ABL or another source of heating which has been proposed recently by Andreas and Emanuel (2001) in the form of sea spray. However, as noted by Wang et al. (2000), the Andreas spray parameterization results in a net warming of the atmospheric boundary layer, something that is not observed (Cione et al., 2000).

Furthermore, observations by Powell et al. (1999) from GPS dropsonde observations show that near hurricane principal rainband and eyewall regions, there are locations where a layer from the surface to 50-100 m exists consisting of constant specific humidity and wind direction, above which the humidity drops markedly. This

layer exists within a well-mixed, constant theta layer (layer of constant adiabatic lapse rate) for winds over 35 m/s. Barnes and Bogner (2001) hypothesized that the only explanation for this phenomenon is the existence of a layer of enhanced spray droplet concentrations. This is consistent with the model computations of Metsayer and Lefauconnier, (1988) and Rouault et al., (1991) which, in general, suggests that the layer of constant specific humidity grows from tens of cm at 7.5 m/s wind speeds to several meters at 15 m/s.

Coupled models (Chen et al., 2007) necessitate a clearer and more complete understanding of the physical processes at the air-sea interface. All coupled air-sea models depend on the specification of the exchange coefficients for the estimation of the transfer of momentum and enthalpy. One clear limitation of the observational results for C_E and C_D is that few direct flux data are available for wind speeds over 20 m/s. Hence most results are extrapolated well outside the range of observations for use in hurricane models. Given that several new physical processes, for instance sea spray, may dominate at much higher winds, such an extrapolation is not likely warranted. Clearly, there is a need for direct measurements of both momentum and enthalpy fluxes at high winds in order to develop a new bulk parameterization of those fluxes for the hurricane models. It is crucial to improve our understanding of what happens at the air-sea interface in winds above about 20 m/s, when the near-surface air is “too thick to breathe and too thin to swim in” (Kraus and Businger, 1994), and of the vertical mixing and energy transport processes within the hurricane boundary layer, in order to enhance the hurricane track and intensity forecasts.

1.2 Review of Literature

1.2.1 Air-Sea Interaction in Hurricanes

The central importance of the boundary layer on hurricane dynamics is highlighted in a series of papers by Emanuel (Emanuel 1986; Emanuel 1991; Emanuel 1995; Emanuel 1999). Following the earlier studies by Riehl (1954), Malkus and Riehl (1960), and Palmen and Newton (1969), Emanuel (1986) deduces that a tropical cyclone cannot be sustained simply by using the ambient convective available potential energy (CAPE). Additional energy extracted from the sea such as the latent heat is needed to drive the tropical cyclone heat engine. This energy enters into the tropical cyclone through the frictional boundary layer. The importance of the additional energy is highlighted by Rotunno and Emanuel (1987) who successfully simulated the intensification and maintenance of tropical cyclones in an environment devoid of CAPE. One conclusion from these studies is that the fundamental source of energy for tropical cyclones is heat transfer from the ocean. The mature tropical cyclone may be idealized as a steady, axisymmetric flow whose energy cycle is very similar to that of an ideal Carnot engine (Emanuel, 1986). The energy cycle of a mature tropical cyclone is one of isothermal expansion, adiabatic expansion, isothermal compression, and adiabatic compression.

Emanuel (1986, 1995), using an analytic model of the structure of mature cyclones, predicts the maximum azimuthal wind speed varies as a function of $(C_k/C_D)^{1/2}$ in the form:

$$\left|U_{\max}\right|^2 \approx \frac{C_k}{C_D}\frac{T_s - T_0}{T_0}\left(k_s - k\right) \tag{1.1}$$

where C_k is exchange coefficient of enthalpy, C_D is the surface drag coefficient, T_s is the sea surface temperature, T_0 is the temperature of the storm's outflow near the tropopause, k_s is the specific enthalpy of air at saturation at the sea surface temperature and pressure, and k is specific enthalpy of boundary layer air. Emanuel (1999) demonstrated that the intensity of many hurricanes can be accurately predicted using a very simple atmospheric model coupled to an essentially one-dimensional ocean model (Schade, 1997), as long as storms remain unaffected by other atmospheric influences such as environmental wind shear.

Equation (1.1) shows the sensitivity of the hurricane intensity to the sea surface temperature. The observed cooling of order 1 K under the storm core could have a significant feedback on hurricane intensity. Although the first simulation of a hurricane using a coupled ocean-atmosphere model by Chang and Anthes (1979) showed little effect of the ocean feedback on storm intensity, the recent study on the ocean feedback by Schade and Emanuel (1999) who used an advanced higher resolution coupled model showed that ocean feedback has a first-order effect on hurricane intensity. Upper ocean processes cause the SSTs to cool mostly through a combination of mixing and upwelling processes, which in turn alter available heat for the storm's maintenance. The sea surface temperature field under the tropical cyclone is often not uniform spatially. Cool wakes,

identified with airborne expendable bathythermographs (AXBTs) may result in little or no sensible heat being transferred to the inflow layer (Black and Holland 1995), while warm eddies may enhance the fluxes (Shay et al. 2001).

Bister and Emanuel (1998) discuss the possibility that viscous dissipation of turbulent kinetic energy in the surface layer could be an additional heat source for the tropical cyclone. Maximum dissipative heating would tend to occur in high winds near the eyewall where rain and spray may evaporate resulting in a latent heat input to the tropical cyclone.

The relation (1.1) also suggests a strong sensitivity of hurricane intensity to those boundary layer processes that determine the exchange of enthalpy and momentum with the ocean, and ocean temperature near the eyewall, which can strongly influence the magnitude of $k_s - k$. As k is not a free parameter, it is sometimes remarked that equation (1.1) is sensitive to the assumptions made of the value of the enthalpy k under the eyewall (Holland, 1997). However, Emanuel (1986, 1995) simplified the calculation of k at the radius of maximum winds by assuming that the boundary layer relative humidity is constant outside the radius of maximum winds and that k is equal to the saturated moist static energy just above the top of the boundary layer.

The predictions of (1.1) are in good agreement with numerical experiments, beginning with those by Ooyama (1969) and Rosenthal (1971) and continuing with many others in 1990s, in which the exchange coefficients are simply specified. Unfortunately, little is known about how these exchange coefficients behave at high wind speeds in nature. It is apparent that most of the entropy increases in the inflow near the eyewall where hurricanes are sensitive to the exchange coefficients. As discussed earlier,

measurements at low to moderate wind speeds suggest that the drag coefficient increases with wind speed, because of increased surface roughness, but the enthalpy exchange coefficient remains approximately constant; when extrapolated to hurricane wind speeds, this yields a ratio C_k/C_D too small to explain the observed intensity of hurricanes (Emanuel 1995; Emanuel, 2003). This suggests other physical processes must come to play to enhance the enthalpy exchange and/or diminish drag.

Andreas and Emanuel (2001) suggested that the relevant mechanism is re-entrant sea spray, which transfers significant amounts of enthalpy to the air. Recent estimates of the exchange coefficients from wave tank measurements (Donelan et al. 2004), from measurements of the ocean current response to tropical cyclones (Shay, 1999) and from wind profiles measured using dropsondes (Powell et al. 2003) suggests that the drag coefficient may level off in high winds. However, there is no direct measurement of momentum and enthalpy fluxes in hurricane winds to verify this.

1.2.2 Modeling Studies of the Hurricane Boundary Layer

There have been several attempts to study the boundary layer of a hurricane by prescribing the wind field at the top of the layer. Smith (1968) used a momentum integral method to calculate the induced vertical velocity at the top of the boundary layer of an axisymmetric vortex assuming the Ekman solution is valid at larger radii where the Rossby number is relatively small. Leslie and Smith (1970) and Bode and Smith (1975) revisited these calculations and found that the prescription of the eddy diffusivity is very

sensitive to the surface stress and surface roughness as a function of wind speed. Shapiro (1983) investigated the asymmetric boundary layer under a translating hurricane and found that the maximum convergence lies in the forward right quadrant in the northern hemisphere. Anthes and Chang (1978) studied the boundary layer structure of a mature hurricane in a time-dependent, axisymmetric numerical model with nine levels, six of which were in about the lowest kilometer, but the radial resolution of 60 km was relatively coarse. Montgomery et al. (2001) considered the effects of the boundary layer on vortex spin-down for particular initial distributions of azimuthal wind with radius. Kepert and Wang (2001) carried out high-resolution calculations of boundary layer structure in a model for both stationary and translating vortices and calculated the vertical structure of the boundary layer flow.

It should be noted that early hurricane models and some idealized studies assume a simple slab representation of the boundary layer. As mentioned above, Emanuel (1995b) used such a representation in theory for the maximum potential intensity of a tropical cyclone in which vertical advection was omitted. In another study, Willoughby (1990) used a balanced formulation that provides a diagnostic formula for the boundary layer inflow, but he did not investigate the accuracy of the approximation. However, Montgomery et al. (2006) showed that the Emanuel's theory does not include a critical aspect of the inner-core structure of mature hurricanes. They suggested that the 'turboboost'' mechanism, i.e., the net effect of the mean secondary and eddy circulation within the low level eye transporting and stirring high entropy air from the eye to eyewall, may play an important role in providing more power to tropical cyclones and explain how the maximum wind speed may exceed the previous upper bound for storms that lack

adverse environmental influences. Although in this study, the boundary layer structure near the eyewall is not the main concern, investigation of the smaller scale structure under the eyewall is challenging in the future.

The hurricane boundary layer wind field has been comprehensively studied especially on the development of the supergradient wind. That is to say the maximum tangential wind speed occurs in that layer rather than above it. Even if the tangential wind is not supergradient in the boundary layer, the maximum total wind speed may still exceed that above the layer. Anthes (1974) first suggested the development of supergradient winds in hurricanes. Shapiro (1983) found a region of supergradient winds in the inner core of an axisymmetric vortex boundary layer inside the radius of maximum wind speed above the layer. The recent high-resolution numerical solutions of the tropical boundary layer by Kepert and Wang (2001) found a strong radial jet in the core region in which the trangential wind speed was 10-25% supergradient. Nguyen et al. (2002) investigated the evolution of the boundary layer flow in an axisymmetric vortex model driven by buoyancy forces associated with moist convection and found the development of supergradient winds in the boundary layer.

Because of the lack of verifying observations, the boundary layer has received less theoretical attention than other parts of the tropical cyclone (Kepert, 2006). The one-dimensional model of Powell (1980) has been used to estimate near-surface winds from flight level observations. Two-dimensional axisymmetric models include the analytical model of Rosenthal (1962) and the numerical models of Anthes (1971), Eliassen and Lystad (977) and Montgomery et al. (2001). As mention above, Kepert (2001) and Kepert and Wang (2001) presented three-dimensional analytical and numerical models of the

tropical boundary layer, which resolve the vertical structure of the motion-induced asymmetry. Regarding the wind field, Kepert (2001) and Kepert and Wang (2001) made some potentially important predictions. They found that the ratio of the 10-m wind speed to that at some reference height in the free atmosphere increases from 0.6 to 0.7 in the outer core to 0.8 to 1.0 near the eyewall, and is greater on the left of the storm than on the right. They also found that the tangential wind in the upper boundary layer is slightly supergradient in the cyclone periphery and increasingly near the core depending on the storm intensity and structure. Using GPS dropsonde data, Kepert (2006) compared the simulated boundary layer flow in Hurricane Georges and that measured by the sondes, and found that the simulated wind profiles are in good agreement with the observations.

It should be noted that in the numerical models, most of the turbulent processes occur at subgrid scale and hence are not explicitly resolved by numerical models. Turbulent surface fluxes and vertical mixing are generally parameterized using different formulations of boundary layer processes. For example, boundary layer and surface layer schemes used in the Pennsylvania State University – National Center for Atmospheric Research (PSU-NCAR) fifth-generation Mesoscale Model (MM5; Dudhia, 1993; Grell et al., 1995) include a simple bulk aerodynamic PBL (Deardoff, 1972), the Blackadar PBL (Blackadar, 1976, 1979; Zhang and Anthes, 1982; Oncley and Dudhia, 1995), a version of the Medium-Range Forecast (MRF) model PBL (Hong and Pan, 1996), and a version of the PBL scheme of Burk and Thompson (1989) that is a Mellor-Yamada level-2.5 closure model including a prognostic equation for the turbulent kinetic energy.

In those PBL schemes, one of the crucial elements is the determination of the ABL height (h), because it is linked to the maintenance of low level clouds. If h is too

low, the boundary layer is decoupled from the cloud layer, which inhibits the vertical transport of turbulent kinetic energy, heat and moisture form the ocean surface to the could layer; on the other hand, if h is too high, cumulus clouds, rather than stratiform clouds would form. In the tropical cyclone boundary layer model, Kepert and Wang (2001) used the Mellor-Yamada scheme but defined the boundary layer depth using the inertial instability parameter. They found the boundary layer depth decreases from around 1.5 km at 2.5 times the radius of maximum winds to about 500 m in the inner core.

1.2.3 Observations of the Hurricane Boundary Layer Structure

Over the past 50 years, research and reconnaissance aircraft measurements have been the primary tools for the study of the hurricane kinematics structure, including Hawkins and Rubsam's (1968) analysis of multilevel aircraft data, Willoughby et al's (1982) description of concentric eyewalls, Jorgensen's (1984) schematic of the core of Hurricane Allen, and Marks and Houze's (1987) Doppler radars analysis of the tropical cyclone structure. However, very few insitu observations were conducted within the atmospheric boundary layer of a hurricane. Hence there is little information on the three-dimensional structure of the hurricane boundary layer.

Doppler radar has been widely used to study the kinematic structure of a hurricane, especially the hurricane rainband structure. Several rainband experiments were conducted in 1980s such as those by Barnes et al. (1983) and Barnes and Stossmeister (1986). Powell and Black (1984) showed the results from the rainband hurricane

planetary boundary layer experiment, indicating that the convective influence of a principal rainband may become more prominent at the downband or downwind end, where it could act as a barrier to the inflow of high theta-e air from the outer radii. Powell (1990a, b) presented the results of hurricane boundary layer experiments conducted in outer rainbands of Hurricanes Josephine (1984) and Earl (1986). He compared the precipitation and kinematic structures in these storms and found that the principal rainbands have common characteristic mesoscale and convective-scale features in the boundary layer. He pointed out that the boundary layer wind field is strongly affected by the rainband and confirmed that the convective downdrafts are capable of transporting cool, dry, low equivalent potential temperature air to the surface.

The recent studies of data from global positioning system (GPS) dropsondes (Hock and Franklin, 1999; Franklin et al., 2003) have provided a hitherto unprecedented observational coverage in the tropical cyclone boundary layer. Franklin et al. (2003) presented a statistical analysis of the surface wind factor, the ratio of the 10-m wind speed to that at some reference height in the free atmosphere, for dropsonde data from the 1997-99 Atlantic hurricane seasons. They showed that the surface wind factor is larger beneath the eyewall than at larger radii. Powell et al. (2003) used the same data as Franklin et al. to calculate drag coefficients in hurricane conditions and found that the drag coefficients increased with wind speed up to about 40 m s^{-1} but then decreased at higher winds. As mentioned earlier, most recently Kepert (2006) presented detailed analyses of the wind field structure and balance within the boundary layer of two intense hurricanes, Georges and Mitch of 1998, using the dropsonde data, and compared these analyses with the predictions of the tropical cyclone boundary layer model (Kepert and

Wang 2001) to provide explanations for observed structures. Despite all the progress, comprehensive observations of the hurricane boundary layer have been especially hard to obtain, in particular, of the small scale turbulent structures.

Due to the safety requirements, research aircraft measurements have been conducted mostly above 1500 m. The only experiment with turbulent flux measurements in the hurricane boundary layer was conducted by Moss and Merceret (1976) and Moss (1978) who investigated some turbulent properties of boundary layer in the periphery of a marginal hurricane. They used a hot-film anemometer to measure the high frequency streamwise wind component and a gust probe to measure the lateral and vertical wind speed components， and computed momentum fluxes during seven level legs at different altitudes from 85 m to 1213 m. Moss (1978) compared the surface stress extrapolated from the observed momentum flux profile with that calculated using the Deardorff (1972) boundary parameterization scheme in which the Charnock (1955) formula of the roughness length and drag coefficient is used, showing a good agreement between them. This implies that the derived surface momentum flux measured by Moss (1978) essentially agrees with the Smith (1980) parameterization. Moss also found that the momentum flux varnishes at the top of the mixed layer defined by the potential temperature profile. Note that the surface wind speed measured by Moss (1978) is around 20 m s^{-1}.

1.3 Objectives of this Study

All the work within the scope of this dissertation is included in the Hurricane Program of the Coupled Boundary Layer Air-sea Transfer (CBLAST) experiment sponsored by the Office of Naval Research, the NOAA Hurricane Research Division, NOAA Office of Atmosphere Research, United States Weather Research Program and the Ocean Winds program of the NOAA/NESDIS Office of Research and Applications. The main purpose of the hurricane component of CBLAST is "to improve the understanding of physical processes that critically regulate the coupling between the oceanic and atmospheric boundary layers in the complicated conditions of tropical cyclones where swell, sea spray and secondary boundary layer circulations play a significant roll". The long term goal of CBLAST is "to improve hurricane intensity and intensity change forecasting by developing improved bulk parameterizations of air-sea fluxes processes" (CBLAST experiment plan, 2003).

The main purpose of this dissertation is to investigate the mean and turbulence structure of the atmospheric hurricane boundary layer between the hurricane rainbands and to extend the parameterization of the turbulent fluxes up to hurricane force using data gathered during the CBLAST-hurricane experiment in 2002-2004. Measurements were conducted using the NOAA-AOC (Aircraft Operation Center) Orion WP-3D aircraft. Data were collected at several altitudes within the hurricane boundary layer to investigate the variability of the turbulent fluxes with height and the mechanisms responsible for their variability. GPS dropsonde data were also utilized to study the mean profiles of the

boundary layer together with the aircraft flight level in-situ measurements. The goals of this dissertation are divided as follows:

1) Investigate the mean and turbulence structure of the hurricane boundary layer between the rainbands;
2) Determine the fluxes of momentum and enthalpy using the eddy correlation method;
3) Scale the profiles of mean and turbulent flow according to the hurricane boundary layer depth and surface fluxes;
4) Study the influence of secondary flow circulations (roll-vortex coherent structures) on the turbulent structure and fluxes.
5) Study the spectra and cospectra characteristics related to the contributions of turbulent mixing due to the surface roughness, surface sensible heating/cooling, and latent heating;
6) Investigate the variability of surface fluxes by storm quadrant;
7) Extend the classical bulk parameterization of fluxes to hurricane force with stability correction;

The following work includes first, in Chapter 2, a description of the CBLAST mission and boundary layer modules, instrumentation and data analysis methods. Chapter 3 presents the experimental results of the first direct turbulent flux measurements in high winds up to hurricane force. Chapter 4 discusses the possible effects of the hurricane boundary layer rolls on the turbulent flux parameterization. In Chapter 5, the vertical structure of turbulence and turbulent fluxes are presented with the discussion of their variability. Observational results are also compared with those from fully coupled

atmosphere-wave-ocean model. Chapter 6 presents the turbulent kinetic energy budget for the rainfree region between the outer rainbands. The conclusions and the future work are given in Chapter 7.

Chapter 2

Description of Experiment and Data

2.1 Introduction

Aircraft have an extensive history of usage for meteorological research, nearly paralleling the history of meteorology (Lenschow, 1986). During the past several decades, the use of research aircraft to measure mean and turbulent winds and scalars such as temperature and humidity has been increasing, especially in hurricane research. That is because it is very difficult to use insitu platforms to measure the atmosphere boundary layer inside hurricanes over the ocean. The main advantage of an aircraft platform is its mobility. While an aircraft's mobility requires more accurate measurement and correction for aircraft motion, an aircraft can probe the entire depth of the boundary layer and measure along a path at any arbitrary angle with respect to the wind, compared to the fixed platforms which are limited to sampling air advected by wind.

Over the past 30 years, NOAA-AOC Orion WP-3D aircraft have played an important role in hurricane research (Aberson et al., 2006). In this study, P3 aircraft N43RF was employed to conduct the turbulent flux measurements. GPS dropsondes released from the P3 aircraft N42RF and N43RF provided the profiles of the mean

quantities including wind speed, temperature and humidity. The flight pattern description is presented in the following section. The instrumentation and data used in this study are shown in sections 3 and 4, respectively.

2.2 Flight Patterns

The CBLAST-hurricane experimental plan consisted of two major observational components: 1) airborne in-situ and remote sensing measurements into hurricanes by the two NOAA WP-3D aircraft and 2) air-deployed surface drifting buoys and subsurface profiling floats (Black et al., 2007). A third component for operational needs consisted of the hurricane synoptic surveillance program that occasionally provided simultaneous high-level NOAA G-IV jet aircraft flights deploying GPS dropsondes in addition to reconnaissance flights within the hurricane's inner core. Geostationary and polar orbiting satellites made additional remote sensing measurements in the hurricane's inner core and environment. Thus, the CBLAST-hurricane experiment can provide a valuable data base to study hurricane intensity changes.

The aircraft component of CBLAST had two modules: a) an aircraft stepped descent module and b) an inner-core survey module. The former was designed to focus on in-situ air-sea flux and spray measurements, while the latter was to focus on large-scale structure, eyewall flux budget measurements and documentation of internal dynamics. The centerpiece of this effort involved a multi-sonde sequence of 8-12 GPS dropsondes dropped from coordinated WP-3Ds flying concurrently at different altitudes

across the hurricane eyewall and eye. Figure 2.1 shows a schematic of a typical flight plan. Each module consisted of several options related to precise experimental patterns dictated by prevailing conditions and available time on station. For instance, the stepped descents (Fig. 2.2), down to as low as 70m above the sea, were only carried out in clear air conditions between rainbands. This study is concentrated on the measurements during the stepped descent module.

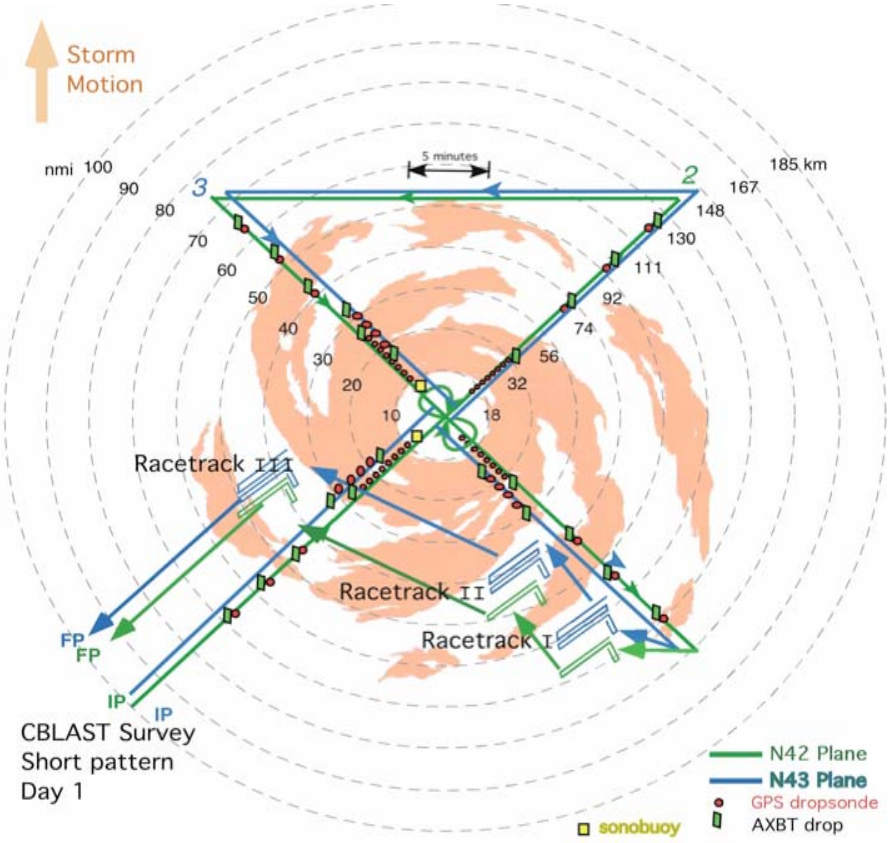

Fig. 2.1. CBLAST survey pattern showing planned expendable probe deployments along a pattern relative to the storm's eyewall and rainband features. Location of planned stepped-descent patterns to measure boundary layer fluxes are shown schematically. This idealized pattern is from the CBLAST experiment plan (http://www.aoml.noaa.gov/hrd/HFP2003/HFP2003.pdf). Actual flight patterns varied depending on flight conditions.

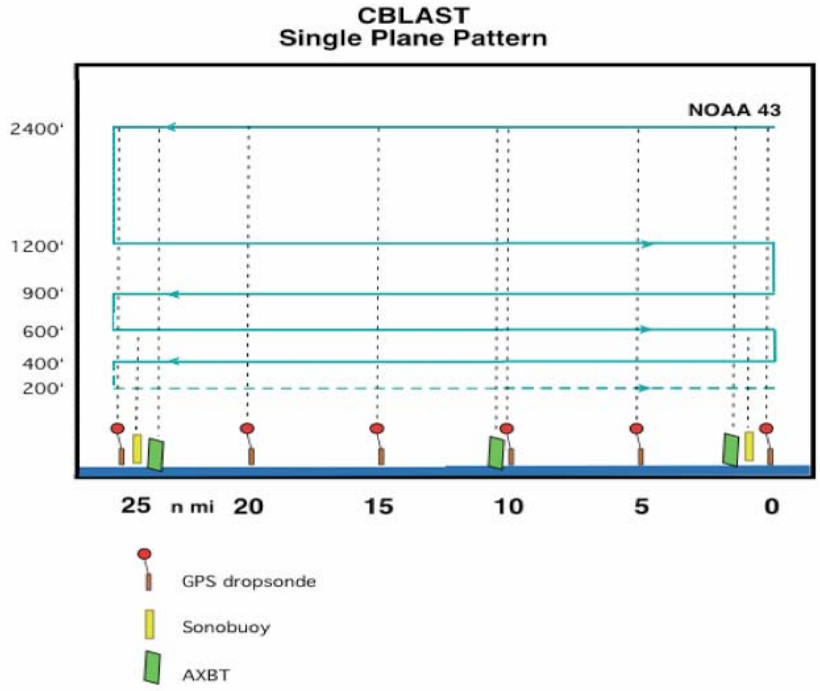

Fig. 2.2. Vertical alignment of planned stepped descent flight legs along with expendable probe location along the 25 nmi (40km) leg lengths. This figure is from the CBLAST experiment plan (http://www.aoml.noaa.gov/hrd/HFP2003/HFP2003.pdf). Actual flight patterns varied depending on flight conditions.

Compared to the planned flight pattern in Figs. 2.1 and 2.2, a typical flight pattern of real measurements is shown in Fig. 2.3. Consistent with the designed flight plan, each flight included an initial calibration (A), an eyewall penetration (B), and several stepped descents into the boundary layer (C). The example shown is for the 20030914 flight into Hurricane Isabel. On that day, Isabel was a strong category 4 hurricane, with maximum sustained winds around 140kts (72 ms^{-1}). The aircraft took off from St. Croix, US Virgin Islands, at 1450 UTC (1050 LT). After an initial descent (C1) was aborted due to poor visibility, along-wind and across-wind descents were made at C2, and an along-wind

descent at C3. Each stepped descent consisted of a series of ~25 km legs at nominal heights of 600, 400, 200, 120 and 60m. During many descents, the lowest altitude(s) was not reached due to the presence of clouds or rain.

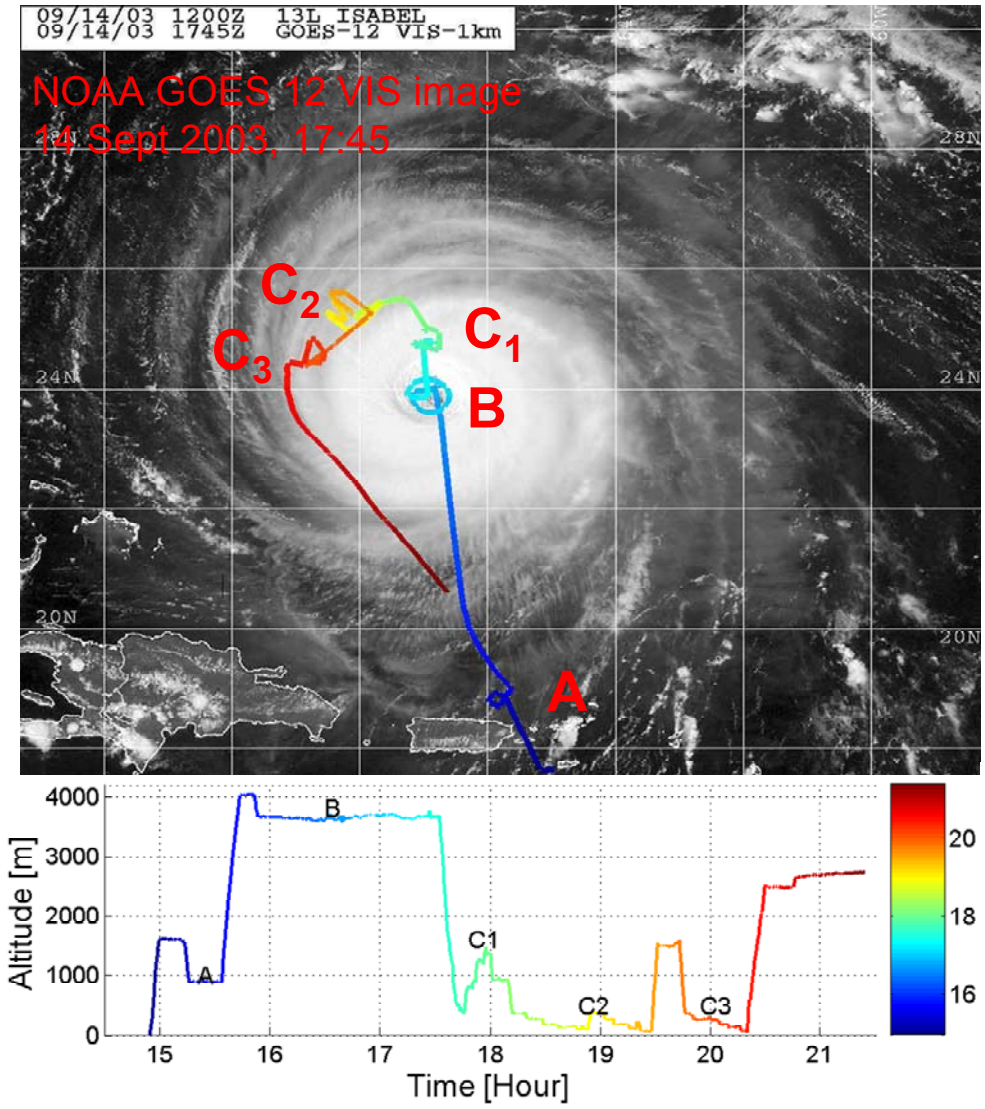

Fig. 2.3. Track of N43RF into Hurricane Isabel on 20030914. The highlighted features are (A) gust probe calibration, (B) eye penetration, and (C) stepped descents. The visible band image, from the NOAA GOES-12 satellite at 1745UTC, is coincident with (B). Image courtesy of Naval Research Laboratory, Monterrey.

2.3 The Instrumentation

The CBLAST-Hurricane experimental effort began in 2000 with the development of seven new airborne instrument systems, three new oceanographic float designs, 2 drifting buoy designs, the flight pattern strategy and the air-deployment strategy, including the WC-130J air-deployment certification and air-drop certification of 3 platform types (Black et al., 2007). The new airborne instrument systems were 1) Best Aircraft Turbulence (BAT) probe for fast response temperature and u-,v-,w-wind components, 2) a modified LICOR fast response hygrometer, 3) particle spectrometer and 4) Particle Doppler Analyzer (PDA) for sea spray droplet observation, 5) Scripps downward-looking, high-speed visible and infrared video camera systems for wave breaking observations, 6) Stepped and Simultaneous Frequency Microwave Radiometers (SFMR and USFMR) for surface wind speed and 7) the Integrated Wind and Rain Atmospheric Profiler (IWRAP) for continuous boundary layer and surface wind vector profiles. These systems were built in 2001 and flight- tested in 2002. Also deployed were three existing systems: 1) Tail (TA) Doppler radar for boundary layer wind structure, 2) Lower Fuselage (LF) weather radar for hurricane precipitation structure and 3) Scanning Radar Altimeter (SRA) for directional wave spectra.

For the CBLAST-Hurricane experiment, N43RF was instrumented with three independent systems for measuring aircraft-relative air velocity (Fig. 2.4): a 5-hole nose radome system (Brown et al. 1983; Khelif et al. 1999), a system consisting of two Rosemount 858Y probes and a pitot tube, and a NOAA Air Resources Laboratory (ARL) designed 9-hole BAT probe system (Crawford and Dobosy 1992; Hacker and Crawford

1999). Aircraft motions are monitored by an inertial navigation system (INS), which is corrected by comparison with a global positioning system (GPS) to remove the Schuler oscillations and long period drifts. The three-dimensional wind vector is computed by taking the vector sum of the aircraft-relative air velocity and the ground-relative aircraft velocity. The theory and algorithms used to derive the three dimensional wind velocities are provided in Zhang (2005).

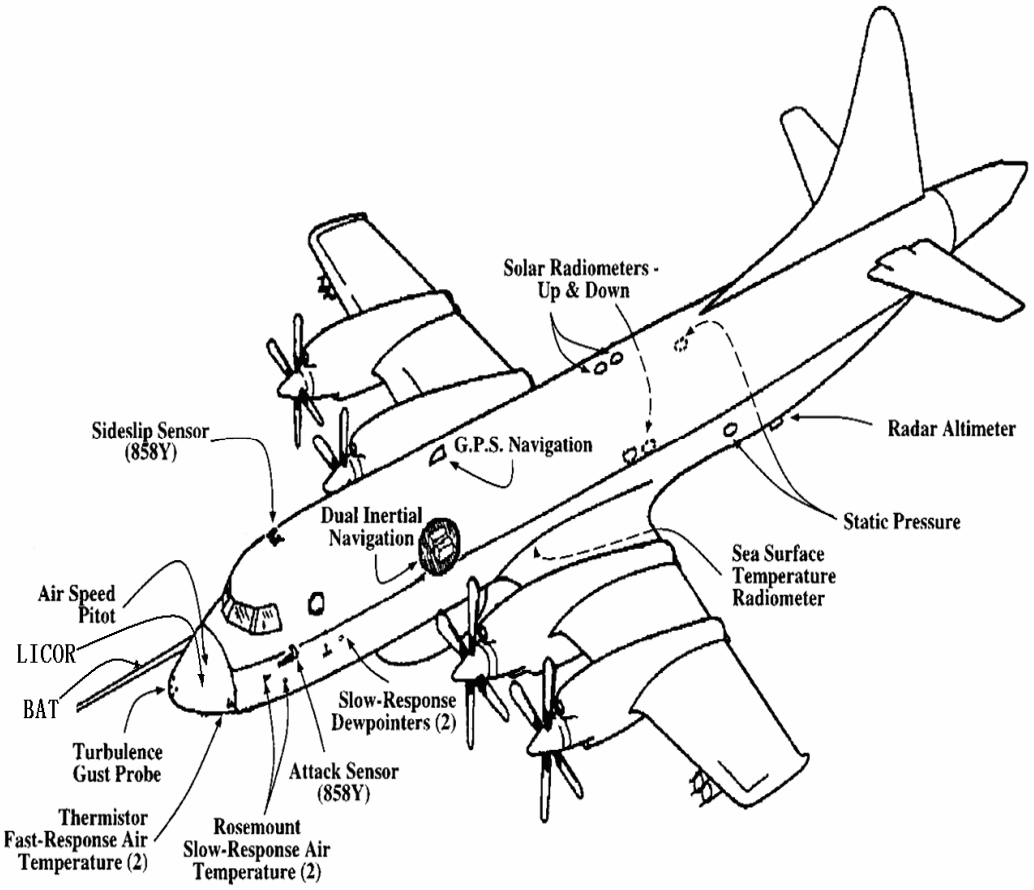

Fig. 2.4. Sketch of NOAA WP-3D research aircraft instrumentation (revised from Khelif et al., 1999, Fig.1, including LICOR and BAT but deleting fast Lyman-alpha hygrometer).

It is noted that the one of the pressure ports from the nose radome system leaked based on the data obtained during calibration maneuvers performed in advance of the 2003 measurement campaign. Further, examination of data from flux runs conducted after penetrations of regions of heavy rain indicate water intrusion into one or more the radome ports was common. Thus, for the remainder of the analysis, wind data will be presented only from the Rosemount system and the BAT probe.

Fast response humidity data are measured using a modified LICOR LI-7500 infrared gas analyzer enclosed in a box that was mounted behind the radome (Fig. 2.5). The LICOR was calibrated in its enclosure in the hanger or in the laboratory both before and after each field season using a LICOR LI-610 dew point generator. The box was put inside the radome so that it is nearly co-located with the gust probe for the purpose of surface flux measurements. Fig. 2.6 a) shows the three components of the LICOR package: LICOR 7500 infrared H_2O/CO_2 analyzer (white), a BEI Motion package including 3 rate gyros and 3 accelerometers (yellow box), and a pressure sensor used for diagnostics (silver).

Fig. 2.5. LICOR package (white box) inside aircraft radome.

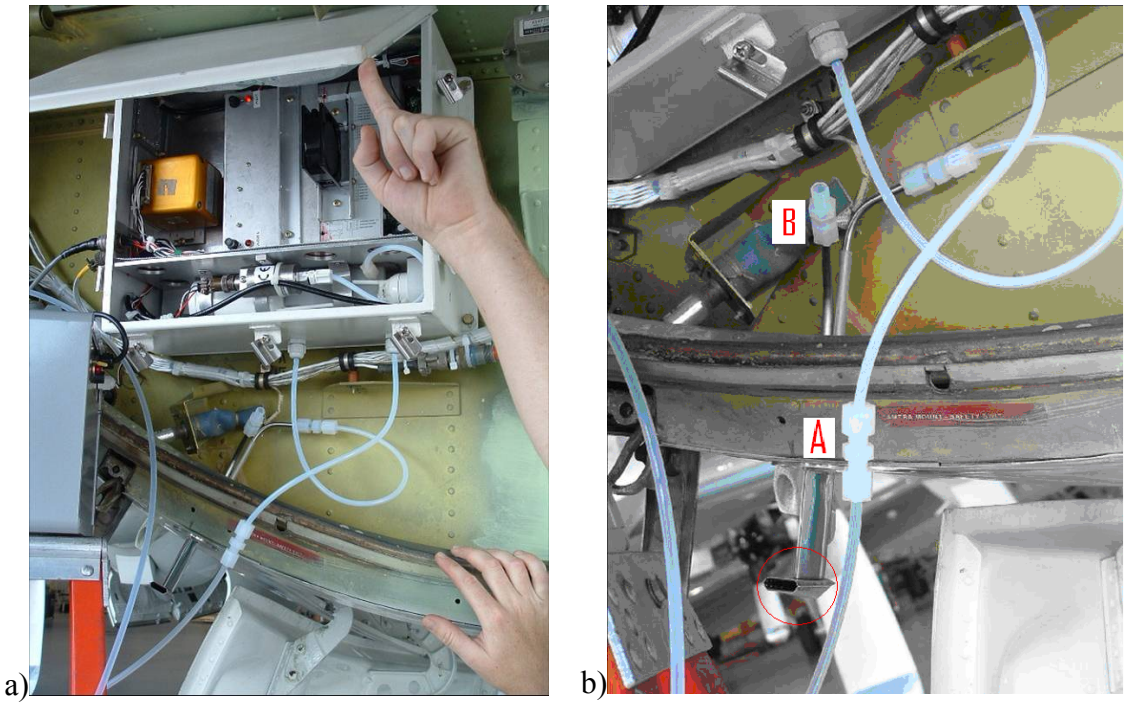

Fig. 2.6. LICOR vapor flux package, a). LICOR package components including LICOR 7500 infrared H2O/CO2 analyzer (white), BEI Motion package (yellow box), and pressure diagnostics (silver); b). Plastic tubes for air flow. The Rosemount 102E4 intake is circled in red. The picture shows the plumbing set up for calibration. For sampling the fittings A and B are connected.

As shown in Fig. 2.6 b), the air flows into LICOR hygrometer through a 1-m tube (6 mm in diameter) and then goes out after measurements. Airflow to the LI-7500 was provided via a Rosemount 102E4 housing (Goodrich Sensors) with a Buck Research IP-100 intake, and 70 cm long by 2-mm dia Teflon tubing. A low-density polyethylene (LDPE) insert with a 1.5-cm bore and ports near each end was mounted in the LI-7500 head to direct the airflow. A third port was connected to an Omegadyne PX-02K1 barometer allowing for the measurement of pressure within the chamber. The insert is similar in principal to the calibration tube provided by LI-COR, but is able to be secured in place against vibration. The aluminum enclosure, which also housed the LI-7500

electronics, was insulated (Orcotek 09–45015) and maintained at a constant 40°C temperature with two Minco Kapton HK-5177R58.8L12A thermofoil heaters, a Sunon SF11580 fan, and a Minco CT325PF2B5 controller. Both 120 V ac and 28 V dc power were provided to the enclosure. All channels from the enclosure (hygrometer, motion, and pressure) were sampled at 40 Hz using the aircraft data acquisition system installed for TOGA COARE. With typical airspeeds of 113 m s^{-1}, this corresponds to a sampling interval of 2.8 m.

The LICOR hygrometer (LI-7500) is a high performance, non-dispersive, open path infrared CO_2/H_2O analyzer designed for use in eddy covariance flux measurement systems. It can simultaneously measure CO_2 and H_2O in the free atmosphere. During each flight, the LI-7500 was checked against the humidity calculated from a slow-response thermistor and chilled-mirror hygrometer located along the fuselage aft of the cockpit and sampled at 1 Hz. Fig. 2.7 a shows a comparison of the two humidity signals from the LI-7500 and slow response aircraft thermistor and chilled-mirror hygrometer system, during the first two minutes of a typical flux run from1923:28 UTC 14 September 2003. Here the latter signal has been advanced by 2.5 s to account for both the slower instrument response and downwind position of the chilled mirror. The 2.5 s was determined from the phase lag between the two signals.

Fig. 2.7 b shows the comparison of absolute humidity from the 1-s LI-7500 and slow response aircraft thermistor and chilled-mirror hygrometer system during the full 7-h flight of 14 September 2003. There was little evidence of sea spray or rain affecting the LI-COR signal, despite the passage of the aircraft through regions of heavy rain: the Rosemount housing appears to be performing according to design by excluding most

droplets. The correlation between the two signals during the flight is $\gamma^2 = 0.993$; the best-fit linear regression between the two, $q_{dew} = 0.958 q_{LI} + 0.467$, is not significantly different from the 1:1 line. Neither the regression nor the correlation coefficient changed significantly during the six CBLAST flight days. Figure 2.7 c shows a comparison of the two humidity spectra during the flux run of Fig. 2.7 a. It is evident that the two signals agree well at frequencies lower than 0.3 Hz. At higher frequencies, the LI-7500 q' spectrum shows a well-defined inertial subrange, while the slow aircraft system spectrum rolls off.

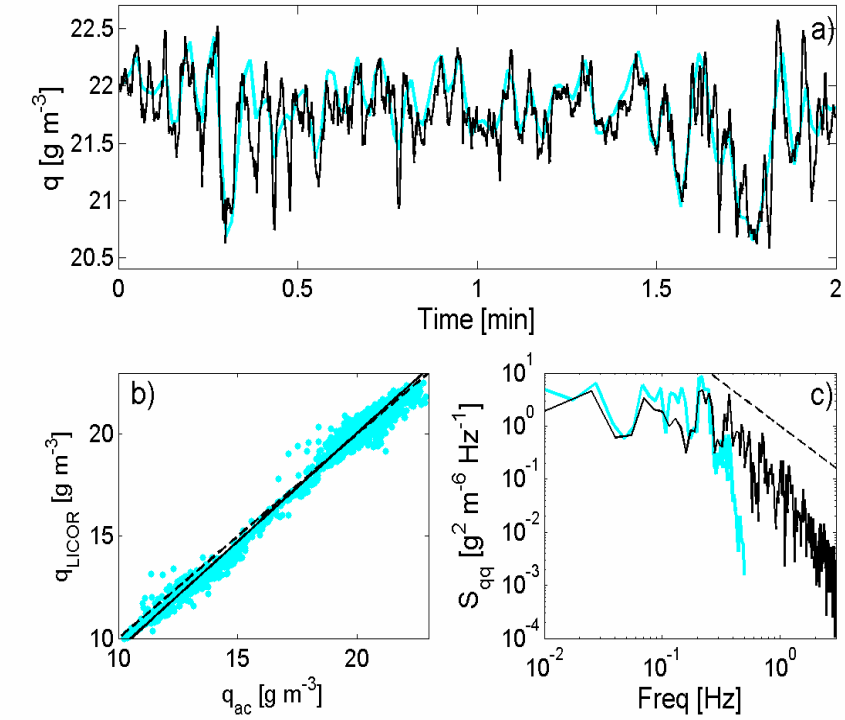

Fig. 2.7. Comparison of absolute humidity from the LI-7500 (black lines) and slow response aircraft thermistor and chilled-mirror hygrometer system (gray lines). (a) Two-minute time series comparison from 1923:28 UTC 14 Sep 2003. (b) Scatterplot of the 1-s data for the entire 7-h flight of 14 September; the dashed and solid lines are the best fit regression and 1:1 lines, respectively. (c) Frequency spectra from the flux run of (a); the dashed line shows the expected inertial subrange slope.

Fast response temperature data are measured using the Rosemount 102a sensors (Friehe and Khelif, 1992; Khelif et al., 1999). Sea surface temperature was measured from the P3s using a Barnes PRT-5 (precision radiation thermometer) radiometer. The PRT-5 operates in the narrow infrared band 9.5–11 μm. Its absolute accuracy is stated by the manufacturer to be ± 0.5°C. The radiometer temperature T_{IR} is affected not only by radiation emitted by the sea surface (i.e., by sea surface temperature), but also by sky radiation reflected from the sea surface and by absorption and radiation by the intervening atmosphere.

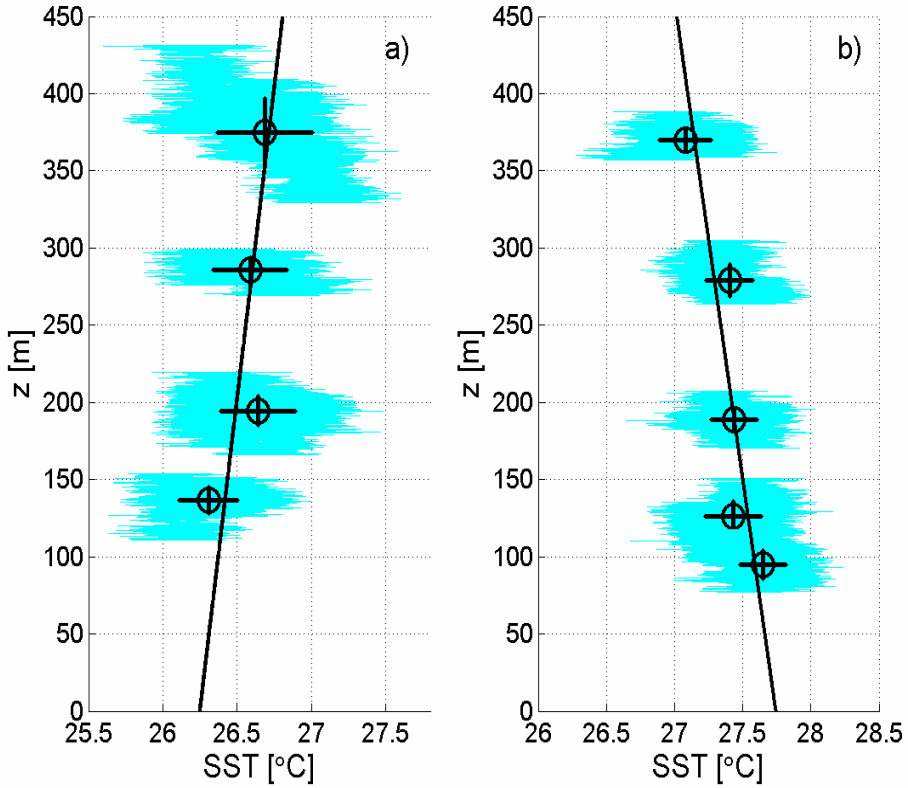

Fig. 2.8. Plot of radiometric sea surface temperature versus altitude for two stepped descents on 12 September.

Plots of measured infrared temperature versus altitude during stepped descents show a roughly linear trend in the BL as shown in Fig. 2.8. Although the mean slope is close to that of Burns et al. (2000), -0.0017 K m^{-1}, it was found to vary according to SST, even changing signs for the first descent of 12 September 2003, when SST was only 26.2°C (Fig. 2.8a). Here we use a different linear correction for each stepped descent. A correction for sky reflection (Burns et al. 2000) is not made here, as the longwave radiation was not measured on the aircraft. We note that the cooler SSTs seen on 12 September 2003 (as well as 2 and 13 September) were measured in the right rear storm quadrants. These are evidence of the cool wake following a hurricane, the result of the strong ocean mixing induced by the hurricane winds (Black et al. 2007).

Near-surface wind speeds are estimated using the stepped frequency microwave radiometer (SFMR: Uhlhorn and Black 2003) on N43RF. The radiometer measures brightness temperature *TB* at six microwave frequencies between 4.55 and 7.22 GHz. As the wind speed increases, so does the percentage of foam covering the sea surface. The increasing presence of foam, an effective blackbody, increases the emissivity and therefore *TB* with the effect increasing with frequency (in the microwave band). Uhlhorn and Black (2003) present the theory and algorithm used to extract wind speed from *TB*. The SFMR wind speed measurements were validated against near-surface (10 m) wind speeds from collocated GPS dropsondes. Here we use the latest SFMR wind speed algorithm, SWEMODv2, developed using data from the 2005 hurricane season (Uhlhorn et al. 2007).

2.4 Data Collection and Analysis method

2.4.1 The Data

The data analyzed in this thesis to investigate the vertical structure of turbulence and flux in the hurricane boundary layer were gathered during 11 boundary layer flights into 7 hurricanes during the 2002-2004 Atlantic Hurricane seasons. To determine the importance of different processes in the maintenance of the hurricane boundary layer, mean wind and thermal structure of the hurricane boundary layer are analyzed for these flights. The measurements of the turbulence statistics from the level legs are then related to the mean vertical structure. The goal of this dissertation is to assess the contributions of possible sources of the maintenance of a persistent nearly neutral surface layer and the decoupling of this layer from the stronger wind aloft in the rain free region between the outer rainbands. The contributions of turbulent mixing due to surface roughness and surface sensible heating/cooling as well as the latent heat release are investigated.

Three storms, Edouard, Lili and Isidore, were flown in 2002, the first two to test the new stepped-descent flight pattern strategy and the third to test extended low level flight pattern for detection of linear coherent turbulence structures, sometimes referred to as ‘roll vortex’ or ‘secondary boundary layer’ circulations. The main CBLAST field program began in 2003 with the survey flight pattern flown on 6 days by the two NOAA WP-3D aircraft (a total of 12 flights) including 15 stepped-descent patterns flown within the hurricane boundary layer in Hurricanes Fabian and Isabel. CBLAST flights in 2004 continued, but were restricted to flight levels above the boundary layer due to high

demand for reconnaissance flights as four hurricanes approached landfall on U.S. continent. The CBLAST flights in 2004 were in Hurricanes Frances on 4 days, Ivan on 5 days and Jeanne on 3 days. However, only two flights were flown into the boundary layer, one each in Hurricane Frances and Hurricane Jeanne.

GPS dropsonde data collected during the CBLAST experiment were utilized to study the vertical structure of the mean flow and coherent structures in the hurricane boundary layer. Typically, a GPS sonde is launched from the research aircraft at altitudes of 500 m to 3 km or higher. The accuracy of the wind speed measured by the GPS sonde is about 0.5-2.0 m s^{-1}, and that of the temperature is about 0.2 K (Franklin et al., 2003). GPS sonde measurements were initially smoothed by a 5-s low-pass filter to remove fluctuations due to under sampled scales and noise caused by satellite switching (Franklin et al., 2003). The dataset for this study consists of 942 hurricane dropsonde profiles obtained during the 2003-2004 seasons by NOAA P3 and AFRC hurricane-hunter aircraft. The dropsonde data used here have been postprocessed for quality control to ensure that any detectable errors were removed (Franklin et al., 2003).

2.4.2 Analysis Methods

To study the structure of the hurricane boundary layer and parameterization of the turbulent fluxes, flux runs were initially identified by evaluating key parameters such as aircraft altitude, attitude angles, and wind speed and so on, according to stationarity and homogeneity. Beginning and ending times for a given run are chosen based on markers set in-flight and are modified in post-flight analysis to remove sections where the aircraft is not straight and level or the plane passes through rain at the beginning or end of the leg leading to spikes in the wind data.

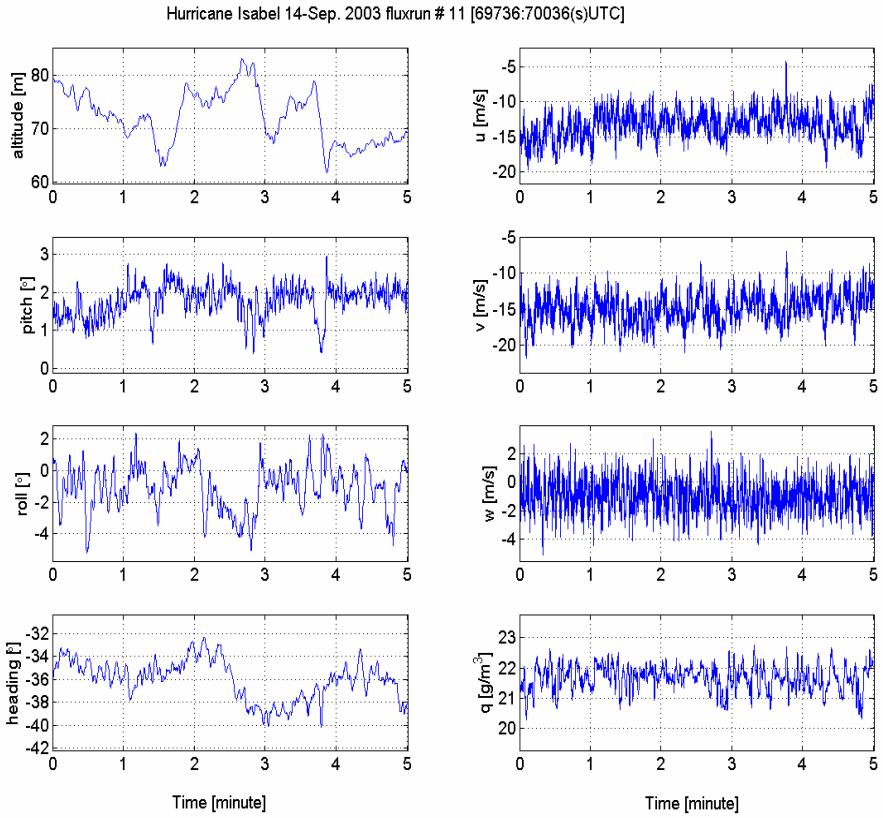

Fig. 2.9. Time series of aircraft altitude, attitude angles (pitch, roll and heading), three components of wind vector (u, v and w), and absolute humidity (measured from LICOR) for the flux run #11 of 14 Sep. 2003. All data are 40 Hz.

Examples of the 40 Hz time series of the aircraft altitude, attitude angles (pitch, roll and heading), and three components of wind and humidity of a typical flux run are presented in Fig. 2.9. In selecting the flux run, aircraft pitch and roll angles were checked to make sure that the aircraft was flying along a horizontal flight path. Any data with either the aircraft pitch or roll exceeding 5 degrees (absolute value) were discarded. Further, the airplane altitude variation should be within 30 m and the heading variation should be within 20 degrees. Further details of the data processing are provided by Zhang (2005).

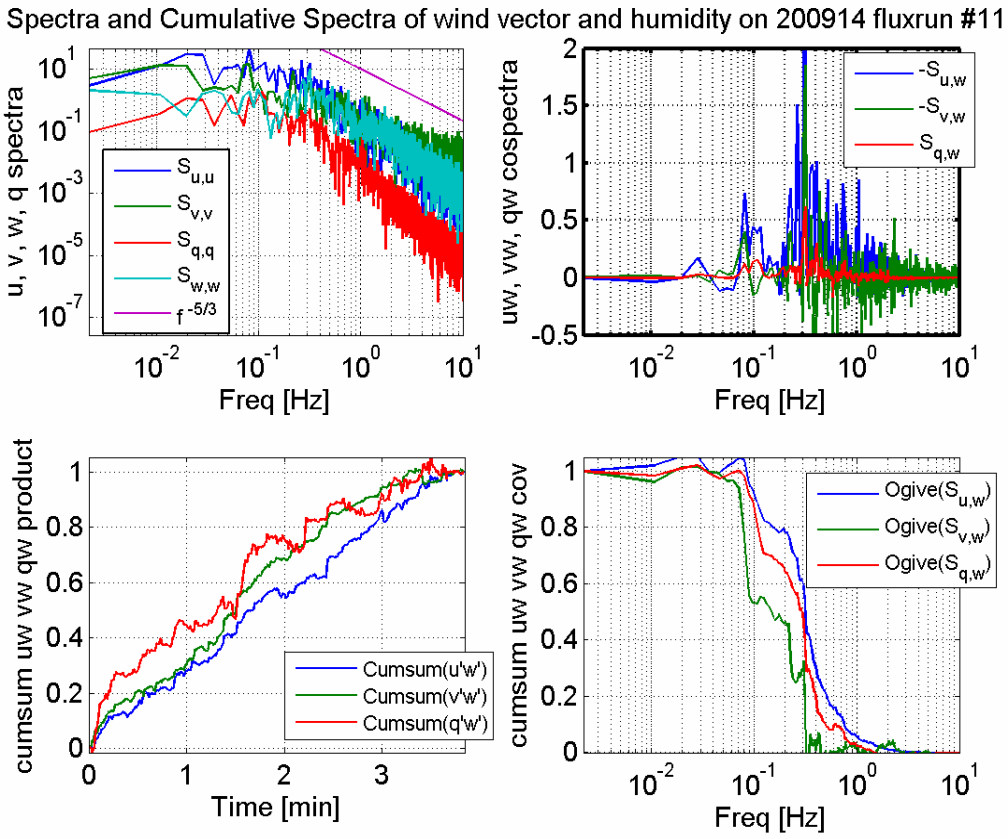

Figure 2.10: Spectra of the three components of the wind vector (u-blue, v-green, w-cyan) and humidity (red) are shown in the upper left panel, cospectra of uw (blue), vw (green) and qw (red) are shown in the upper right panel. Normalized cumulative sums of the products and covariances are shown in the lower panels. Note that the purple line in the upper left panel shows the -5/3 slope.

Data quality assurance for individual flux legs include inspection of the linear cumulative summation of the covariance, the power spectra for individual wind component, and co-spectra and ogives (Friehe et al. 1991) for along wind and cross wind stress. The use of ogive curves when estimating fluxes provides a useful insight into turbulent structure since they give a detailed description of how different scales contribute to turbulent transport. If the ogive curve approaches asymptotically a single value, then the stationary condition is met, and the final value of the ogive represents the total covariance or flux.

Fig. 2.10 shows the spectra and cospectra of the three components of wind vector and humidity for the same flux run shown above to give an example of the spectral analysis results. The normalized cumulative sum (cumsum) of the detrended products and covariances are also shown here. Note that here is almost no unexpected change in the normalized cospectra cumsum plots, such that the energy is well contained in the middle frequency range from 0.01 Hz to 1 Hz.

Additionally, a wavelet transform method is applied to the vertical velocity signals in order to study the temporal structure of the wind field. The wavelet transform allows for a decomposition of a signal in both frequency and time. This technique is used to study the effects of roll vortices on turbulent fluxes, which will be discussed in the Chapter 4.

Chapter 3

Turbulent Fluxes

3.1 Introduction

In this study, turbulent fluxes are measured directly using the eddy correlation method. The turbulent fluxes of momentum, sensible heat and latent heat are given by

$$\tau = \rho(-\overline{w'u'}\,\hat{i} - \overline{w'v'}\,\hat{j})\,, H = \rho c_P \overline{w'\theta'}\,, \text{ and } E = \rho L_v \overline{w'q'}\,, \tag{3.1}$$

respectively, where prime indicates turbulent fluctuations, *u, v, w, t* and *q* represent along-wind velocity, cross-wind velocity, vertical velocity, potential temperature and specific humidity respectively, ρ the air density, c_p the specific heat at constant pressure, L_v the latent heat of vaporization, and overbar represents averages over a period of time. According to the similarity theory proposed by Monin and Obukhov (1954), scaling parameters for momentum, sensible heat and latent heat, respectively, can be derived from these fluxes as follows:

$$u_* = (|\tau|/\rho)^{1/2},\ t_* = H/(\rho c_P)/u_*,\ \text{and}\ q_* = E/(\rho L_v)/u_*\,, \tag{3.2}$$

assuming turbulent fluxes are constant in the surface layer in stationary and homogeneous conditions. Note that typically the surface layer is taken to be the lowest 10% of the

atmospheric boundary layer. M-O similarity theory relates the scaling parameters to the mean quantities with expressions of the form:

$$U(z)-U(0)=\frac{u_*}{\kappa}\log\left(\frac{z}{z_o}-\Psi_u\left(\frac{z}{L}\right)\right),\qquad \Theta(z)-\Theta(0)=\frac{P_r t_*}{\kappa}\log\left(\frac{z}{z_{0t}}-\Psi_\theta\left(\frac{z}{L}\right)\right),$$

$$Q(z)-Q(0)=\frac{P_r q_*}{\kappa}\log\left(\frac{z}{z_{0q}}-\Psi_q\left(\frac{z}{L}\right)\right), \tag{3.3}$$

where $U(z)$, $\Theta(z)$ and $Q(z)$ are the horizontal wind speed, potential temperature and specific humidity, respectively, at height z above the surface; z_0, z_{0t} and z_{0q} are the surface roughness lengths; Pr = 0.85 is the turbulent Prandtl number; Ψ_u, Ψ_θ and Ψ_q are functions of the stability index $\frac{z}{L}$ (Donelan, 1990) , where L is the Obukhov length, and $L= -u_*^3\ [\kappa g(\ H/(c_P\theta) + 0.61\ E/L_v)/\rho]^{-1}$; κ is the von Kármán constant κ≈0.4 and g the gravitational constant. The Obukhov length represents the height where turbulence production due to shear is equal to that due to buoyancy.

Although the surface fluxes are the physical quantities of interest, models typically rely on bulk parameterizations of them in terms of bulk coefficients at 10-m above the surface in neutral conditions where buoyant forcing is negligible ($\frac{z}{L}$ = 0). For momentum (the drag coefficient), sensible heat (the Stanton number), and latent heat (the Dalton number), the 10-m bulk relations are:

$$C_{D10N}=\frac{\tau}{\rho(U_{10N}-U_0)^2},\quad C_{H10N}=\frac{\overline{w'\theta'}}{(\theta_{10N}-\theta_0)(U_{10N}-U_0)},\quad C_{E10N}=\frac{\overline{w'q'}}{(Q_{10N}-Q_0)(U_{10N}-U_0)}, \tag{3.4}$$

where subscript N represents neutral conditions and subscript 0 represents the surface.

In the following section of this Chapter, results of the direct measurements of turbulent fluxes and bulk parameterization of the surface fluxes are demonstrated. Section 3 discusses the errors of the turbulent flux measurements. The variability of surface fluxes by storm quadrant is shown in Section 4.

3.2 Turbulent Fluxes and Parameterization

Following the analysis methods mentioned in section 2.4.2 in Chapter 2, a total of 128 flux runs below 1000 m were made in the seven storms mentioned above, of which 118 were completed below 500 m and 108 were qualitatively accepted for analysis. Wind, temperature and humidity data from these flux runs are used to compute wind stress, friction velocity, enthalpy flux and ultimately estimate the 10 m neutral drag coefficient, Dalton number and Stanton number. Table 1 summarizes the measurements and calculations for each of the 128 runs suitable for this analysis. Due to the lack of the fast-response humidity sensors during 2002 and the absence of stepped descent flight patterns, there are only 52 and 42 suitable flux runs for the humidity and sensible heat flux measurements, respectively. The majority of the runs are oriented along the mean wind vector, reflecting the difficulty in finding a long enough path of rain-free space in the cross wind direction. The average air-relative leg length is roughly 28 km, with a minimum of 13 km from one of the lower altitude legs, and a maximum of more than 55 km. The majority of legs are between 20 and 30 km in length. The lowest altitude leg is 53 m. Only 6 legs are at the altitudes below 100 m. Leg-averaged mean flight level winds speeds vary from 21 m s^{-1} to just over 40 m s^{-1}, with most between 30 and 35 m s^{-1}.

Table 3.1 Summary of Data and Calculations from 128 Flux runs in Seven Storms

Run No.	Date	Alt (m)	U(z) (ms^{-1})	U_{10N} (ms^{-1})	θ_{10N} (K)	Q_{10N} (gkg^{-1})	SST (°C)	Q_0 (gkg^{-1})	u_* (ms^{-1})	t_* (K)	q_* (gkg^{-1})	$C_{D,10N}$ ($X10^3$)	$C_{H,10N}$ ($X10^3$)	$C_{E,10N}$ ($X10^3$)
1	20020903	301	12.8	11.1	-	-	-	-	0.35	-	-	0.97	-	-
2	20020903	297	12.1	10.2	-	-	-	-	0.41	-	-	1.58	-	-
3	20020903	297	12.5	10.2	-	-	-	-	0.36	-	-	1.25	-	-
4	20020903	295	13.6	10.3	-	-	-	-	0.36	-	-	1.19	-	-
5	20020903	296	12.7	10.1	-	-	-	-	0.34	-	-	1.11	-	-
6	20020903	305	15.7	13.8	-	-	-	-	0.48	-	-	1.20	-	-
7	20020903	287	20.5	18.7	-	-	-	-	0.68	-	-	1.32	-	-
8	20020903	285	23.3	19.2	-	-	-	-	0.67	-	-	1.20	-	-
9	20020903	336	14.4	12.8	-	-	-	-	0.48	-	-	1.40	-	-
10	20020903	303	17.1	12.9	-	-	-	-	0.49	-	-	1.46	-	-
11	20020903	300	16.5	13.1	-	-	-	-	0.54	-	-	1.71	-	-
12	20020903	302	16.6	14.6	-	-	-	-	0.45	-	-	0.93	-	-
13	20020903	304	16.4	14.9	-	-	-	-	0.51	-	-	1.17	-	-
14	20020903	286	16.1	13.2	-	-	-	-	0.60	-	-	2.08	-	-
15	20020903	312	15.4	13.1	-	-	-	-	0.45	-	-	1.15	-	-
16	20020903	305	14.1	11.7	-	-	-	-	0.34	-	-	0.86	-	-
17	20020903	175	14.4	11.6	-	-	-	-	0.34	-	-	0.83	-	-
18	20020903	171	15.0	13.1	-	-	-	-	0.41	-	-	0.98	-	-
19	20020903	297	14.6	11.9	-	-	-	-	0.39	-	-	1.07	-	-
20	20020903	303	14.8	11.8	-	-	-	-	0.48	-	-	1.65	-	-
21	20020903	185	15.5	12.4	-	-	-	-	0.41	-	-	1.07	-	-
22	20020903	180	14.5	12.4	-	-	-	-	0.42	-	-	1.14	-	-
23	20020903	123	16.3	13.0	-	-	-	-	0.52	-	-	1.61	-	-
24	20020903	121	16.0	13.5	-	-	-	-	0.63	-	-	2.16	-	-
25	20020903	59	18.7	14.6	-	-	-	-	0.44	-	-	0.92	-	-
26	20020903	53	19.7	15.6	-	-	-	-	0.50	-	-	1.02	-	-
27	20020903	289	16.3	13.9	-	-	-	-	0.46	-	-	1.09	-	-
28	20020903	328	14.3	11.5	-	-	-	-	0.38	-	-	1.06	-	-
29	20020903	189	13.7	11.9	-	-	-	-	0.48	-	-	1.65	-	-
30	20020903	175	16.5	14.2	-	-	-	-	0.58	-	-	1.65	-	-
31	20020903	172	15.6	13.6	-	-	-	-	0.49	-	-	1.29	-	-
32	20020903	302	16.6	14.2	-	-	-	-	0.54	-	-	1.45	-	-
33	20020903	298	16.2	13.4	-	-	-	-	0.60	-	-	1.99	-	-
34	20020903	122	17.7	14.5	-	-	-	-	0.48	-	-	1.11	-	-
35	20020903	118	18.4	15.4	-	-	-	-	0.54	-	-	1.25	-	-
36	20020903	57	18.5	15.4	-	-	-	-	0.46	-	-	0.90	-	-
37	20020903	69	18.1	15.6	-	-	-	-	0.61	-	-	1.54	-	-
38	20020922	294	32.2	21.6	-	-	-	-	1.08	-	-	2.51	-	-

39	20020922	319	35.4	23.0	-	-	-	-	1.05	-	-	2.06	-	-
40	20020922	194	30.9	21.1	-	-	-	-	0.98	-	-	2.17	-	-
41	20020922	197	29.1	20.3	-	-	-	-	0.88	-	-	1.89	-	-
42	20020922	315	26.6	18.1	-	-	-	-	0.82	-	-	2.05	-	-
43	20021003	261	27.5	21.8	-	-	-	-	0.63	-	-	0.84	-	-
44	20021003	258	30.7	22.7	-	-	-	-	0.86	-	-	1.43	-	-
45	20021003	273	27.6	21.3	-	-	-	-	0.71	-	-	1.10	-	-
46	20021003	173	27.1	21.8	-	-	-	-	0.88	-	-	1.62	-	-
47	20021003	181	25.1	21.2	-	-	-	-	0.96	-	-	2.07	-	-
48	20021003	186	25.2	20.6	-	-	-	-	0.69	-	-	1.13	-	-
49	20021003	171	24.1	20.6	-	-	-	-	0.81	-	-	1.56	-	-
50	20030902	762	35.3	23.3	-	-	25.9	-	-	-	-	-	-	-
51	20030902	360	36.8	24.2	-	-	26.6	-	-	-	-	-	-	-
52	20030902	278	32.6	22.9	299.9	17.8	26.7	22.6	0.97	0.00	0.14	1.86	-7.20	1.25
53	20030902	179	29.7	21.8	299.8	17.7	26.7	22.3	0.80	-0.02	0.16	1.41	5.24	1.30
54	20030902	136	28.3	21.2	299.3	17.6	26.6	22.0	0.94	-0.01	0.13	1.99	1.35	1.28
55	20030902	79	29.1	24.8	299.7	17.7	26.7	22.0	0.78	0.00	0.10	1.03	0.22	0.77
56	20030902	773	38.7	24.7	-	-	25.1	-	-	-	-	-	-	-
57	20030902	793	32.0	23.5	-	-	26.9	-	-	-	-	-	-	-
58	20030902	373	36.0	23.1	-	-	26.8	-	-	-	-	-	-	-
59	20030902	288	33.4	24.2	299.9	18.0	26.8	22.7	0.76	0.03	0.19	1.02	-20.16	1.29
60	20030903	374	32.2	24.7	300.4	18.5	30.0	27.8	1.13	-0.10	0.16	2.25	1.67	0.81
61	20030903	290	34.7	22.4	-	-	30.3	-	-	-	-	-	-	-
62	20030903	283	36.4	26.9	-	-	29.8	-	-	-	-	-	-	-
63	20030903	273	40.5	29.0	298.7	15.3	29.8	27.1	1.00	-0.09	0.34	1.15	0.69	1.01
64	20030903	187	37.2	28.7	298.8	15.8	29.7	26.6	1.43	-0.06	0.35	2.53	0.72	1.64
65	20030903	196	34.9	28.1	298.9	15.7	29.9	26.9	1.18	-0.03	0.28	1.80	0.29	1.07
66	20030903	132	30.7	26.6	299.5	15.3	29.8	26.7	1.05	-0.03	0.22	1.60	0.37	0.75
67	20030903	750	39.2	27.2	-	-	28.1	-	-	-	-	-	-	-
68	20030903	376	36.6	27.2	-	-	29.2	-	-	-	-	-	-	-
69	20030903	270	36.5	28.9	301.1	14.8	29.3	26.3	1.05	-0.08	0.22	1.30	2.14	0.69
70	20030903	157	35.9	28.1	300.2	14.8	29.2	25.9	1.21	-0.06	0.25	1.98	1.14	0.99
71	20030904	368	30.3	21.9	-	-	29.1	-	0.68	-	-	0.84	-	-
72	20030904	361	30.4	22.6	-	-	29.2	-	0.88	-	-	1.46	-	-
73	20030904	369	29.9	21.3	301.1	18.3	29.0	25.9	0.82	-0.02	0.21	1.39	0.80	1.09
74	20030904	282	29.4	20.7	-	-	29.1	-	-	-	-	-	-	-
75	20030904	280	28.4	20.2	-	-	29.7	-	0.83	-	-	1.53	-	-
76	20030904	194	26.7	20.7	300.6	17.9	29.8	26.7	1.11	-0.01	0.14	2.84	0.16	0.86
77	20030904	135	22.2	18.6	300.3	17.4	29.7	26.4	0.77	-0.04	0.12	1.68	0.65	0.55
78	20030904	104	21.5	22.0	299.8	18.0	29.5	26.1	0.72	-0.07	0.10	1.06	0.80	0.44
79	20030912	375	35.2	24.5	301.5	20.0	26.2	22.2	0.97	0.06	0.14	1.57	1.23	2.53

80	20030912	286	32.2	18.9	301.0	19.8	26.2	22.0	0.66	0.08	0.15	1.15	1.69	2.44
81	20030912	194	31.4	19.1	301.6	19.2	26.4	22.0	0.88	0.03	0.09	2.05	0.71	1.46
82	20030912	137	25.2	16.5	301.4	19.1	26.2	21.5	0.81	0.02	0.08	2.40	0.55	1.71
83	20030912	88	24.3	20.3	301.3	19.0	27.4	23.0	0.84	0.03	0.12	1.75	1.32	1.24
84	20030912	126	32.7	24.5	301.9	18.8	27.6	23.5	1.30	0.00	0.04	2.84	0.21	0.49
85	20030912	95	27.0	21.9	301.5	19.0	27.8	23.6	0.88	0.03	0.11	1.63	2.22	0.93
86	20030912	189	31.3	21.6	-	-	27.7	-	1.13	-	-	2.71	-	-
87	20030912	279	29.9	21.6	301.7	18.7	27.8	24.2	0.87	0.03	0.11	1.54	1.58	0.83
88	20030912	370	32.6	22.0	-	-	27.7	-	0.98	-	-	1.97	-	-
89	20030913	365	35.6	19.8	302.1	20.1	26.7	22.8	0.86	0.05	0.10	1.81	0.91	1.56
90	20030913	256	35.3	21.9	302.2	19.9	26.8	22.7	1.04	0.05	0.11	2.24	1.09	1.88
91	20030913	189	33.0	19.7	302.1	19.6	26.8	22.5	0.91	0.03	0.06	2.14	0.58	0.93
92	20030913	120	29.5	21.2	302.0	19.7	26.7	22.2	0.89	0.04	0.09	1.75	0.71	1.45
93	20030913	70	27.8	24.7	301.9	19.4	26.7	22.0	0.95	0.02	0.08	1.49	0.34	1.12
94	20030913	382	35.2	23.8	-	-	27.4	-	-	-	-	-	-	-
95	20030913	269	36.3	24.0	-	-	27.4	-	1.17	-	-	2.42	-	-
96	20030913	193	31.1	22.6	301.8	19.2	27.4	23.2	0.91	0.03	0.12	1.73	0.97	1.22
97	20030914	370	29.9	22.2	-	-	28.7	-	-	-	-	-	-	-
98	20030914	278	34.8	22.9	302.8	19.2	28.7	25.5	0.96	0.03	0.12	1.79	1.25	0.82
99	20030914	179	29.5	22.5	302.8	19.6	28.7	25.2	0.90	0.03	0.20	1.64	1.22	1.45
100	20030914	132	31.4	23.3	302.8	19.3	28.7	25.1	1.09	0.03	0.14	2.22	1.66	1.18
101	20030914	94	32.0	25.7	302.7	19.3	28.6	24.8	1.11	0.03	0.12	1.80	1.19	0.95
102	20030914	104	31.1	27.6	302.7	19.5	28.6	24.9	1.14	0.04	0.19	1.72	1.84	1.44
103	20030914	383	30.3	22.2	302.8	19.3	28.8	26.0	1.18	0.03	0.15	2.70	1.93	1.23
104	20030914	268	32.9	21.6	303.0	19.4	28.9	25.6	1.09	0.01	0.16	2.45	0.40	1.25
105	20030914	187	27.2	20.9	302.6	19.7	28.9	25.4	0.98	0.03	0.17	2.24	2.59	1.41
106	20030914	120	29.1	22.4	302.8	19.2	28.9	25.2	1.04	0.01	0.10	2.20	0.57	0.75
107	20030914	72	22.8	24.2	302.6	19.4	28.8	25.0	0.95	0.01	0.14	1.57	0.72	0.98
108	20030914	361	36.4	24.6	302.7	18.9	29.0	26.4	1.03	0.03	0.16	1.78	2.42	0.89
109	20030914	270	33.7	24.8	-	-	29.0	-	-	-	-	-	-	-
110	20030914	277	31.7	23.8	302.9	19.6	29.3	26.5	1.05	0.08	0.27	1.97	7.83	1.72
111	20030914	185	34.1	22.5	-	-	29.0	-	1.18	-	-	2.83	-	-
112	20040901	484	20.4	15.41	-	20.2	29.4	27.9	0.48	-	-0.03	0.96	-	0.15
113	20040901	478	20.3	15.97	-	-	29.4	-	0.48	-	-	0.96	-	-
114	20040901	484	20.6	17.27	-	-	28.8	-	0.59	-	-	1.37	-	-
115	20040901	484	21.6	16.57	-	22.8	29.5	28.1	0.64	-	-0.15	1.37	-	1.32
116	20040901	457	22.0	16.01	-	22.2	29.7	28.4	0.80	-	-0.08	2.35	-	0.75
117	20040901	563	28.9	21.45	-	22.7	29.7	28.4	0.69	-	-0.11	1.88	-	0.98
118	20040901	530	32.7	22.71	-	-	29.4	-	0.98	-	-	2.08	-	-
119	20040901	498	32.7	23.58	-	-	29.6	-	0.70	-	-	0.96	-	-
120	20040901	487	32.3	22.69	-	22.0	29.7	28.4	0.67	-	-0.14	0.80	-	0.74

121	20040901	466	33.8	23.48	-	21.5	29.8	28.7	0.87	-	-0.17	1.47	-	1.09
122	20040922	719	28.7	20.04	-	22.6	30.0	28.9	0.86	-	-0.18	1.34	-	1.27
123	20040922	717	30.9	21.77	-	-	27.4	-	0.70	-	-	1.21	-	-
124	20040922	712	35.1	24.67	-	-	23.9	-	0.98	-	-	2.04	-	-
125	20040922	724	36.0	23.66	-	-	24.8	-	0.68	-	-	0.76	-	-
126	20040922	387	32.8	22.52	-	-	25.6	-	0.84	-	-	1.26	-	-
127	20040922	400	33.4	22.19	-	22.1	27.5	25.1	1.29	-	-0.10	3.28	-	1.81
128	20040922	283	30.4	21.63	-	22.0	27.2	24.7	0.96	-	-0.10	1.89	-	1.57

3.2.1 Momentum Flux

Although the turbulent flux is measured at order 100m above the surface, the quantity of interest is the surface flux in order to derive the air-sea exchange coefficients. For momentum flux, Figure 3.1 shows variation in $(|\tau/\rho|)^{1/2}$ with altitude. Data from each stepped descent in this study are shown in separate panels. An initial approach of estimating the surface friction velocity based on linear regression and extrapolating to the surface results in the dashed lines shown in the figure. This method works reasonably well for stepped descents that consist of several flux legs at different altitudes. Many of the stepped descents, cross wind patterns in particular, consist of four or fewer legs and the resultant linear fit extrapolation is much worse. Although there appears no direct correlation between the quality of a linear fit (for a given stepped descent) and the variation of a bulk quantity such as mean wind speed for a leg, one must question the validity of the assumption of stationarity during an entire stepped descent.

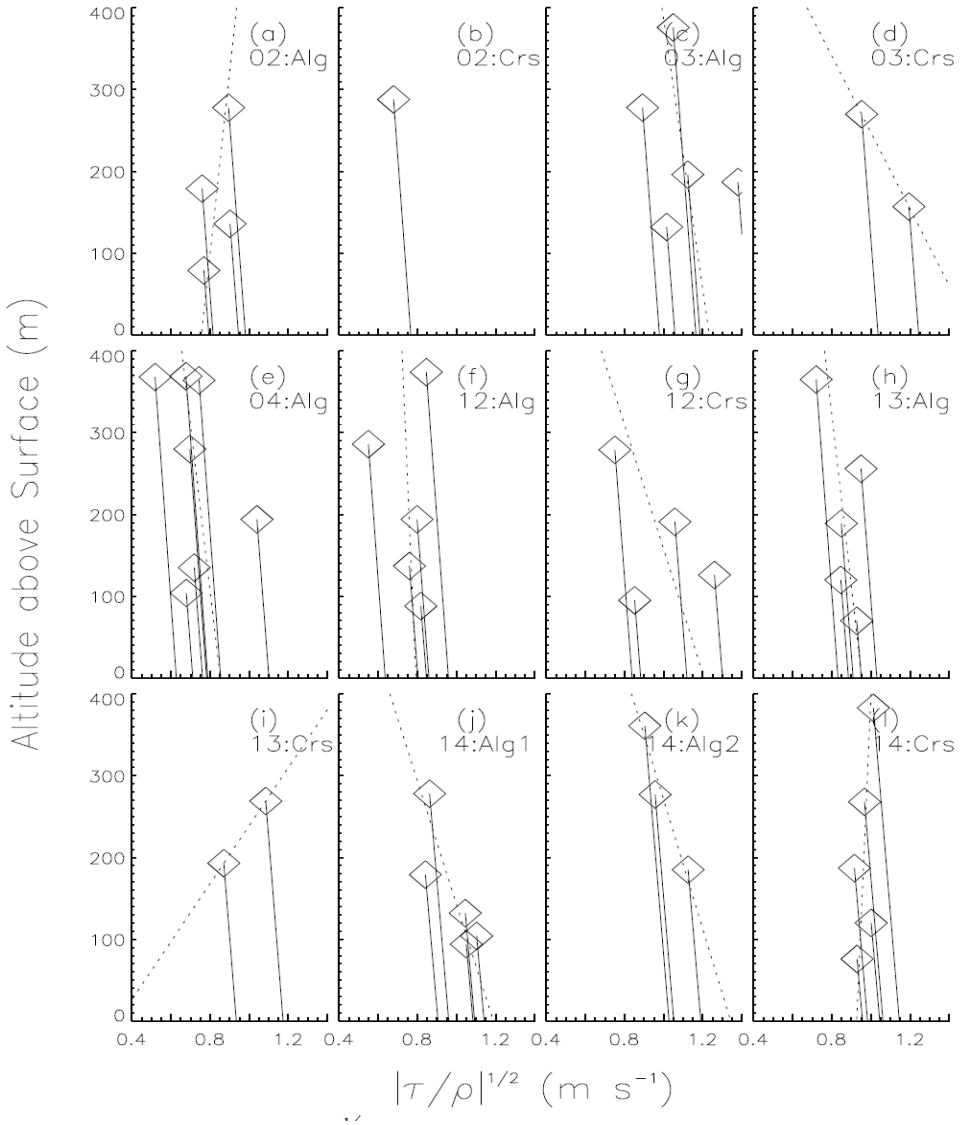

Fig. 3.1. Total covariance as a function of altitude for twelve individual stepped descents. The dashed line shows the best linear fit, extrapolated to the surface. The solid lines show the extrapolation of friction velocity following Donelan (1990; see text). 'Crs' and 'Alg' designators represent cross-wind and along-wind runs, respectively. Number represents day in September 2003.

The solid lines in Fig. 3.1 illustrate results from using a height-based correction to the friction velocity assuming a nominally-constant stress surface layer and correcting for the influence of the Coriolis force and the horizontal pressure gradient following Donelan

(1990) and Banner et al. (1999). This correction indicates that the momentum flux decays with height according to the following:

$$\frac{\tau}{\rho} = u_*^2 (1 - \frac{afz}{u_*}), \tag{3.5}$$

where f is the Coriolis parameter given by $f = 1.454 \times 10^{-4}$ sin(lat) rad s^{-1} and $a = V_{gs} / u_*$, where V_{gs} is the component of the geostrophic wind normal to the surface wind. Following Donelan (1990), we use $a = 12$.

It should be pointed out that among the assumptions made by Donelan (1990) are (1) that at the surface the pressure gradient is balanced by the vertical gradient of stress, (2) that the stress is zero at the top of the boundary layer, (3) that the wind is in geostrophic balance at the top of the boundary layer, and (4) that conditions are temporally and spatially homogeneous. All of the above assumptions are questionable within hurricanes, but assumptions 2 and 3 can be tested directly in this study. One expects that in hurricanes the wind at the top of the boundary layer must be consistent with gradient balance rather than geostrophic (must include centrifugal force) as following:

$$\frac{V_g^2}{r} + fV_g = \frac{1}{\rho}\frac{\partial p}{\partial r}, \tag{3.6}$$

where V_g is gradient wind, r is the distance to the storm center, and p is the pressure. Data from cross wind legs on Sep2 in Hurricane Fabian support that the wind is in gradient balance even at 150 km from the storm center. Also, our data indicate that the stress does not vanish at the top of the hurricane boundary layer that is defined by the

lowest inversion height in the potential temperature profile (as discussed later in Chapter 5), but is rather approximately 1/2 to 3/4 the value at the surface. Indeed, applying corrections similar to that derived by Donelan (1990) but accounting for gradient wind and a non-zero stress at the top of the boundary layer results in a magnitude of the correction of roughly 10 to 15% for most of our flux runs. This is about the same magnitude as the simply applying the Donelan (1990) correction. This is likely the single largest error introduced in our estimation of the drag coefficient. We estimate that the error in this correction is on the order of 5% for u_*, resulting in a 10% error in drag coefficient. The error is may be larger for runs near the top of the boundary layer and likely smaller for runs nearer the surface.

Using the corrected u_* the 10 –m neutral wind speed for each flux run is computed according to Eq. 3. As the surface wind speed is also measured by the SFMR, Fig. 3.2 shows the comparison of the profile-derived and SFMR measured 10-m winds for the data collected during Hurricanes Fabian and Isabel. The correlation between the two variables is $\gamma^2 = 0.895$, and the best-fit linear regression line between the two is $U10_{SFMR} = U10_{PROF} - 0.5$, indicating that they agree well in the mean, but the profile-derived winds at higher altitudes are 0.5±0.1 ms^{-1} higher in the mean than the SFMR winds. The profile-derived surface winds also show much higher variability within given stepped descents than the SFMR surface winds. Here we take the SFMR winds to be the best estimate of U_{10N}. This avoids the need to assume logarithmic wind speed profiles, which we consider to be questionable in hurricane conditions.

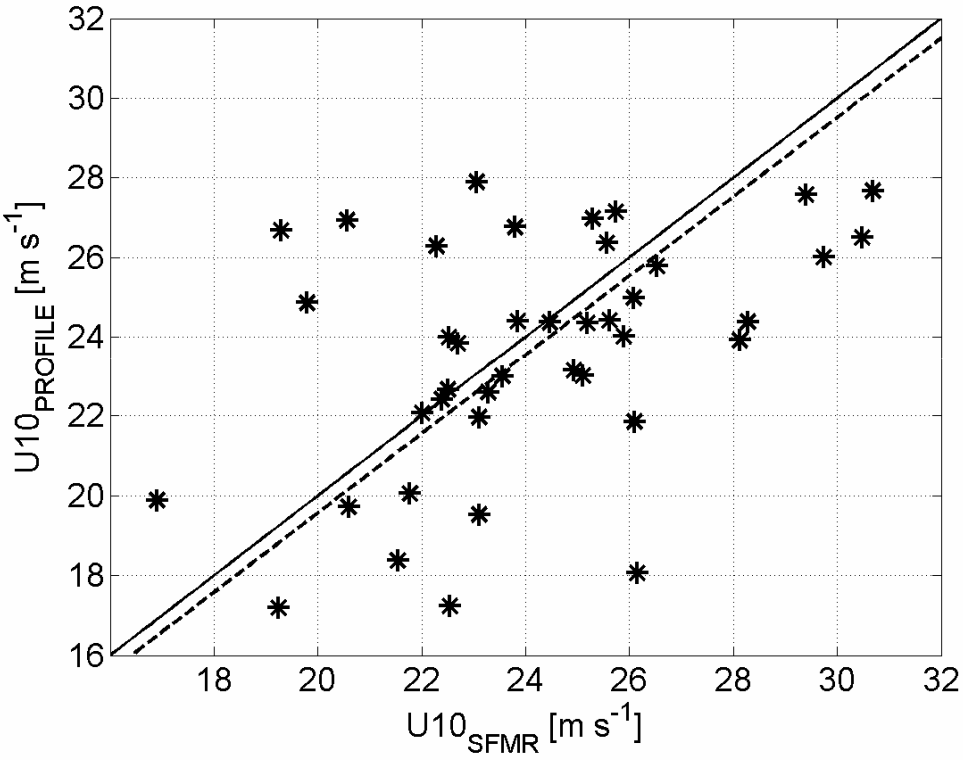

Fig. 3.2. A comparison of profile-derived and SFMR measured 10-m winds. The dashed and solid lines are the best fit regression and 1:1 lines, respectively.

Figure 3.3 shows the drag coefficients $C_{D,10N}$, computed from the 108 flux runs plotted as a function of near surface neutral wind speed, U_{10N}. The bold stars and line in the figure represent the bin averaged drag coefficient for 4 m s^{-1} wide bins centered at 12, 16, 20 m s^{-1}, etc. Results from this study are in general agreement with results from the earlier studies for wind speeds of 10 and 22 m s^{-1}. Our measurements suggest a roll-off at even lower wind speeds around 23 m s^{-1} and at a smaller value of the drag coefficient, compared to the Powell el al. (2003) and Donelan et al. (2004) studies. Unfortunately, data from this study were not collected at wind speeds much greater than 30 m s^{-1}, and thus we cannot speculate on the behavior of the drag coefficient at even greater wind speeds.

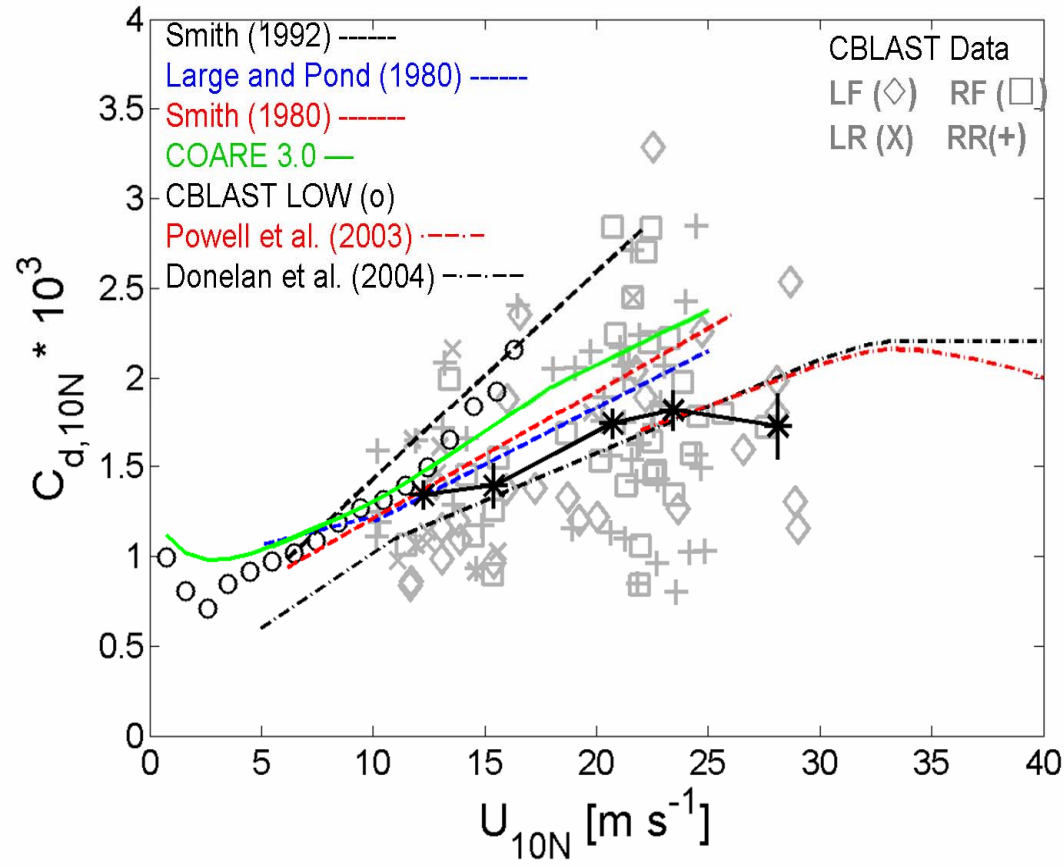

Fig. 3.3. Plot of drag coefficients as a function of wind speed. The asterisks represent average values in 4 msP^{-1P} bins; The data are from aircraft measurements during Hurricanes Edouard, Isidore, Lili, Fabian, Isabel, Frances and Jeanne; Green curve is from Fairall et al. (2003), blue curve from Smith (1980), black-dashed curve from Donelan et al. (2004), and red-dashed curve from Powell et al. (2003). The CBLAST results show qualitative agreement with both recent curves, with the drag coefficient leveling off for wind speed above about 25 m/s.

3. 2.2 Latent Heat Flux

For latent heat flux, Fig. 3.4 shows vertical profiles of $\overline{w'q'}$ in the boundary layer, where each profile represents a stepped descent. Only profiles with four or more points

are used. The mean and standard deviation of these regression slopes are calculated as -0.00005 ± 0.0003, which shows that the water vapor flux was constant throughout the boundary layer. A statistical analysis of the profile slopes indicates the CBLAST data to be constant with height (95% confidence), in support of the DeCosmo et al. (1996) HEXOS aircraft data, and also those of Nicholls and Readings (1979). Therefore the measured fluxes are taken as indicative of surface values.

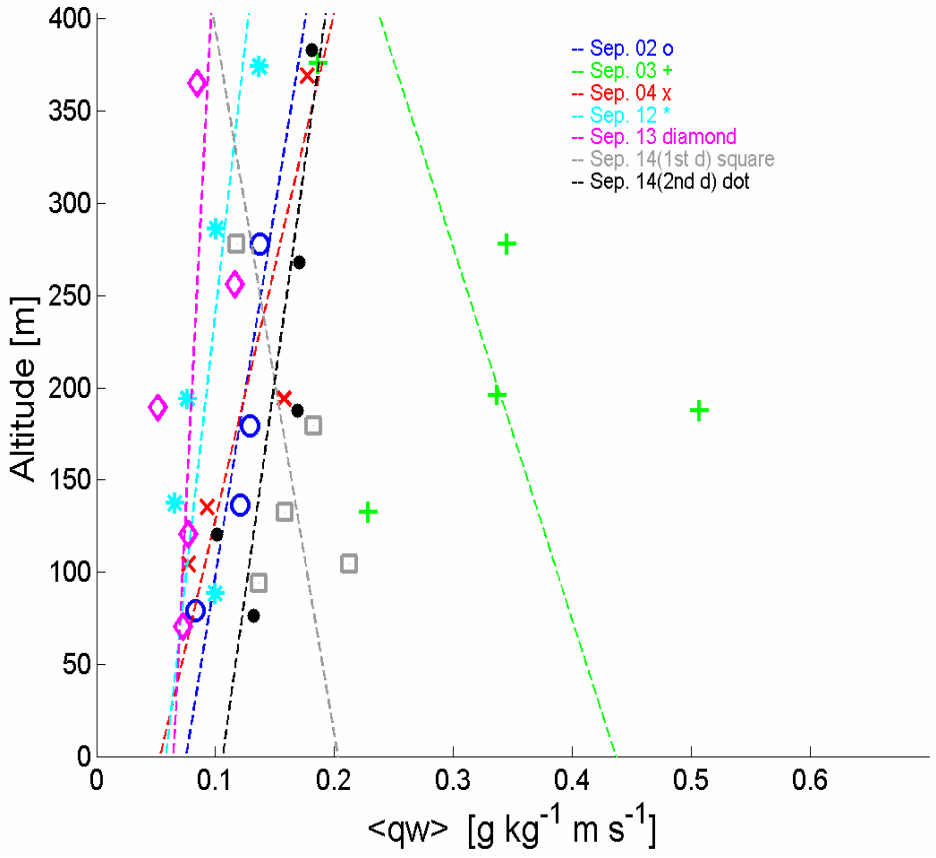

Fig. 3.4. Plot of $\overline{w'q'}$, covariance of specific humidity with vertical velocity, versus altitude z for CBLAST stepped descents. Only descents with 4 or more altitudes are used. The symbols represent the different descents: 20030902: o, 03: +, 04: x, 12: *, 13: ◊, 14-1: □, 14-2 ●. The dashed lines represent slopes for each descent.

Fig. 3.5 shows the 10 m neutral Dalton numbers versus $U_{10N.}$ The mean value of the 42 points is $(1.18 \pm 0.07) \times 10^{-3}$, showing one standard error. This is close to the original HEXOS man value and is slightly above the GASEX and SOWEX means. Fairall et al. (2003) revised the HEXOS data by applying the Webb correction, accounting for the 2% reduction in saturated surface humidity due to salinity, and adjusting for the use of an O(5 m) bulk value for sea surface temperature. The original HEXOS Dalton numbers are raised by 8% to 1.2×10^{-3}, that is slightly higher than the present result.

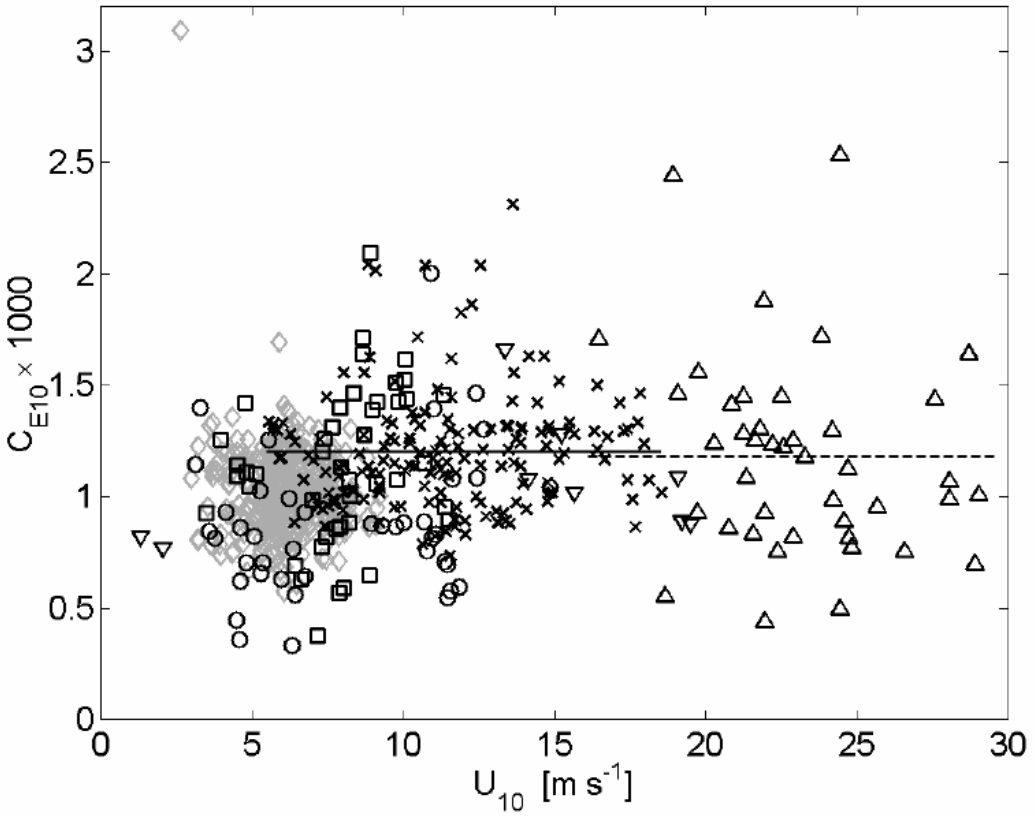

Fig. 3.5. Plot of Dalton number vs wind speed, both neutral 10 m. The CBLAST data points and mean value are shown with Δ and dashed line, respectively. The HEXOS data (DeCosmo et al. 1996), shown with $\times$ and the solid line, have been corrected according to Fairall et al. (2003). Other symbols are from experiments: AGILE (o: Donelan and Drennan 1995), HEXOS (x: DeCosmo et al. 1996), GASEX ($\Diamond$: McGillis et al. 2004), SOWEX (∇: Banner et al. 1999), and SWADE (□: Katsaros et al. 1993).

3.2.3 Sensible Heat Flux

For sensible heat flux, Fig. 3.6 shows vertical profiles of $\overline{w'\theta'}$ in the boundary layer, where each profile represents a stepped descent. Again, only profiles with four or more points are used. A statistical analysis of the profile slopes indicates that $\overline{w'\theta'}$ increases as the height decreases, in the similar manner as the DeCosmo et al. (1996) HEXOS aircraft data, and also that of Nicholls and Readings (1979). In this study, different linear regression for each stepped descent is used to obtain the surface sensible heat fluxes.

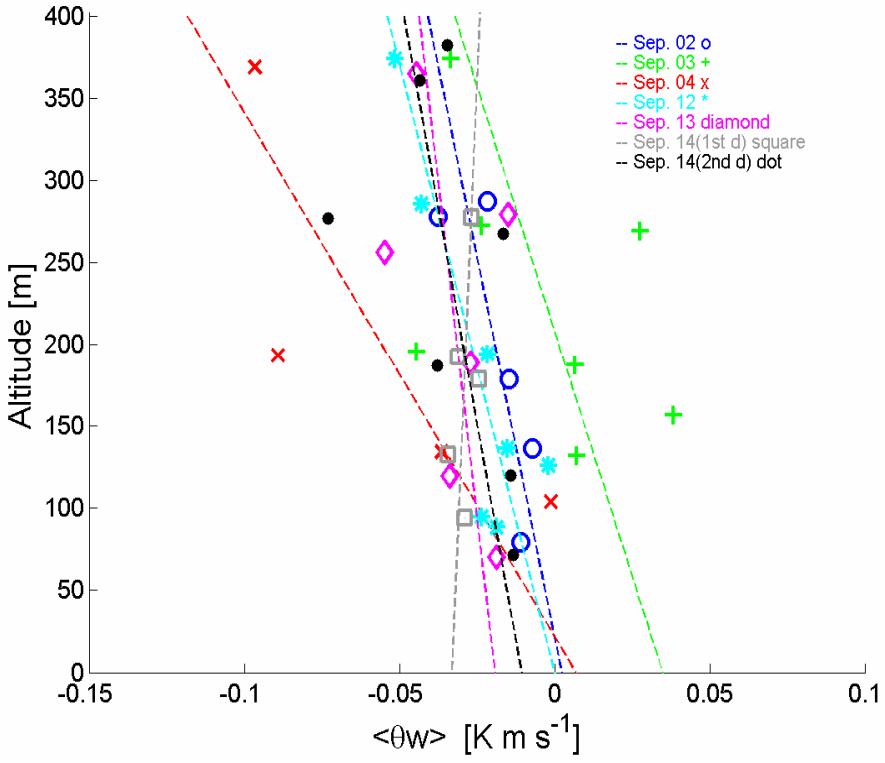

Fig. 3.6. Plot of $\overline{w'\theta'}$, covariance of potential temperature with vertical velocity, versus altitude z for CBLAST stepped descents. Only descents with 4 or more altitudes are used. The symbols represent the different descents: 20030902: o, 03: +, 04: x, 12: *, 13: ◊, 14-1: □, 14-2 ●. The dashed lines represent slopes for each descent.

Fig. 3.7, shows the surface $\overline{w'\theta'}$ versus $U_{10N}(\Theta_0 - \Theta_{10N})$. Data with $\Delta\Theta$ larger than 0.5 ºC are presented. This plot showing that both the stable and unstable data pass through zero indicates the bias of the corrected SST using the method discussed in Chapter 2 is small. The stable data mostly represent conditions in the right rear of the storm, above the cold wake.

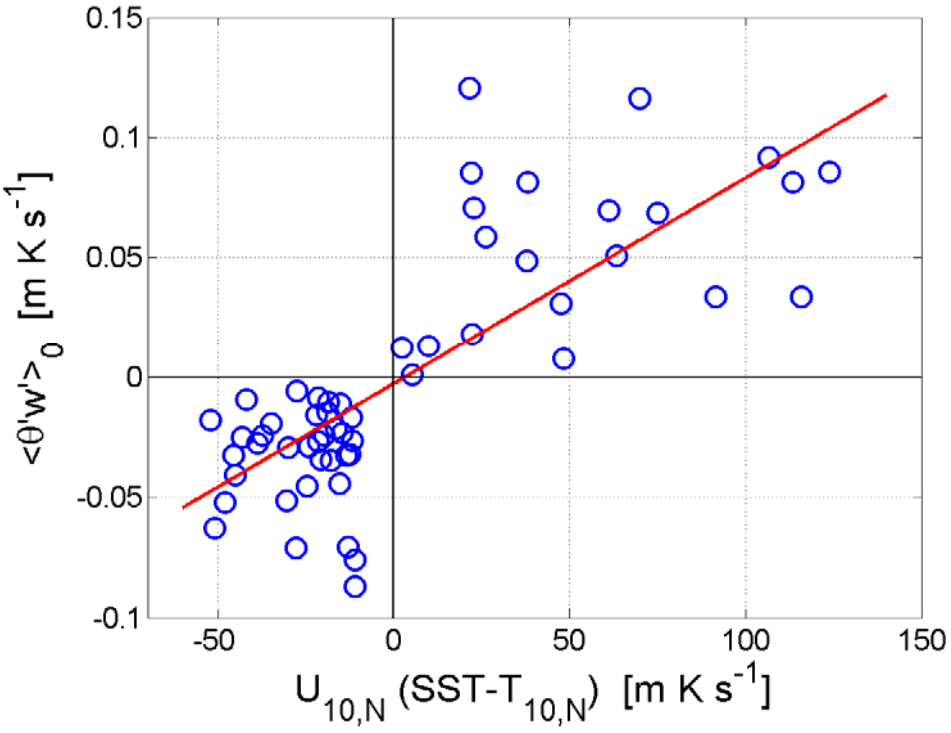

Fig. 3.7. Surface sensible heat flux $\overline{w'\theta'}$ as a function of $U_{10N}(\Theta_0 - \Theta_{10N})$. The red line indicates the best-fit linear regression line.

Figure 3.8 shows the 10 m neutral Stanton numbers versus U_{10N}. The mean value of the 42 points is $(1.1 \pm 0.07) \times 10^{-3}$, showing 1 standard error. Again, this is close to the HEXOS result. Statistical analysis shows that there is no dependence of the Dalton and Stanton numbers on the surface wind speed. These do not differ significantly with the existing data such as the HEXOS results (Decosmo et al., 1996).

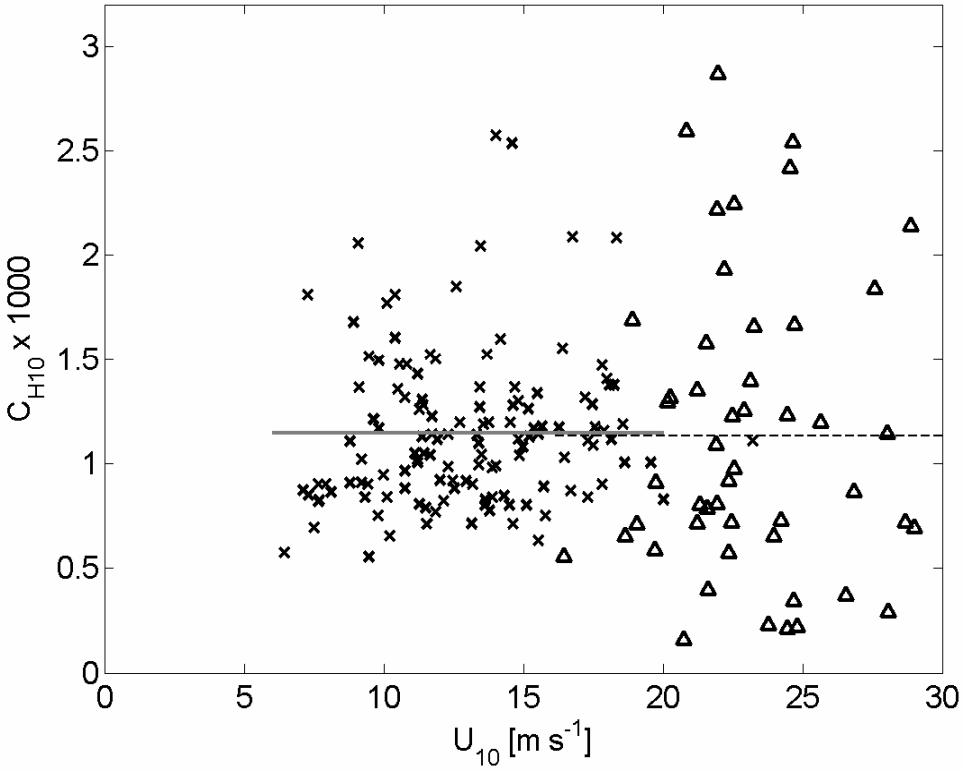

Fig. 3.8. Plot of 10-m neutral Stanton number as a function of 10-m neutral wind. The CBLAST data points and mean value are shown with Δ and dashed line, respectively. The HEXOS data (DeCosmo et al., 1996), shown with × and the solid line, have been corrected according to Fairall et al. (2003).

3.2.4 Enthalpy Flux

Theoretical study (Emanuel 1986) and numerical experiments (Ooyama 1969; Rosenthal 1971; Emanuel 1995) showed that the intensity of a hurricane depends strongly on the ratio of C_K/C_D, where C_K is the exchange coefficient of enthalpy flux. Results from numerical simulations using an axisymmetric tropical cyclone model (Emanuel 1995) demonstrated that to make the intensity of the simulated hurricane realistic, the

ratio C_K/C_D mostly lies in the range of 1.2-1.5 with C_K/C_D=0.75 as a lowest bound to ensure model consistency. To test this hypothesis, the exchange coefficients of enthalpy flux are also estimated using direct eddy correlation method as follows:

$$F_K = \rho\overline{k'w'}, \tag{3.7}$$

$$C_K = F_K / [\rho U_{10N}(k_0 - k_{10N})], \tag{3.8}$$

where F_K is the specific enthalpy defined as $k = c_pT + L_vq$, where T is ambient temperature, and k_{10N} and k_0 are the specific enthalpy at 10 m and the surface, respectively.

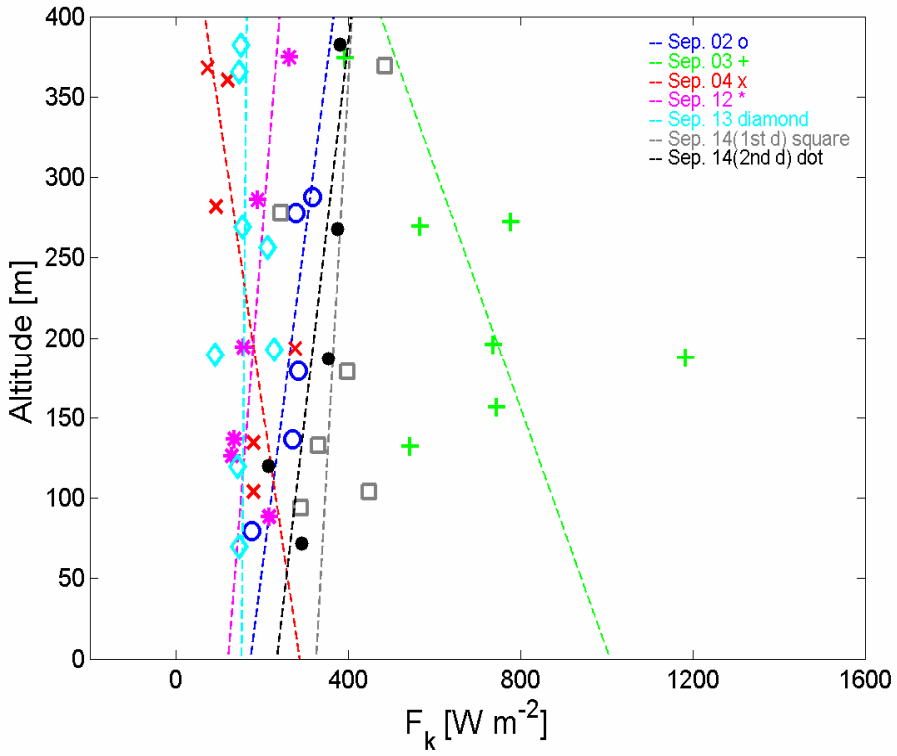

Fig. 3.9. Plot of the specific enthalpy flux versus altitude z for CBLAST stepped descents. Only descents with 4 or more altitudes are used. The symbols are as in Fig. 3.6.

Fig. 3.9 shows the profiles of $\overline{k'w'}$ in the boundary layer where each profile represents a stepped descent. Again only profiles with four or more points are used. The mean and standard deviation of these regression slopes are calculated as -0.0001 ± 0.00033, indicating that there is no significant height dependence of $\overline{k'w'}$ in the boundary layer. In the same way as the treatment of surface latent heat flux, the measured enthalpy flux is regarded as the indicative of surface values.

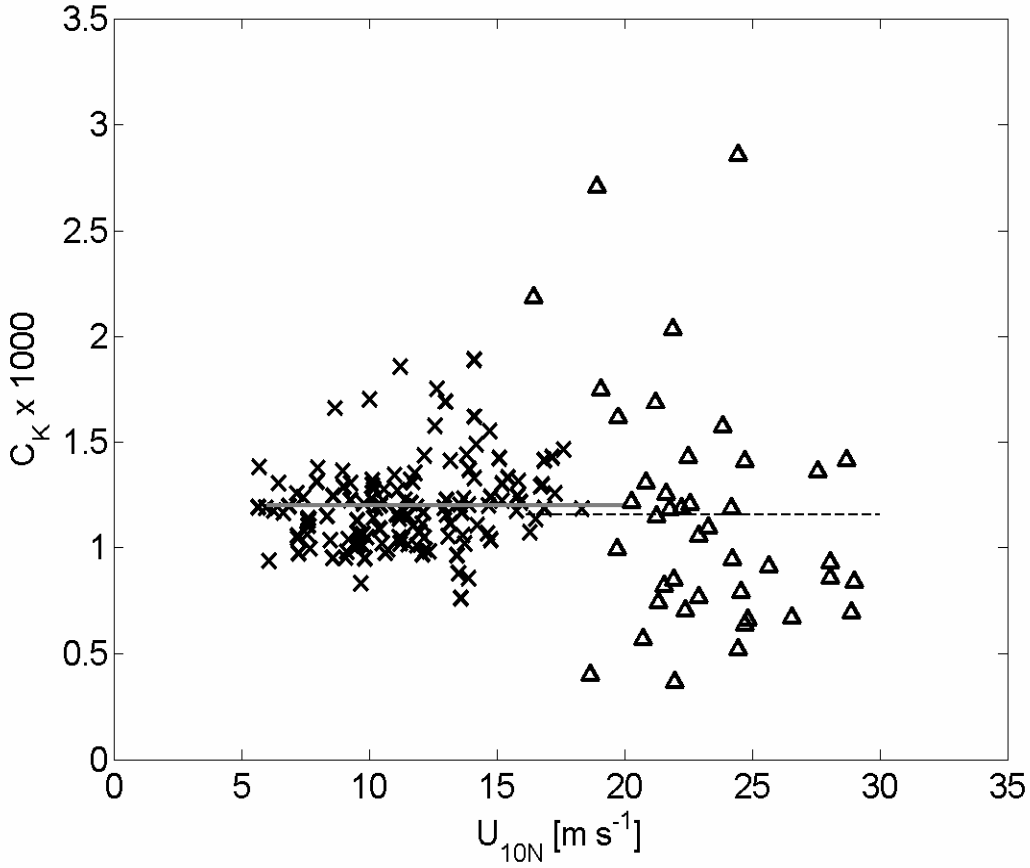

Fig. 3.10. Plot of 10-m neutral exchange coefficient of enthalpy as a function of 10-m neutral wind. The CBLAST data points and mean value are shown with Δ and dashed line, respectively. The HEXOS data (DeCosmo et al. (1996), shown with × and the solid line, have been corrected according to Fairall et al. (2003).

Fig. 3.10 shows the CBLAST neutral 10-m exchange coefficients of enthalpy versus wind speed. The mean value of the 42 points is $1.15 \pm 0.08 \times 10^{-3}$, showing 1 standard error. The HEXOS results are also shown. Here C_K from HEXOS are calculated based on the sensible and latent heat flux data as provide by J. DeCosmo (personal communication, 2005). The mean value of the HEXOS data is $1.18 \pm 0.04 \times 10^{-3}$. Statistical study on the CBLAST C_K shows that there is no significant dependence of it on the wind speed up 30 m s^{-1}.

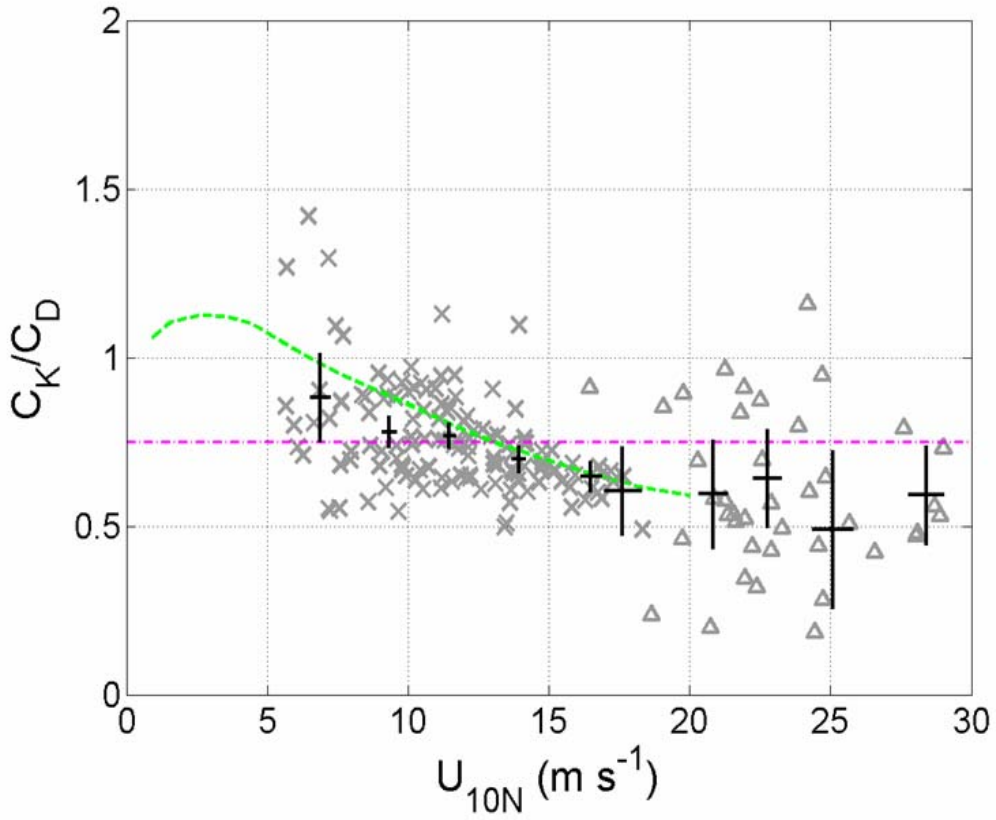

Fig. 3.11. Wind speed dependence of C_K/C_D total heat exchange coefficient. Data from CBLAST (Δ), and HEXOS results (x) are shown. After binning observations by wind speed the mean and 95% confidence intervals of the combined HEXOS and CBLAST field data are shown in black. Revised COARE 3.0 relationship is shown as the green dashed line. The threshold value of 0.75 suggested by Emanuel is also shown as the dash-dotted purple line.

Fig. 3.11 shows the ratio of C_K/C_D versus wind speed for the flux runs with both momentum and enthalpy flux measurements. The average of the C_K/C_D values is 0.67 which is significantly below the Emanuel (1995) threshold for hurricane development of 0.75. This suggests that the ratio of C_K/C_D in hurricane conditions could be lower than Emanuel's threshold used in his numerical models. That means that the assumption of treating the boundary layer as a single layer without vertical mixing parameterization may not be enough to simulate the hurricane intensity accurately. On the other hand, a further increase of the wind speed range is required to validate flux estimates in hurricane-force wind conditions, where physical processes may depart significantly from tropical storm wind conditions as the importance of sea spray and other poorly understood phenomena such as roll vortex features may increase dramatically.

3.3 Error Analysis for the Turbulent flux Measurement

It is evident from the plots of the exchange coefficients that there is much more scatter or variability in the CBLAST data than the earlier, lower wind datasets. Several factors could lead to either systematic or random error in our estimates of momentum, sensible heat and latent heat flux, and their exchange coefficients. The sampling error of a turbulent flux in stationary conditions is usually given by

$$\sigma_F / \overline{F} = \alpha_F z^{1/2} U^{-1/2} \gamma^{-1/2}, \tag{3.9}$$

where F is a given turbulent flux, σ_F is the standard deviation of flux estimates, α_F is a constant, U is the speed of advection of turbulence past the probe in m s^{-1}, γ is the

sampling duration in s, and z is the altitude where measurements are taken (e.g. Sreenivasan et al., 1978). For $F = \overline{q'w'}$, the estimate of α_F is around 6.4 (Sreenivasan et al., 1978).

During GASEX when conditions were mostly stationary (z = 6.5; U =6.1; γ =1800), the measured variability $\sigma_F / \overline{F} = 0.18$ is well predicted by (9), which gives 0.16. For HEXOS, the measured variability of 0.22 considerably exceeds that predicted (0.10), likely an indication of the varying conditions during the 7-week-long HEXOS campaign. The CBLAST measurements were carried out at considerably higher altitudes (z=60-400 m), higher relative wind speeds ($U \approx 110$ m s^{-1}) and shorter durations ($\gamma \approx 270$ s) than the surface-based ones. Again using (9), the expected variability in the CBLAST data is 52% that is consistent with the measured variability of 38%. Hence we conclude that the higher observed variability in the CBLAST data is consistent with the CBLAST sampling.

There are a variety of factors that could lead to systematic bias in the measurements. Considering the sensors themselves, as discussed above in Chapter 2, each compared well with independent aircraft sensors; for example, the LI-COR with the dewpoint hygrometers, the Rosemount and BAT velocities, the various motion packages. Furthermore, the algorithms were coded and run largely independently by two groups (Miami and Oak Ridge) with excellent agreements. Also the criteria for evaluating the quality of each run were initially derived independently by each group. It is thought that sensor and algorithm errors are no larger than in typical studies.

For the sensible heat and humidity flux measurements, a possible bias is the lag time applied to w before correlating with q or θ to obtain the flux. For the correlation of

w and q, the selected time lag ($\varsigma = 0.20$ s for the BAT and ς_R = 0.30 s for the Rosemount, with the 0.1 s difference between two due to horizontal displacement of the two systems) is based on our estimate for flow rates through tubing plus the delay in internal LI-COR processing. To check the sensitivity of the calculated fluxes to ς, the fluxes were recalculated for different values of ς from 0 to 0.5 s. At the lower values, $\varsigma \approx 0 - 0.1$ s, the $w'-q'$ velocity cospectra exhibited negative contributions at high frequencies, contrary to what is expected from the universal cospectra (Kaimal et al., 1972). Based on these calculations, the estimated mean error in our flux estimates due to time lag effects ranges from -2.8% (ς=0.15) to +4.2% (ς=0.3), with no dependence on wind speed. For the sensible heat flux calculation, the time lag ς=0.5 s is used following Friehe and Khelif (1993).

Mann and Lenschow (1994) and Mahrt (1998) discuss how short flight legs can yield systematic underestimates of covariance fluxes. In this study, the shorter flight legs are mostly due to the limitations of flight leg length imposed by the operational need for clear air. Under hurricane conditions, it is not easy to find a clear rain free area. All runs were thoroughly checked using ogive and cumulative sum analyses as mentioned in Chapter 2. Only runs passing these tests (thereby indicating that all low frequency scales are captured) were used in the analysis. Mahrt (1998) identified an additional error due to deviations of the aircraft from constant altitude. During a typical CBLAST run, the average standard deviation about the nominal altitude is 7.8 m. The error results from what is essentially a Gaussian displacement distribution over a logarithmic mean humidity gradient. A thorough analysis of the problem by Mahrt et al. (2005) indicated this problem to be small, $O(1\%)$, except in very stable conditions.

The use of SFMR winds for U_{10} is clearly a potential source of error. The SWEMODv2 algorithm, developed and validated using an extensive set of near surface dropsonde winds, claims an accuracy of 2% at 30 m s^{-1}, or $\pm$ 1.5 m s^{-1} (Uhlhorn et al., 2007). A mean bias of 2% in U_{10N} could yield a similar bias in C_{E10N} and C_{H10N}. In contrast, the use of profile derived winds instead of SFMR wind could yield a 5% reduction in Dalton number and Stanton number. We conservatively consider 5% as the uncertainty due to the surface winds for Stanton number and Dalton number estimates.

The single largest potential source of bias appears to lie with the radiometric SSTs. The PRT-5 has a stated accuracy of ± 0.5 °, consistent with the corrections applied on N43RF by Burnes et al. (2000) during the TOGA COARE experiment. A sensitivity analysis indicates that biases in SST of [+1°, +0.5°,-0.5°,-1°C] would lead to biases in mean C_{E10N} of [-24%, -14%, +19%,+51%], respectively. We are able to constrain the bias by plotting the measured surface heat flux (covariance of potential temperature with vertical velocity) against the product $U_{10}(\Theta_0 - \Theta_{10})$ as shown in Fig. 3.7, indicating SST biases $O|0.5°|$C or greater are ruled out. Another error is from the assumption that the surface wind speed U_0 is near zero, which could contribute approximately 5% bias in the enthalpy exchange coefficients if the surface wind velocity is larger than 2 m s^{-1}. However, till now there is no direct measurement of currents and wind velocity near the sea surface in hurricane conditions. Considering all factors, an uncertainty of $\pm$ 25% in our mean Dalton and Stanton number estimates seem to be a conservative estimate. A similar uncertainty should apply to the bulk enthalpy coefficient.

For the drag coefficient estimates, one issue likely to contribute most significantly to errors in our estimates is that the height-based correction of Donelan (1990) applied to

our data to obtain a surface friction velocity. We estimate that an uncertainty of 10% for the friction velocity can be induced by this correction, which could result in approximately 20% uncertainty in the drag coefficient. The use of the SFMR winds could lead to at least 4% uncertainty in the drag coefficients. Additionally, assuming the surface wind velocity is zero could lead to 5% uncertainty in the drag coefficients. Taking into account these possible sources of error, we estimate an uncertainty of 30% in our measurements of drag coefficient.

3.4 Variability of Surface Fluxes

This section discusses the variability of the surface fluxes by storm quadrant according to the variation of stability and sea state. The CBLAST surface flux data are compared with the simulation results from the Fully Coupled Atmosphere-Wave-Ocean model of University of Miami (Chen et al., 2007). The variability in the wind stress and wind direction is also discussed.

As mentioned earlier, only data during the 2003 hurricane season are obtained within the lower boundary layer (70 – 400 m) of cat 4 and 5 storms with direct measurements of surface fluxes of both momentum and enthalpy. These data were essentially collected in three storm quadrants as shown in Fig. 3.12, where the horizontal aircraft flight tracks are rotated with respect to the storm direction and superimposed on top of the GOES image. In Fig. 3.12, each color represents each flight day. In addition, a

WP-3D Lower Fuselage (LF) airborne radar image from NOAA 43 of Isabel at 1642 UTC is overlaid indicating typical eyewall and rainband structure.

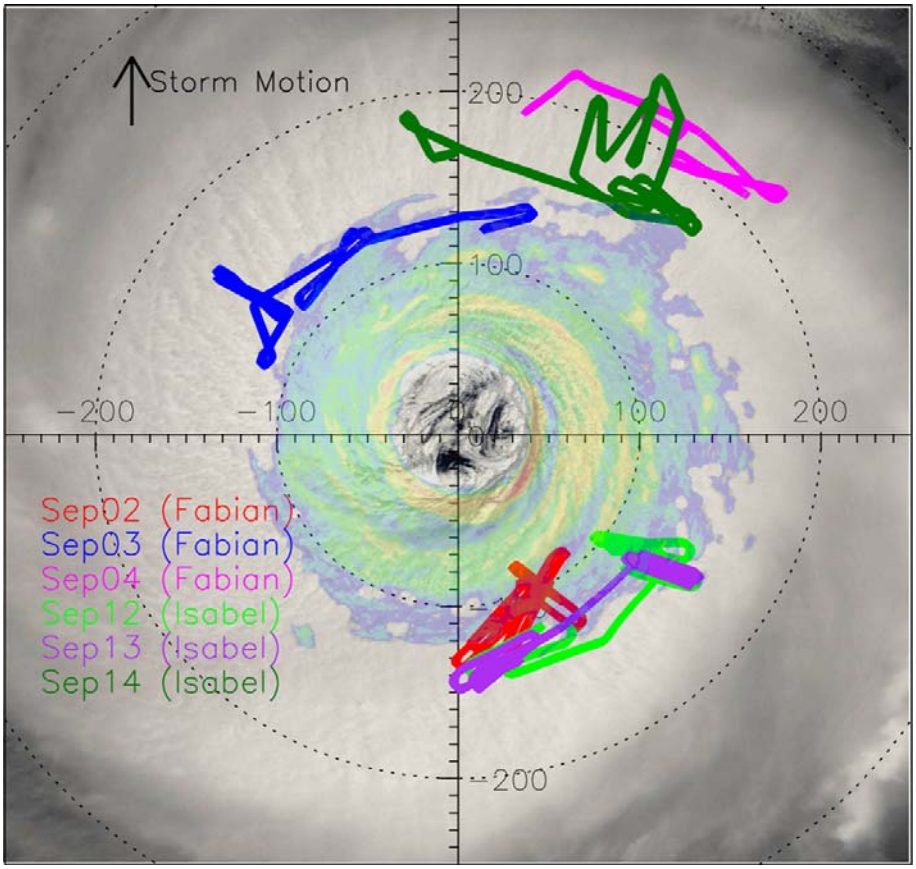

Fig. 3.12. CBLAST stepped descent flight patterns flown in Hurricanes Fabian and Isabel in 2003, plotted in storm-relative coordinates, with the storm motion indicated by the arrow (up). Circles are shown at 100 km intervals. Flight tracks are superimposed on a NASA MODIS visual image of Hurricane Isabel on 14 Sept, 2003 at 1445 UTC. In addition a WP-3D Lower Fuselage (LF) airborne radar image from NOAA 43 of Isabel at 1642 UTC is overlaid indicating typical eyewall and rainband structure. MODIS image courtesy of MODIS Rapid Response Project at NASA/GSFC.

Fig. 3.13 shows the vertical profiles of the buoyancy fluxes ($\overline{\theta_v' w'}$) for the six flights in the 2003 season. The colors in Fig. 3.13 are consistent with those in Fig. 3.12 for each flight. In general, the buoyancy flux increases linearly with a decreasing height. The behavior of the buoyancy flux profiles provides the estimate of the stability. The flights into hurricane Fabian are within three quadrants, the left front, right front and right rear quadrant, while the flights into hurricane Isabel are within two quadrants, the right

front and right rear quadrant. Fig. 3.13 shows the variability of the surface buoyancy flux by the storm quadrant. The boundary layers at the right front and right rear quadrants are nearly neutral with a near zero buoyancy flux. The boundary layer at the left front quadrant is a little bit unstable but still nearly neutral since the buoyancy flux is relatively small compared to the shear stress.

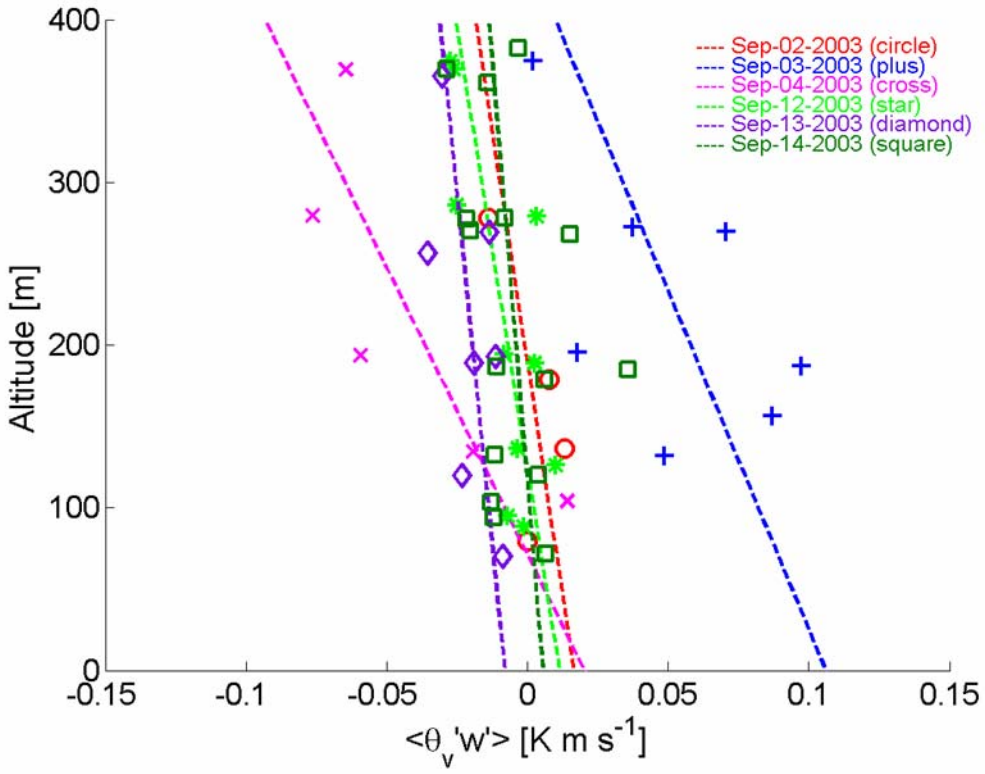

Fig. 3.13. Vertical profiles of the buoyancy flux. Each color represents a flight day. Only descents with 4 or more altitudes are used. The symbols represent the different descents: 20030902: o, 03: +, 04: x, 12: *, 13: ◊, 14-1: □. The dashed lines represent slopes for each descent.

In Fig. 3.13, only the boundary layer at the right rear quadrant of hurricane Isabel on 12th September 2003 is slightly unstable. This is possibly due to the cooling effect that usually takes place in the right rear quadrant of a storm caused by the strong ocean mixing. However, it is also shown that this cooling effect may not always cause a slight

stable boundary layer as the boundary layer at the right rear quadrant of hurricane Fabian on 2 September 2003 is slightly unstable. The reason why the cooling effect in the Hurricane Isabel case is more predominant is that the sea surface temperature in the ocean Hurricane Isabel passed is lower than that of Hurricane Fabian since Hurricane Fabian passed the same area ten days before Isabel as shown in Fig. 3.14. Overall, it can be postulated that the boundary layer in the rain free region between the outer rain bands is nearly neutral to slightly unstable. Although hurricanes draw energy from the ocean through upward transported enthalpy flux, a slightly stable boundary layer with negative buoyancy flux could occur at the right rear quadrant.

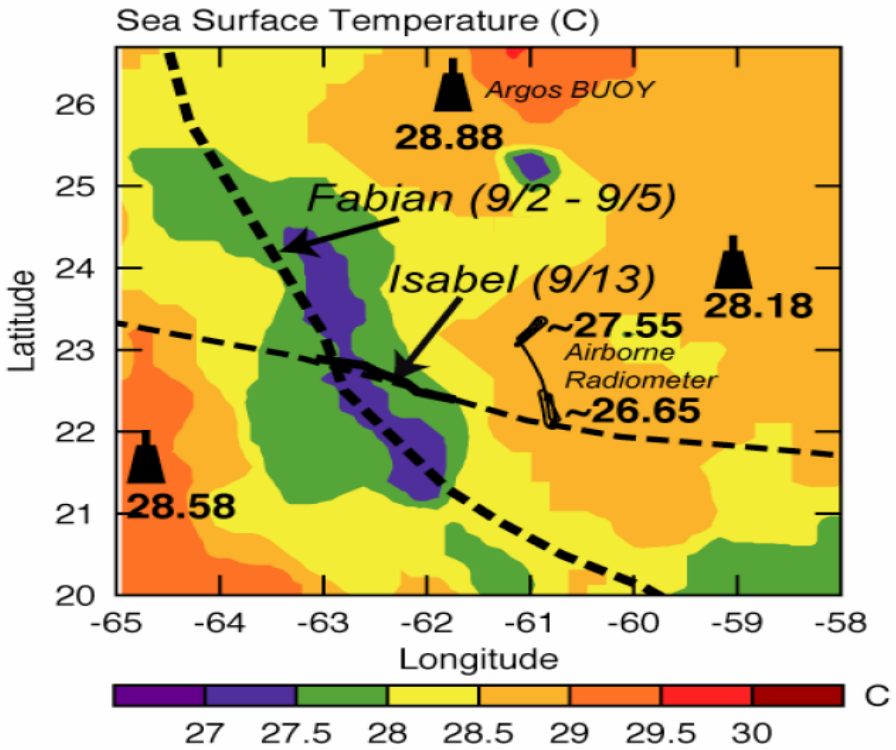

Fig. 3. 14. SST derived from AVHRR satellite averaged from 4 to 10 September 2003 in color, ARGOS buoys, and NOAA P-3 downward pointing radiometer (thin line, from 18UTC, 13 September). Tracks of Hurricanes Fabian and Isabel are also shown. See Fig. 5 in Montgomery et al., 2006.

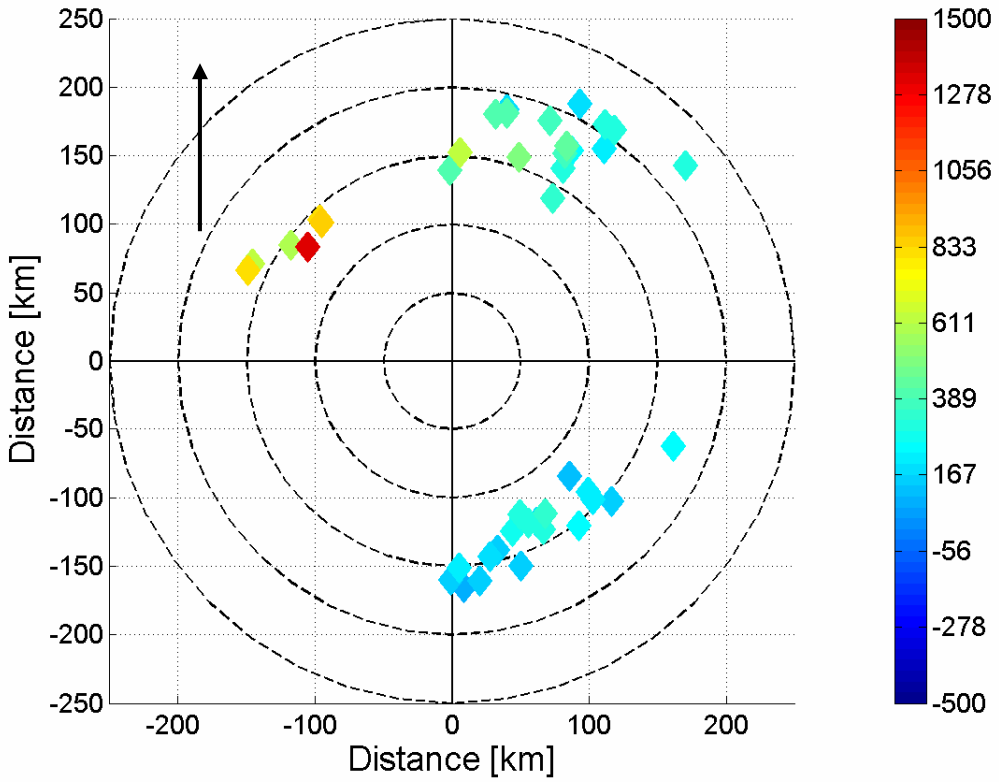

Fig. 3. 15. Variability of enthalpy flux (color in W m^{-2}) by storm quadrant. Black arrow represents the storm direction.

Fig. 3.15 shows the variation of the surface enthalpy flux by storm quadrant. Data from 42 flux runs during the 2003 hurricane season are shown here. The magnitude (in color) of the enthalpy flux is around 200 – 1000 W m^{-2}. It is also shown in Fig. 3.15 that there is an asymmetric distribution of the enthalpy flux with respect to the storm quadrant. Within the similar distance to the storm center, the left front quadrant has the highest enthalpy flux, while the right rear quadrant has the lowest one. This finding is consistent with the simulation result from the Fully Coupled Atmosphere-Wave-Ocean Model as shown in Fig. 3.16. Compared to the observation, the new generation fully coupled model shows a good ability to capture the surface enthalpy flux. With a higher resolution of 1.67

km, it could demonstrate in detail the distribution of the surface fluxes. With the coupling to the underlying ocean, its results represent the physics near the air-sea interface, so it can be a good tool to interpret the physical processes where the observation did not cover. For instance, during the CBLAST experiment, only three storm quadrants were measured. The coupled model-simulated results could be used in the future to study the air-sea energy transport at the left rear quadrant.

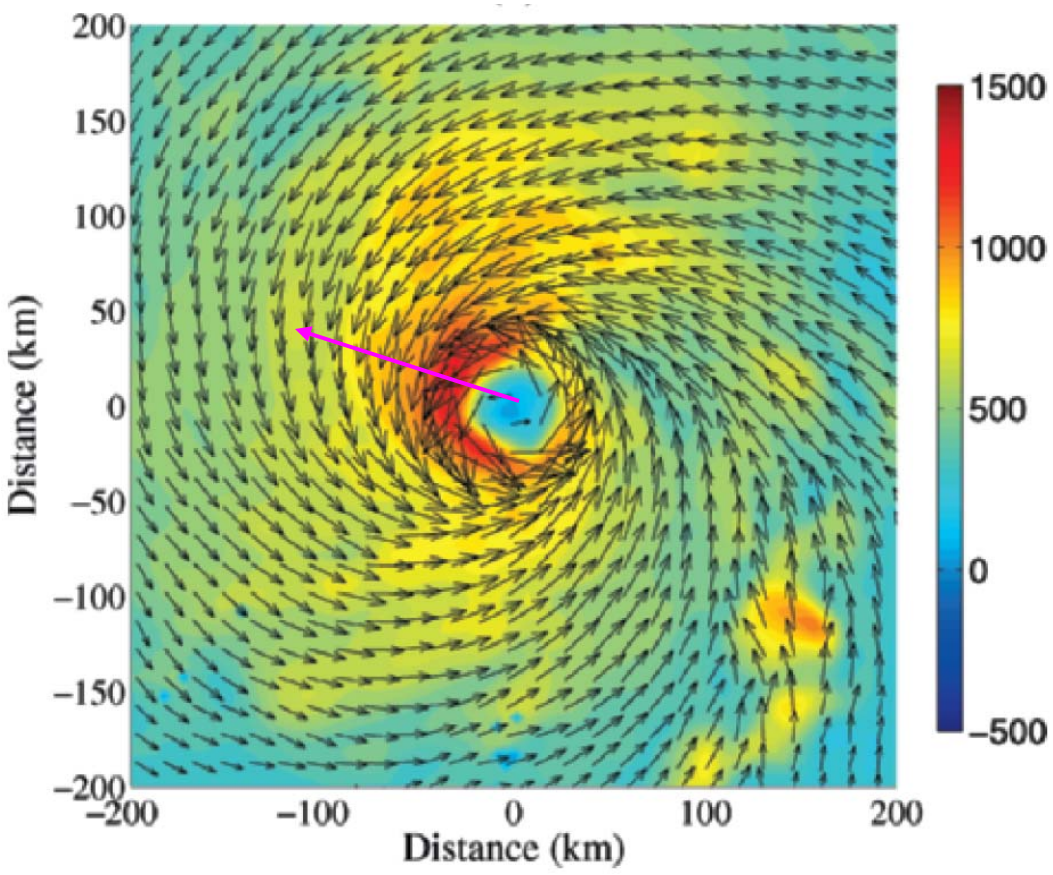

Fig. 3.16. Coupled model simulated enthalpy flux (color in W m^{-2}) by storm quadrant. Purple arrow represents the storm direction. Black arrows represent wind direction. Figure is from b) of Fig.3 in Chen et al. (2007).

One reason of the asymmetry of the enthalpy flux is due to the asymmetry of the air-sea temperature difference by storm quadrant. Especially at the right rear quadrant, the air-sea temperature difference tends to be smaller than that of the remaining quadrants due to the cooling effect assuming a homogeneous environment. Given the nearly constant exchange coefficients with wind speed in this region, the smaller the air-sea temperature difference the smaller the enthalpy flux. Another reason is due to the asymmetry of the surface wind. According to the storm motion, the wind speed at the left quadrants tends to be larger than that at the right quadrants. When the exchange coefficients for enthalpy are nearly constant with wind speed as shown in section 3 of this chapter, the higher the wind speed the larger the enthalpy flux.

Fig. 3.17 presents the variability of the friction velocity which is equivalent to the square root of wind stress by storm quadrant. It shows the asymmetry of the wind stress similar to that of the enthalpy flux. The left front quadrant has the highest wind stress while the right rear quadrant has the lowest one. This is mostly due to the asymmetry of the wind speed. However, the drag coefficients that relate the wind stress and wind speed do not show the same quadrant distribution (Fig. 3.18). Although it has been shown from surface wave observations (Black et al., 2007) that the waves are young, steep and short in the right rear quadrant, and older, flatter, and longer in the right front and left front quadrants, the exchange coefficients of momentum flux did not exhibit the variability that depended on the characteristics of the 2D wave spectrum.

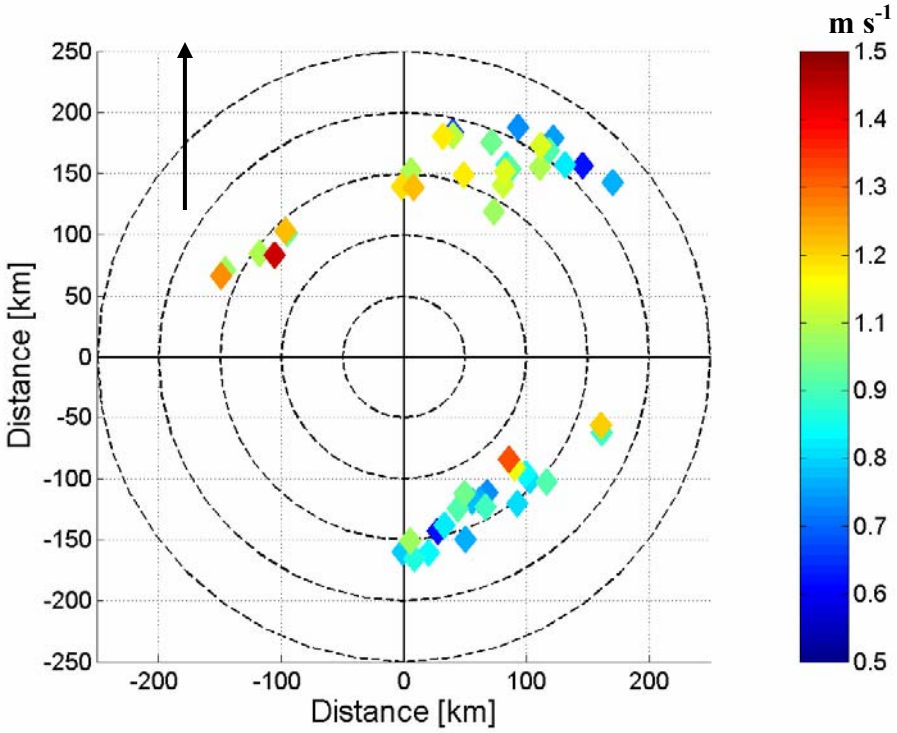

Fig. 3.17. Variability of the friction velocity by storm quadrant. Black arrow represents the storm direction.

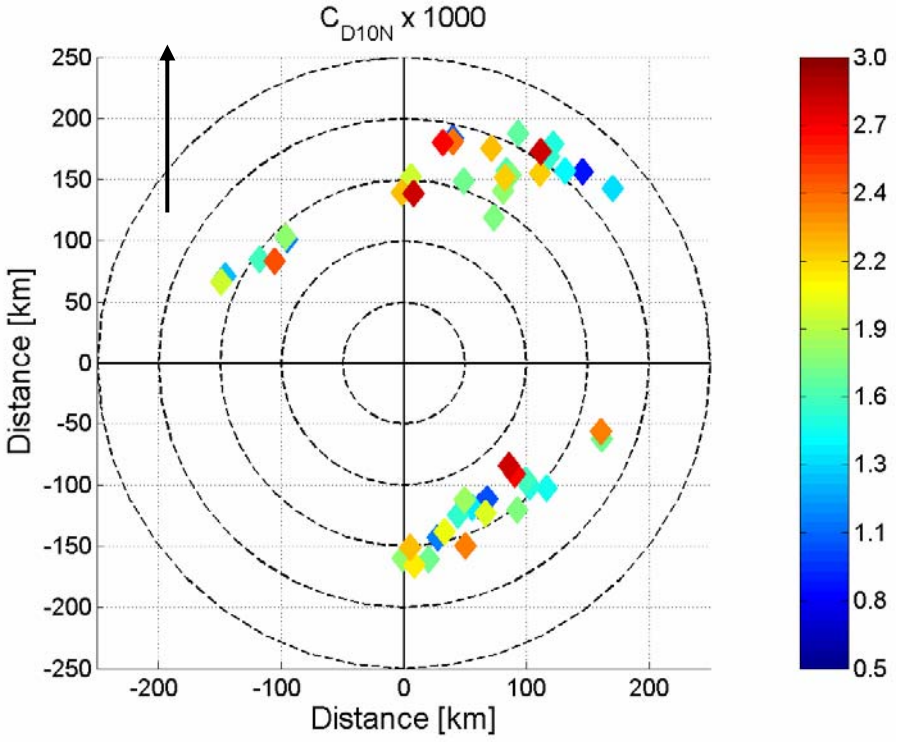

Fig. 3.18. Variability of the drag coefficient by storm quadrant. Black arrow represents the storm direction.

At the end, discussion is made on the deviation of the wind stress direction from the wind direction. Fig. 3.19 shows the wind direction as a function of the wind stress direction for the 2003 data grouped by storm quadrant. In this study, the wind stress direction is not aligned with the wind direction. There is an approximately 10-20 degree difference between them. At the left front quadrant, the angle between the wind direction and wind stress direction is smaller that those at the right quadrants.

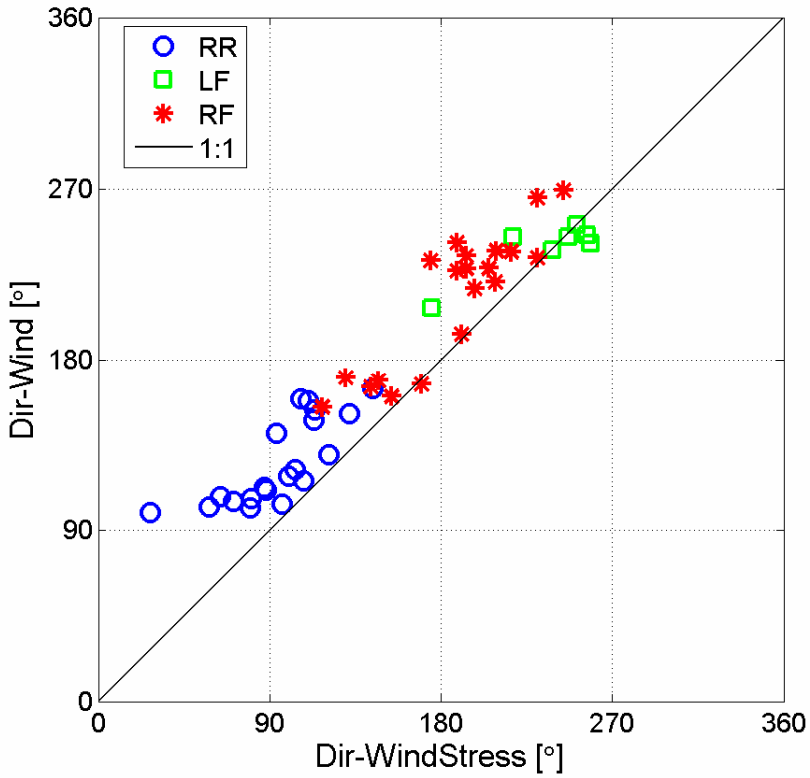

Fig. 3.19. Wind direction versus wind stress direction. Data are separated by storm quadrant as shown in the legend.

In the Monin-Obukhov similarity theory, it is usually assumed that the wind stress vector follows that of the wind. However, several experimental studies including this work show that the stress direction over the ocean often deviates significantly from

the mean wind direction. There are several mechanisms that may be responsible for this difference, such as the surface heat flux (Geernaert et al 1988), the direction of long waves or swell (Grachev et al 2003), and surface currents (Drennan and Shay, 2005). Under hurricane conditions, the wave field near the air-sea interface is more complicated that elsewhere, since the wind is very high rotating while the storm is moving.

It is well known that the wind stress is an important boundary condition for atmospheric, wave and oceanic models. The wind stress is also one of the important forcing for the ocean waves. Understanding of the wind-wave-current interaction processes has become a crucial part to improve the model ability of simulating the surface waves, storm surges and hurricane intensity. To qualify the wind stress direction near the air-sea interface in hurricanes, a dedicated field experiment is needed with the direct measurements of all the forcing parameters including the wind stress vector, wave, surface currents and heat flux.

Chapter 4

Rolls

4.1 Introduction

Roll vortices in the atmospheric boundary layer (ABL) have been studied in a number of early theoretical and field studies (e.g., LeMone, 1973; Brown, 1970; Etling and Brown 1993; Glendening 1996; Weckwerth et al. 1997). For reference also see the review article of Young et al. (2002). Depending on their size and strength, roll vortices have the potential to play a significant role in transporting momentum, heat and moisture through the atmospheric boundary layer. Failing to adequately sample these coherent structures could easily lead to an under (or over) estimation of boundary layer fluxes. Recent remote sensing observations show that roll vortices may be common in the hurricane boundary layer (HBL). It has been suggested that the periodically spaced damage patterns observed during hurricane landfalls are associated with the enhancement of surface friction or momentum flux caused by the HBL rolls (Fujita, 1992; Wakimoto and Black, 1994).

Previous studies indicate that Synthetic Aperture Radar (SAR) can provide useful information for identifying atmospheric mesoscale variations, such as the ABL rolls

(Alpers and Brumer, 1994; Mourad, 1996; Mourad and Walter 1996; Brümmer, 1999; Müller et al., 1999; Levy, 2001). The coherent structures of rolls can cause distinctive alternation of the ocean surface roughness on the cm-scale that can be sensed by SAR via the change of the Bragg wave spectrum. Katsaros et al. (2000) report on the examination of a few RADARSAT SAR images from four hurricanes (Bonnie, Danielle, George, and Mitch) in 1998. This was the first year of operations for RADARSAT, a program sponsored by the Canadian Space Agency. In addition to the identification of numerous effects of rain and convective rainbands, Katsaros et al. also recognized features they attributed to roll vortices in the surface wind in regions between rainbands. By examining SAR images of Hurricanes Mitch and Floyd, Katsaros et al. (2002) found similar periodic variation in sea surface roughness as that induced by roll vortices. Some aspects of SAR observed coherent roll-scale features are also discussed by Vachon and Katsaros (1999) and by Friedman et al. (2004).

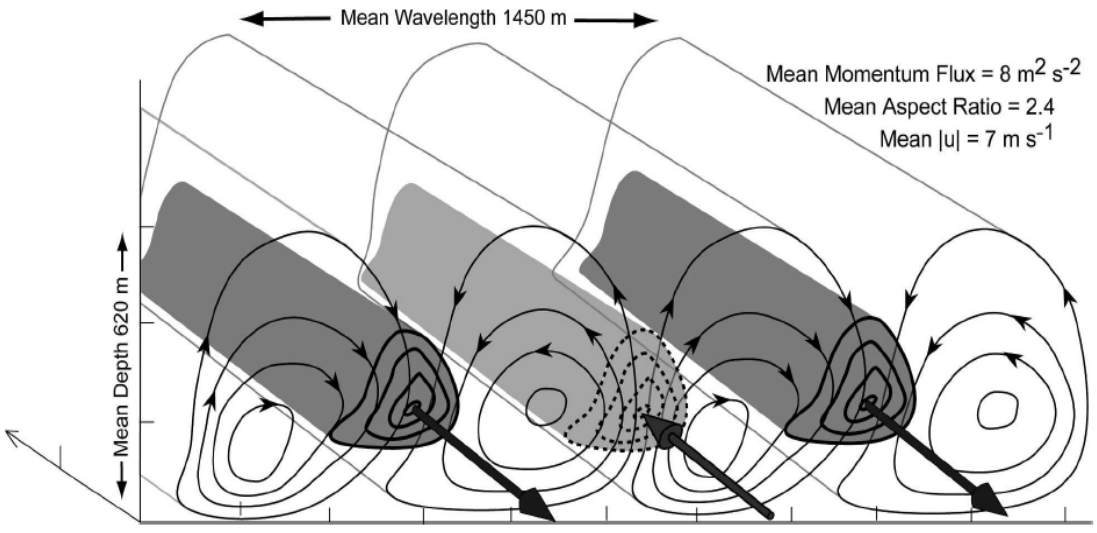

Fig. 4.1. Schematic depicting hurricane boundary layer rolls observed during four hurricane landfalls. Streamline arrows indicate transverse flow, with high (low) momentum air being transported downward (upward). Shaded arrows and bold contours indicate the positive (black) and negative (gray) residual velocities. See Figure 8 of Morrison et al., 2005.

Intense sub-kilometer-scale rolls in the HBL have been inferred from coastal radar observations (Wurman and Winslow, 1998). Recently, Morrison et al. (2005) reported on new observations made by airborne radar. They identified roll vortices in 35 to 69 percent of the radar volumes of four hurricane landfalls with typical roll wavelengths of 1450 m, aspect ratio of 2.4, and azimuthal wind variations of about 7 m s^{-1}. A schematic diagram of the rolls measured by Morrison et al. (2005) is shown in Fig. 4.1. Consistent with the above observations, Foster (2005) has developed a theory for roll vortices in curved flow at high wind speeds, such as in hurricanes. Adapting the boundary layer model to cylindrical coordinates, Foster (2005) determined that rolls were likely to develop in hurricanes and could make significant contributions to fluxes of momentum, heat and water vapor.

ABL rolls have also been previously investigated through research aircraft (LeMone 1976, Chou and Ferguson, 1991; Brooks and Rogers, 1997; Savtcthenko, 1999; Chen et al., 2001; Vandemark et al., 2001), but there is no aircraft investigation of rolls in hurricanes coincidently with turbulent flux measurements. In this Chapter we report the first in-situ turbulent flux measurements during the event of roll vortices in the HBL. The main purpose is to investigate the significance of roll vortices on the transport of energy across the air-sea interface and through the hurricane boundary layer. Section 2 describes the satellite data employed and the analysis of a RADARSAT-1 SAR image captured in the area of the boundary layer aircraft measurements during Hurricane Isidore. Section 3 presents the detailed aircraft measurements of rolls and turbulent flux in this storm. Finally, discussions are made in section 4.

4.2 Satellite RADARSAT-1 SAR Observation

SAR images provide a unique view of many physical processes in the upper ocean and within the marine atmospheric boundary layer (Katsaros et al. 2002). Spaceborne SAR is capable of providing a comprehensive view of the sea surface roughness at a resolution on the order of 10-100m. The variation in sea surface roughness can be explained in part by change in surface wind speed due to the formation of boundary layer rolls (Mourad et al., 2000; Sikora and Ufermann, 2004).

In the 2002-2003 Hurricane seasons, the Hurricane Watch program was established between the Canadian Space Agency (CSA) and Canadian Centre for Remote Sensing (CCRS) in collaboration with NOAA' Hurricane Research Division (HRD) flight planning team and the NOAA Aircraft Operations Center (AOC). In this program, tens of RADARSAT SAR images were obtained in hurricanes. We focus here on a RADARSAT-1 image (Fig. 4.2) collected in the area of the boundary layer aircraft measurements in Hurricane Isidore at 2357 UTC, on September 23, 2002. RADARSAT-1 is an HH-polarized C band (5.3 GHz) radar with nominal spatial resolution of 32 and 20 m in the azimuth and range dimensions, respectively (Vachon and Katsaros, 1999).

This image (Fig. 4.2) was precision processed after it was calibrated and corrected for power loss (Laur et al., 1998). Detailed algorithms of the analysis of the image are given by Lehner et al. (1998) and Lehner et al. (2000). In general, the image was split into subscenes of 20 kilometers (256 pixels of 50 m length and width). A Fast Fourier Transform (FFT) algorithm was then used to calculate the image spectra of these subscenes. For subscenes in which the maximum of the 2D spectrum is due to the wind

streaks or rolls, the direction of the rolls can be taken to be the wind direction (Morrison et al., 2005). Image pixels corresponding to land and some types of non-wind features are identified using the algorithm given by Koch (2004). The 180° ambiguity of the wind direction is also resolved. While up to this point the algorithm is standard for wind field determination from SAR imagery, here we focus on the wavelength of the rolls from which one can estimate of the depth of the mixed boundary layer.

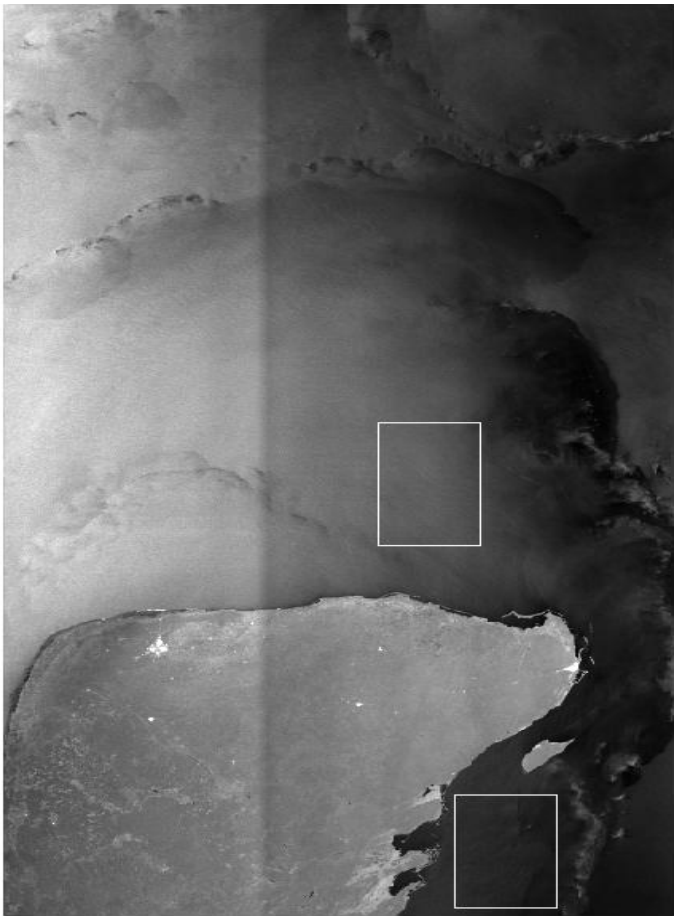

Fig. 4.2. RADARSAT-1 SAR image of hurricane Isidore acquired on September 23, 2002 at 23:57 UTC after landfall on the Yucatan Peninsula. Analyses of this image and the two boxes are shown in Fig. 4.3.

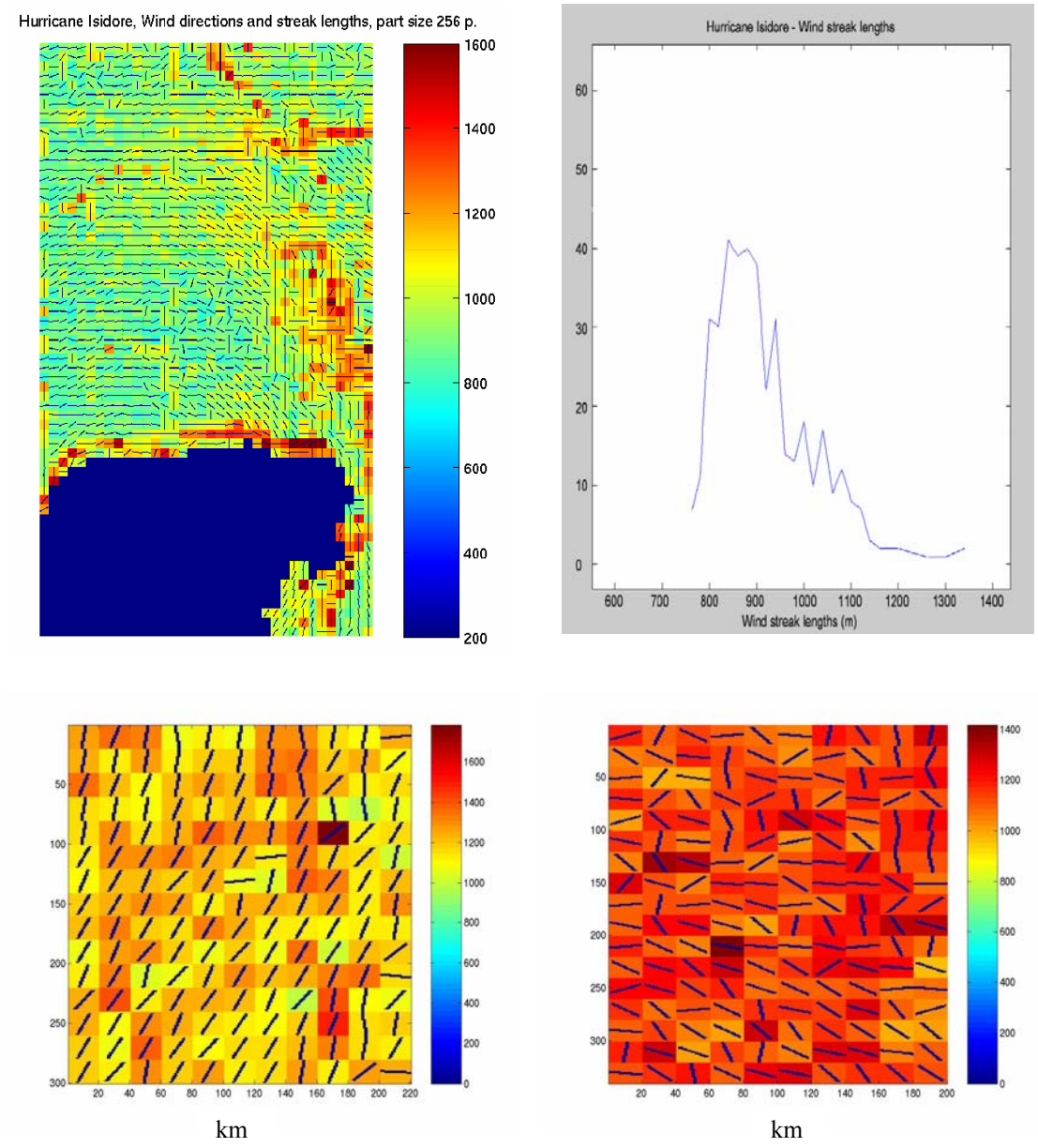

Fig. 4.3. Analysis result of the SAR image in Fig.4.2. The upper left panel shows the wavelength (color bar code, m) and direction of the wind rolls. Note that the vertical lines in the image are the artifacts either due to rain or problems with the original image. The upper right panel shows the histogram of the roll wavelengths of the entire image at left. The lower two (left/right) panels show the wavelength (color in m) and direction analysis of the (upper/lower) boxes in Fig. 4.2.

Figure 4.3 shows the analysis result of the SAR image. Our primary interest lies in the typical features of a mesoscale wind field on the sea surface in this case the wind streaks. The upper left panel of Fig. 4.3 shows the wavelength and direction of the wind streaks. Several artifacts due either to rain or problems with the original image (especially the vertical line of intensity change) are also seen, but are generally distinguishable from the roll features. The upper right panel shows the histogram (for the entire image) of the wavelength of the rolls with a maximum in the distribution of about 850 m. The lower two panels (left/right) demonstrate the analyses of the two boxes (upper/lower) of interest indicated in Fig. 3.26. The wavelengths of the rolls vary from around 800 to 1300 m, which illustrates that the scales vary within a storm.

4.3 Aircraft Observations

4.3.1 The Study Case of Rolls

The cases in this study of the HBL rolls are a subset of the measurements during the CBLAST-Hurricane experiment. Of interest to this study are data from boundary layer flight legs in Hurricane Isidore (2002). Tropical Depression Isidore was upgraded to a tropical storm at 6:00UTC, 18 September 2002 near Jamaica. It was upgraded to a hurricane 36 hours later, and made landfall in western Cuba at 20 UTC 20 September 2002 as a category 1 storm. Hurricane Isidore continued westward after leaving Cuba, and strengthened, maintaining category 3 (100-kt winds) status until making landfall in the Yucatan around 2000 UTC 22 September 2002. The storm center remained over the

Yucatan for the next 36 hours during which time it gradually weakened. Isidore re-emerged over the Gulf of Mexico later on 24 September as a tropical storm and made landfall again south of New Orleans 2 days later.

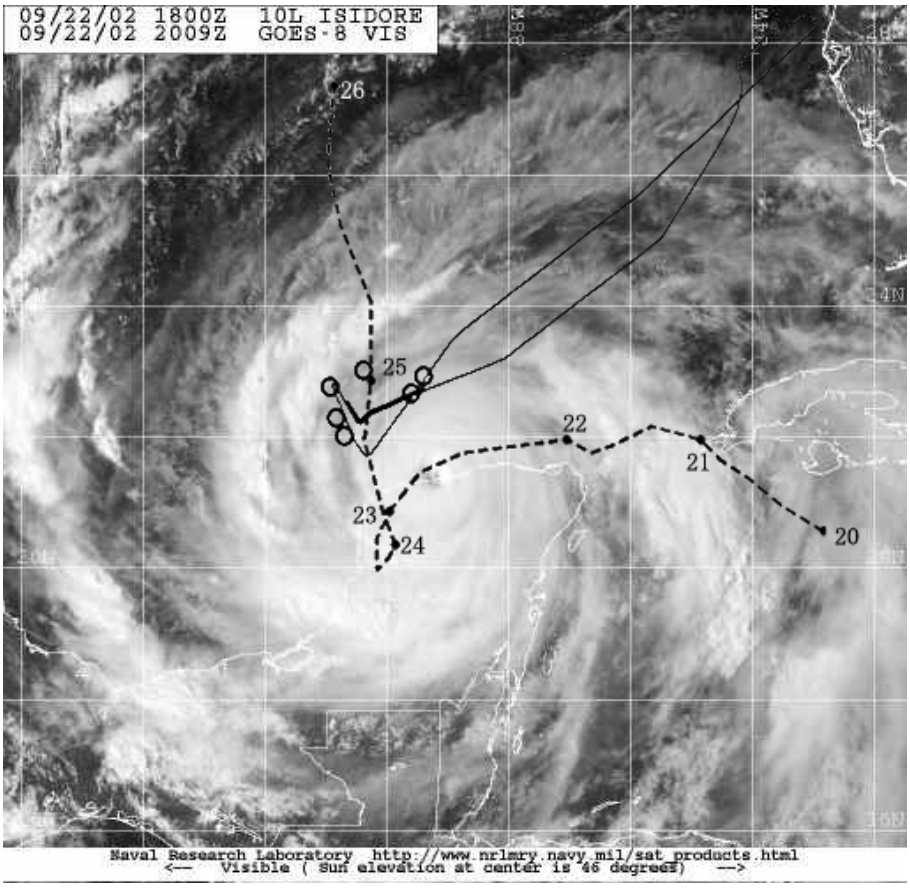

Fig. 4.4. P3 N43RF aircraft track (solid black line) on top of the GOES-8 visible image at 2009 UTC, on 22 September 2002, showing Hurricane Isidore several hours before the flight, image courtesy of Naval Research Laboratory, Monterey, CA. The dashed line shows the track of the storm from 20 to 26 September 2002, with numbers occurring at 0:00 UTC. Also shown are the release locations (o) of the dropsondes (Fig. 4.5) dropped from another aircraft N42RF.

The P3 Aircraft N43RF conducted missions into Isidore on 21, 22 and 25 September 2002. Of interest here is the N43RF flight on 22 September that occurred roughly 24 hours prior to the SAR over pass discussed in the previous section. At this

time the hurricane eye was situated at the northern edge of the Yucatan Peninsula. Superimposed on the boundary layer portion of the N43RF flight track in Fig. 4.4 is a GOES satellite image (VIS band). Boundary layer profiles of potential temperature and specific humidity retrieved from GPS dropsondes released in the vicinity of the boundary layer leg are shown in Fig. 4.5. Boundary layer depths were estimated from the potential temperature profiles to be around 400-500m (Stull 1988). The dropsondes were qualitatively selected based on their proximity to the P3 N42RF flight track, spatially and temporally. Dropsonde positions are also shown in Fig. 4.4.

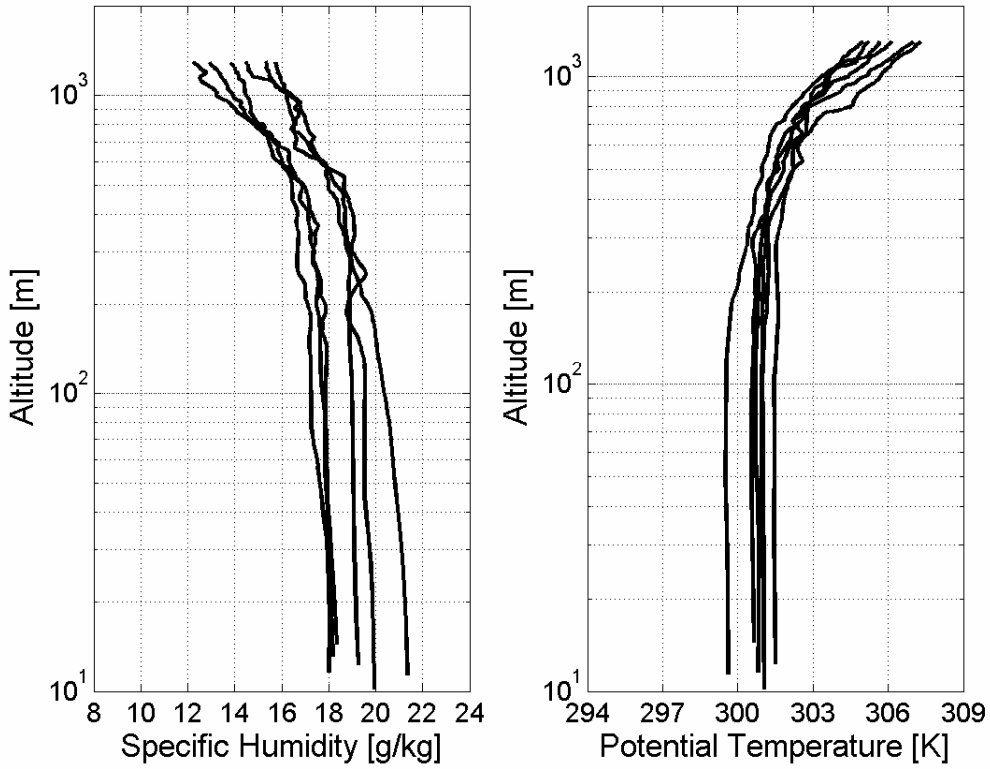

Fig. 4.5. Specific humidity (left) and potential temperature (right) from 6 GPS dropsondes dropped from N42RF in the vicinity of the 22 September 2002 boundary layer flight. The release points of the sondes are shown in Fig. 4.4. The profiles of specific humidity and potential temperature indicate the hurricane boundary layer depth is around 500 m.

Fig.4.6 presents the portion of the track between 2210 and 2240 UTC, and some of the parameters of interest such as aircraft altitude, wind speed, wind direction, and aircraft attitude angles. In Fig. 4.6 b), the black lines represent the five flux run legs denoted by A-E for reference hereafter. Flux run A is the nearly cross-wind leg (see panel e), B, C and D are the nearly along-wind legs, and E can be regarded as a transverse leg with an angle of around 40° between the aircraft ground track and the mean wind direction. Aircraft altitude and attitude angles (pitch, roll and heading) were checked and confined to a specific range in order to reduce the spurious values in the wind measurements caused by the sudden changes of these quantities. The entire low-level portion of this flight leg was confined to 200 and 350 m altitude and hence is within the HBL at all times.

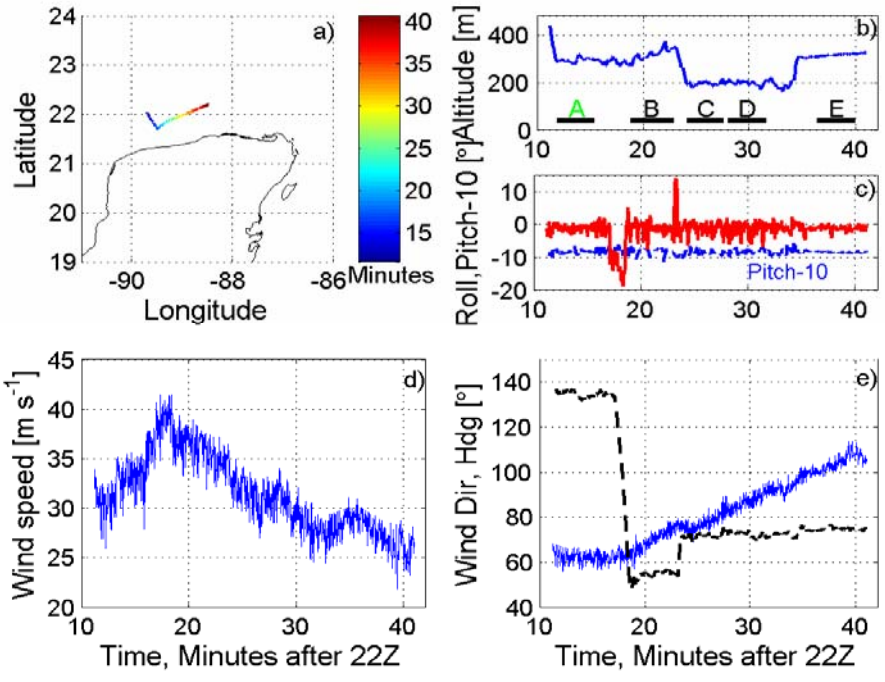

Fig. 4.6. N43RF flight track (a) during Hurricane Isidore on 22 September 2002, 22:10-22:42 UTC. Also shown are the aircraft altitude (b), pitch and roll (c), flight level wind speed (d), and aircraft heading wind direction (e).

4.3.2 Evidence of Rolls

All flux measurements were taken between the rain bands outside the eyewall. The boundary layer was under near neutral but slightly unstable thermodynamic conditions, which can be implied by the stability parameter z / L in Table 4.1. Previous theoretical and numerical studies suggest that this atmospheric environment is favorable to the formation of the roll vortices (Lilly, 1966; Brown 1980; Young et al., 2002; Foster, 2005). Table 4.1 summarizes the measurements and calculations for each of the five runs. Leg-averaged mean flight level wind speeds vary from 29 m s^{-1} to 35 m s^{-1}. The near-surface neutral-stability wind speeds (U_{10N}), determined from measurements by the SFMR, vary from about 19 m s^{-1} to 23 m s^{-1}. Sea surface temperature (SST) shown in Table 1 is measured by the infrared radiometer on the N43RF. Corrections of SST for water vapor path and reflected radiation have been made following the method discussed in Chapter 2. The SST during the flux measurements is nearly uniform implying that the underlying instability conditions are similar for all the five flux runs.

Table 4.1: Summary of data and calculations for the five flux run legs (A, B, C, D and E)

Leg	Leg Time	Length	Leg	z	U_z	U_{10N}	z/L	u	$C_{D,10N}$	θ_{10}	SST	<θ'w'>
	UTC	(km)	Type	(m)	(m s-1)	(m s-1)		(m s-1)	(X 10^3)	(K)	(°C)	(K m s-1)
A	22:10:48-22:15:05	24.6	cross	293	32.4	21.6	-0.001	1.08	2.51	301.5	27.4	0.028
B	22:18:30-22:22:40	24.5	along	319	35.3	23.0	-0.023	1.04	2.06	301.7	27.2	0.037
C	22:23:56-22:27:25	24.3	along	194	30.2	21.1	-0.017	0.98	2.17	301.5	27.1	0.036
D	22:27:45-22:31:20	24.4	along	196	29.1	20.3	-0.023	0.88	1.89	301.7	27.1	0.025
E	22:36:40-22:39:50	24.3	along	315	28.8	18.1	-0.023	0.81	2.05	301.4	27.0	0.022

Fig. 4.7 shows the time series of the turbulent fluctuations of the three components of the wind velocity (u', v' and w') that are bin-averaged to 1 Hz, fluctuations of the potential temperature (θ') and absolute humidity (q'), and productions ($w'\theta'$ and $w'q'$) for the cross-wind flux run A. Both high and low frequency variations can be observed in the time series. In the product plots the periodic variations imply that mesoscale coherent structures may exist in this storm (LeMone 1976).

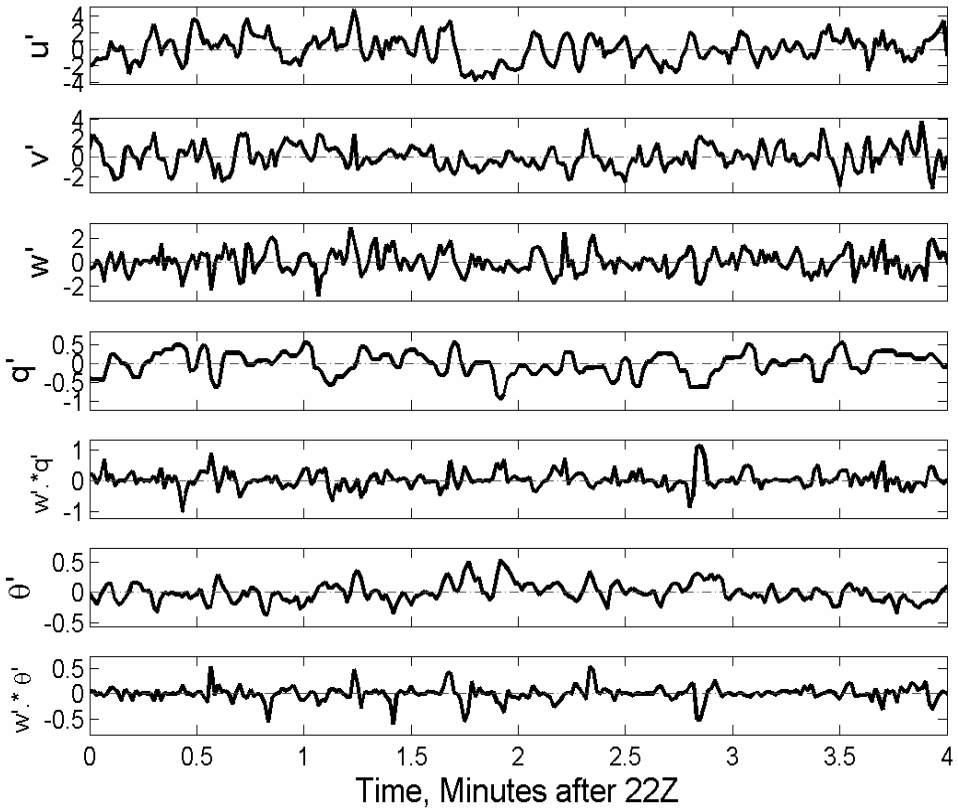

Fig. 4.7. Data from the cross-wind leg A, showing time series of the bin-averaged (1 Hz) fluctuations of three dimensional wind velocities, the (1 Hz) potential temperature and absolute humidity, and productions of the fluctuations. Note that the three component wind velocities and potential temperature are collected in 40 Hz. The 1 Hz data here are shown to indicate the periodic variations in the production plots.

Figure 4.8 shows the spectra of u', v', w', θ', and q' for the cross-wind leg (A) which has a length of about 25 km. There are significant peaks in the spectral plots of all the variables at 0.13 Hz. Given an aircraft speed of around 100 m s^{-1} and accounting for a 80° track angle relative to the wind, this would be equivalent to a wavelength about 950 m. A number of small peaks between 0.3 and 1 Hz (100 and 330 m) are shown in u', v', w' and θ' spectra, which can be related to the smaller-scale plumes and less organized turbulence. There is no smaller-scale turbulence signal above 0.5 Hz in the power spectra of q' due to the lack of fast response humidity sensor during the 2002 measurements.

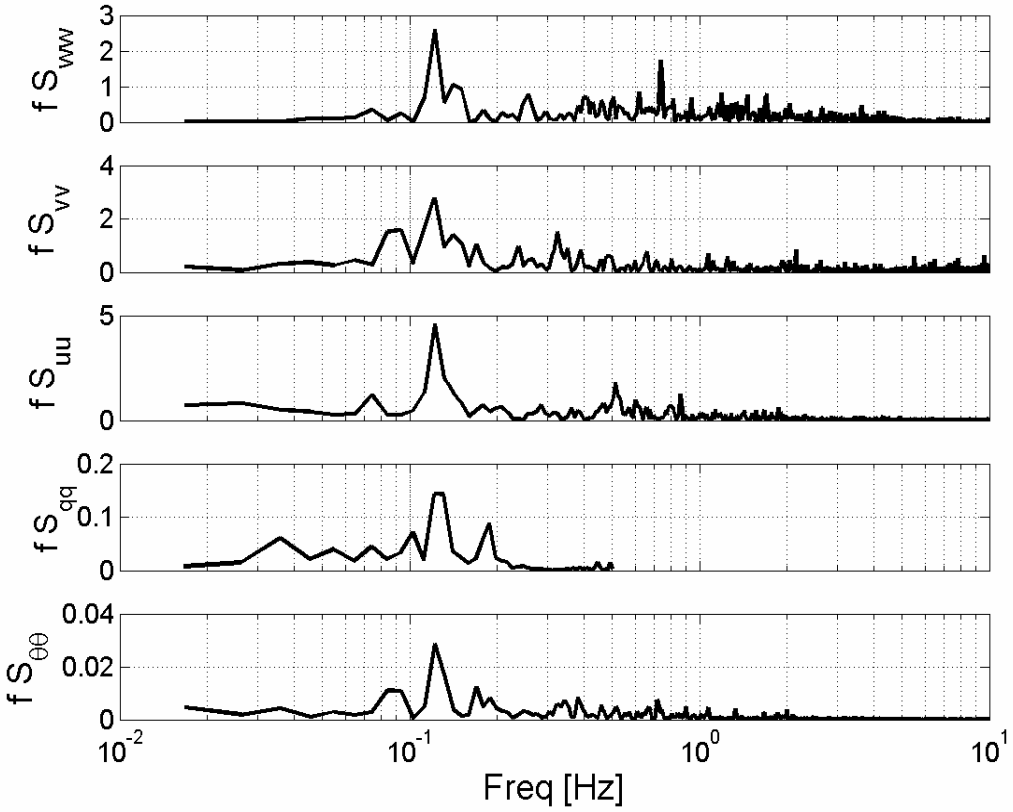

Fig. 4.8. Data are from the cross-wind leg A, showing spectra of three component velocities, potential temperature and humidity.

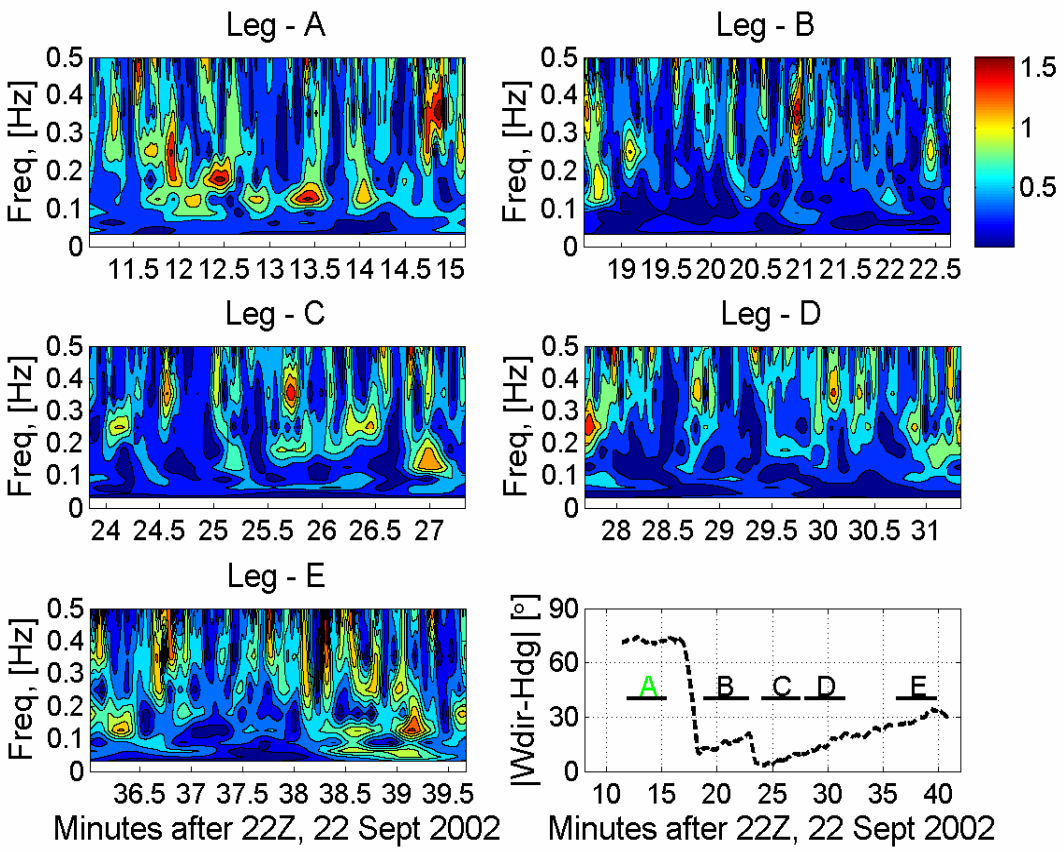

Fig. 4.9: Contour plots of wavelet coefficient amplitude squared of the vertical velocity against time and frequency. The five sections (A-E) of the boundary layer flux run on 22 September 2002 into hurricane Isabel were analyzed separately. The absolute angle between the aircraft heading and the wind direction is also shown in the lowest right panel.

To confirm the presence of rolls during the aircraft measurements, a Morlet wavelet transform (Grossmann and Morlet, 1984) was applied to the vertical velocity signals. A wavelet transform allows for the decomposition of a signal in both frequency and time domain, hence can be used to study the evolution of features (e.g., Farge, 1992). Fig. 4.9 shows the amplitude squared (i.e., energy) of the wavelet coefficients for the five flux run legs and the angle between the aircraft heading and the wind direction. Note in particular the enhanced energy patterns in the wavelet plot during the cross-wind flight leg A in the frequency band around 0.13 Hz, which we suggest corresponds to roll

features on scales of approximate 950 m which is consistent with the SAR measurement discussed before. That such coherent features are only infrequently observed in the subsequent near-along-wind and transverse legs, is consistent with identification of these features as roll vortices. The rolls are generally lined up in the wind direction (i.e., Young et al., 2002; Morrison et al., 2005; Foster, 2005), therefore, are less frequently encountered in flights close to the wind direction.

4.3.3 Spectral Analysis

The main objective here is to study the importance of roll circulations in transporting momentum, sensible heat and humidity in the hurricane boundary layer. As seen in Fig. 4.8 for leg A, all spectral plots have higher spectral densities in the frequency band f=0.1-0.16 Hz and peak at the frequencies near f=0.12 Hz. Similarly, the cospectra in Fig. 4.10 show the peaks at nearly the same frequencies within f=0.1-0.16 Hz, indicating a coherent roll structure. The peak frequencies within the roll frequency band, to which the roll wavelength of 950 m is equivalent, show good agreement with the SAR measurements. Considering the boundary layer depth indicated by the potential temperature profile about 400-500m, the aspect ratio of these rolls is about 1.8-2.2.

The influence of scale on the fluxes can be studied by dividing the covariance into three spectral regions: f<0.1 Hz, f=0.1-0.16 Hz and f>0.16 Hz. The low-frequency band f<0.1 contains larger or mesoscale eddies, the roll-frequency band f=0.1-0.16 contains roll vortices, and the high-frequency band contains smaller scale eddies and turbulence of the inertial subrange (Chou and Ferguson, 1991). Given that the roll-scale contributions

are equal to the difference between the total fluxes and non-roll fluxes (Glendening 1996), the integral of the cospectrum over the roll-frequency band that corresponds to the roll-scale flux could be 30-50% of the total fluxes of momentum. The cospectral plots in the lower panels of Fig. 4.10 indicate the warmer drier air is transported downward near the downdraft branches and the cooler wetter air strongly penetrates near the updraft branches. That indicates that roll circulations carry air parcels with q and theta highly negatively correlated, and therefore transfer sensible heat downward and moisture upward.

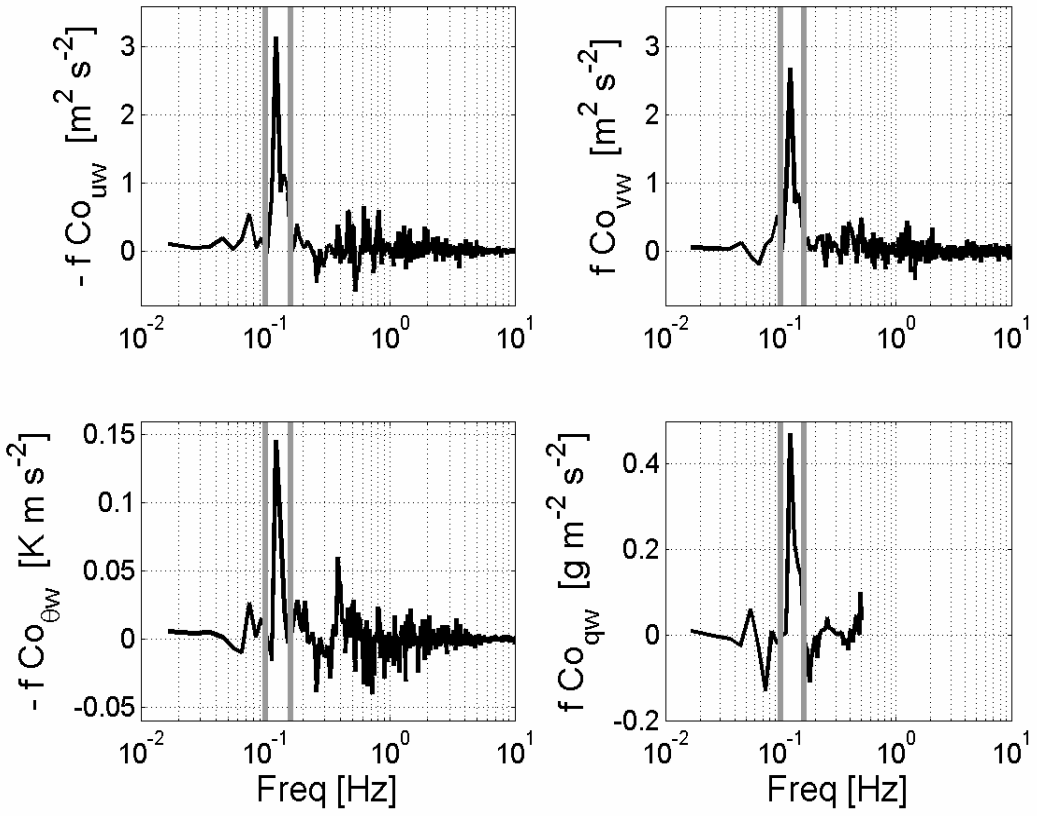

Fig. 4.10. For the cross-wind leg A, Cospectra of the vertical velocity w with the horizontal wind velocity components u and v, potential temperature and humidity. The vertical gray lines indicate the roll-frequency band. Note negative sign on θw spectrum.

The normalized cumulative cospectral sum or ogives (Friehe et al. 1991) for the along- and cross-wind components of momentum flux for the five flux runs are shown in Fig. 4.11. Here the solid green line represents the cross roll leg (A), the dashed black lines represent the near-along-roll legs (B, C and D), and the dash-dotted line represents the transverse roll leg (E). The curves are normalized by the square of $U_{10,N}$ to remove the effect of changing wind speed. One aspect of particular interest here is the normalized cospectra ogive, comparable to the 10 m neutral drag coefficient shown in table 1. It is 20% higher for the cross-wind leg than for the mean of the along-wind legs.

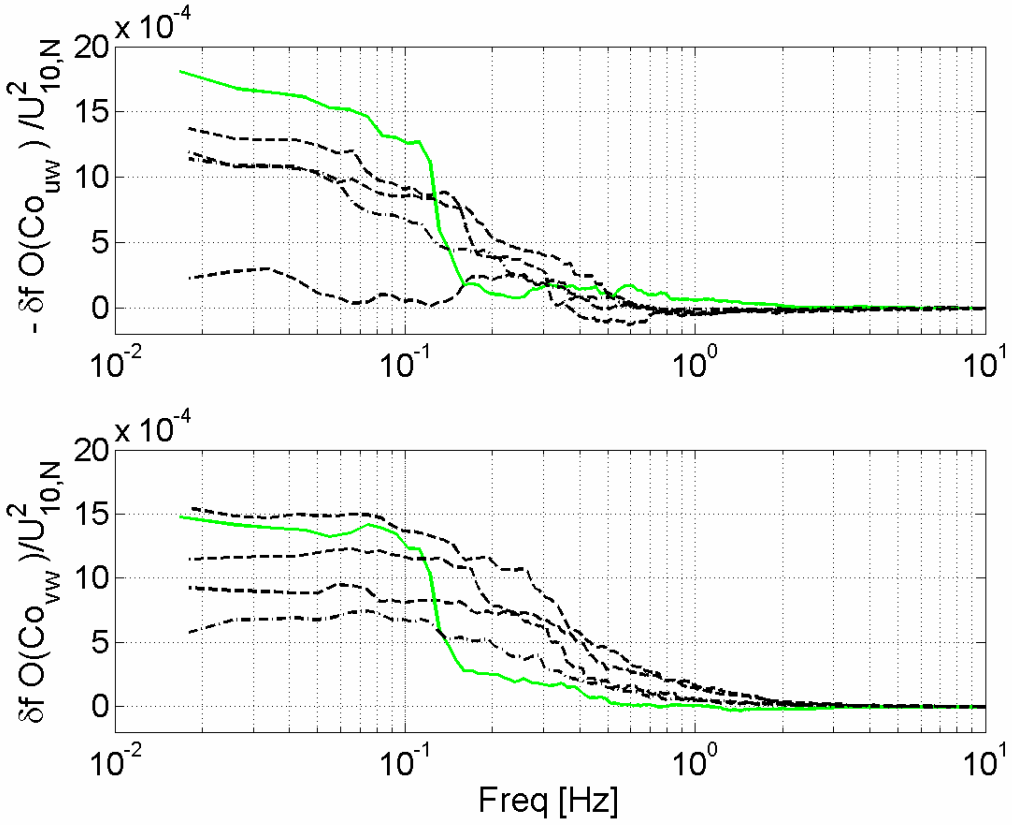

Fig. 4.11. Cumulative cospectral sum (ogives) of the alongwind and crosswind components of the momentum flux for the N43RF boundary layer flight. Here, the solid green line represents the cross-roll leg (A), the dashed black lines represent the three near-along-roll legs (B, C, and D), and the dash-dotted gray line represents the transverse-roll leg (E). Note that the curves are normalized by $U^2_{10,N}$ to remove effect of changing wind speed. The curves that have been multiplied by the step frequency δf are equivalent to the 10 m neutral drag coefficients.

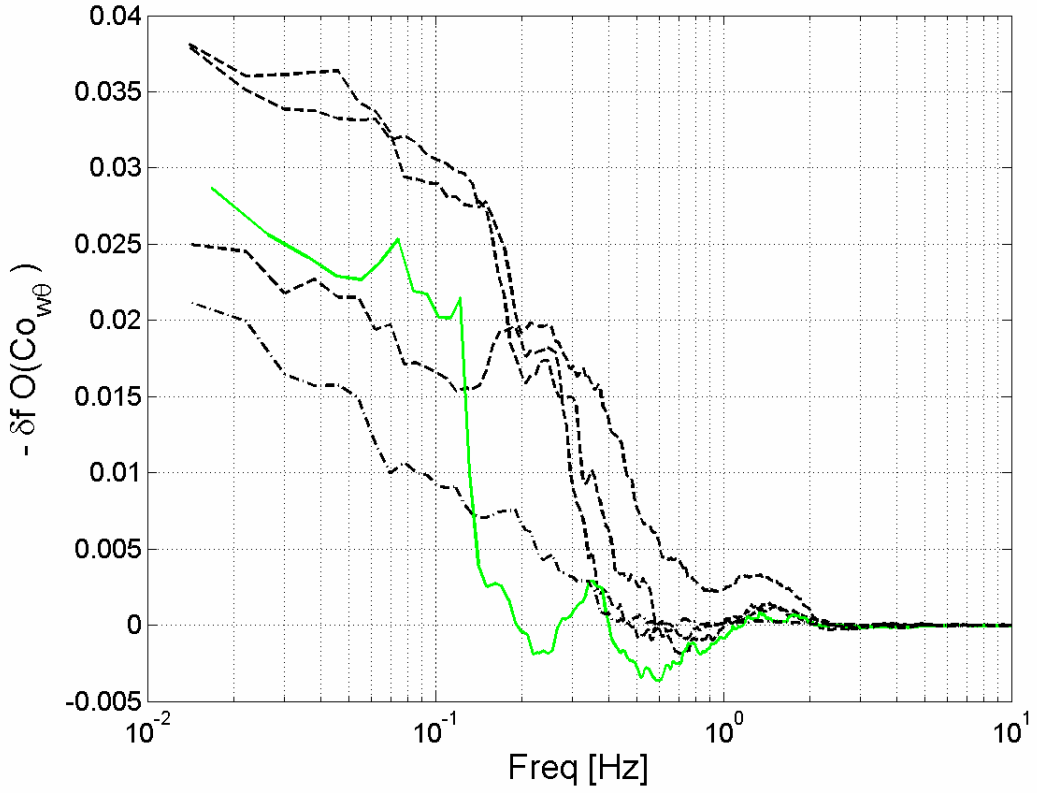

Fig. 4.12. Cumulative cospectral sum of the sensible flux for the 22 September 2002 N43RF boundary layer flight. Symbols are as in Fig.4.11.

Fig. 4.12 shows the ogives for the sensible heat flux of the five flux runs. The nearly continuous ogive plots of the along-wind legs converge at the low frequency around 0.01 Hz indicating the along-wind flux runs are under nearly stationary condition which is one of the critical assumptions in air-sea interaction theory (Donelan 1990) in developing the standard parameterization of turbulent fluxes. However, the remarkable variations in the ogive plot of the cross-wind leg show the non-local contribution of rolls to the total flux as discussed earlier on the cospectra of sensible heat flux. Ogives in air-sea interaction study are often used to detect the stationarity or homogeneity of a flux run, thus such a flux run with unexpected changes in the ogive plots is usually eliminated in

calculating the turbulent fluxes using eddy correlation method (French et al., 2007). That is to say, the non-local contribution of rolls to the flux could not be captured by the standard boundary layer parameterization used in the hurricane models.

Moreover, Fig. 4.12 shows that the sensible heat flux for the cross-wind leg is nearly equal to the mean of that for the along-wind and transverse legs, indicating that the modulation of rolls to the sensible heat flux at the middle of the boundary layer is not significant compared to the momentum flux. Although the surface sensible heat flux and the exchange coefficient for heat can not be estimated due to the lack of the stepped descent flight pattern, the influence of rolls to the exchange coefficient of sensible heat flux is expected to be small given the underneath uniform SST and near surface environments during the flux measurements. It seems that the rolls redistribute the sensible fluxes in spatial scale but transport vertically similar amount of them in mean.

4.4 Discussion

Results from an aircraft case study together with the SAR data analysis have been presented in the above 2 sections. This case study indicates that the presence of a spectral subrange of rolls in the hurricane boundary layer could contribute to the net air-sea fluxes. The flux of momentum across the hurricane boundary layer containing rolls is larger than flux predicted by the standard parameterizations of turbulence. This supports the theory of rolls by Foster (2005) that the HBL rolls may contribute a significant fraction of the total downward momentum flux. It is also shown from the spatial analysis of SAR data

that the wavelength of the rolls matches that of the aircraft measured rolls. The aspect ratio of the rolls measured in this study ranges between 1.8 and 2.2 for both the SAR and aircraft measurements, which is in very good agreement with the result of Morrison et al. (2005).

While earlier research by both numerical models and observations shows a profound effect on surface stress (the momentum flux) in the hurricane boundary layer, little was found about the roll effects on the enthalpy flux. Here, we investigated the effect of rolls on the sensible heat flux. At the middle of the boundary layer, rolls tend to rescale eddies that transport heat flux. The net effect of rolls on the sensible heat flux seems to be small. We also show the highly correlation of sensible heat and moisture at the roll scale in the cospectra plots. Given the asymmetry of the roll circulations postulated by Foster (2005) with much stronger and narrower updraft regions of rolls, we expect that the modulation of rolls to the humidity flux could be higher. Due to the lack of a fast response humidity sensor in the 2002 field season, the effects of rolls on the exchange coefficients of enthalpy (heat and humidity) and the influence of rolls on the ratio of C_K/C_D or hurricane intensity are still unknown. But we show that rolls could rescale the turbulent eddies and thus influence the turbulent flux measurements. As mentioned in Chapter 2, the flux runs are generally short (around 24 km) during the CBLAST measurements, so fluxes measured through ensemble average of turbulent fluctuations could be either overestimated or underestimated when rolls exist. Modulation of rolls on the turbulent fluxes is likely to be the major reason for the large scatter of the exchange coefficient plots.

One of the main aims underlying the CBLAST-hurricane experiment was to measure the surface turbulent fluxes in hurricane conditions in order to develop a new bulk parameterization of these fluxes for the purpose of improving hurricane model forecasts. The CBLAST dataset has provided the first direct measurements of turbulent fluxes in the high wind regime up to hurricane force (Chapter 3), including the first detection of roll vortices by aircraft as well as SAR shown in this Chapter. We found that the lower stepped descent flight pattern is promising for studying the turbulent fluxes and the interpretation in terms of the hurricane boundary layer rolls. In the future, more flights with longer period of flux measurements within hurricane boundary layers are needed.

Chapter 5

Vertical Structure of Turbulence

5.1 Introduction

The planetary boundary layer (PBL) is the region of the atmosphere near the surface where the influence of the surface is felt through turbulent exchange of momentum, heat and moisture. The equations which describe the large-scale evolution of the atmosphere do not take into account the interaction with the surface. The turbulent motion responsible for this interaction is small-scale and totally sub-grid for current models and therefore needs to be parameterized. Hence, turbulence structure is crucial to the parameterization of the hurricane boundary layer.

The CBLAST experiment provided unique data sets that contain the measurements of the vertical structure of the turbulence throughout the hurricane boundary layer. In this Chapter, the vertical profiles of the mean quantities, spectra and cospectra, variances, and fluxes during the CBLAST stepped descent boundary layer measurements are investigated in order to address four questions: (1) To what extent is this boundary layer consistent with standard similarity theory? (2) Where is the top of the boundary layer? (3) What are the dominate scales of variability related with the turbulent

fluxes? and (4) How are the time and space scales in the turbulence eddies related to the net flux and overall turbulence state?

In this Chapter, the vertical structure of turbulence and flux in the boundary layer between the outer rainbands is presented in the following section. The characteristics of the spectra and cospectra of the wind velocity, potential temperature and humidity are demonstrated in section 3.

5.2 Vertical Structure of Turbulence and Flux

5.2.1 Scaling

Before the presentation of the vertical profiles, the data are non-dimensioalized according to the scaling parameters so that universal curves can be discussed. Following the methods discussed by Nicholls and Readings (1979), two scaling methods are essentially used to scale the turbulence structure in the literature: 'surface layer' similarity (Monin and Obukhov, 1954) and 'mixed layer' similarity (Kaimal et al., 1976). The former assumes that the parameters governing the turbulence structure are $u_*, t_*, q_*,$ and L, and parameters that are scaled by $u_*, t_*,$ and q_* should be functional of z/L only. However, mixed layer similarity is applied to where the turbulence structure is no longer influenced by surface momentum flux but does vary with the boundary layer depth, and the scaling parameters are w_* and z/z_i, where z_i is the boundary layer depth that is

usually defined as the lowest inversion base in the potential temperature profile, and w_* is the mixed layer scaling velocity defined as

$$w_* = [(H_0 / \rho c_p) z_i (g / \theta)]^{1/3}, \tag{5.1}$$

where H_0 is the surface sensible heat flux. Parameters scaled by w_* should then be functions of z / z_i only.

Fig.5.1 shows the schematic diagram developed by Nicholls and Readings (1979) indicating idealized limits of validity of certain scaling techniques for different boundary layer conditions. Firstly, there are two distinct layers where surface and mixed layer scaling schemes are applied independently. Surface layer scaling is valid only up to the height at which u_* is still an important parameter while mixed layer scaling can apply above that height. For instance, Kaimal et al. (1976) showed that Monin-Obukhov scaling applies only if $z < 0.1\ z_i$, while the mixed layer scaling is valid above in strongly convective conditions. Secondly, there is a layer of free convection (Wyngaard 1973; Panofsky 1978), where the turbulence is not sensitive to either z_i or L and both types of scaling apply. In the end, there is a region 'A' in Fig. 5.1, where neither mixed layer nor is surface layer scaling adequate, because in this type of boundary layer surface friction induced mechanical mixing cannot be neglected although z / z_i is quite large. This is generally the case over the ocean in which a general approach is to use $u_*, t_*, q_*,$ and z_i as the scaling parameters.

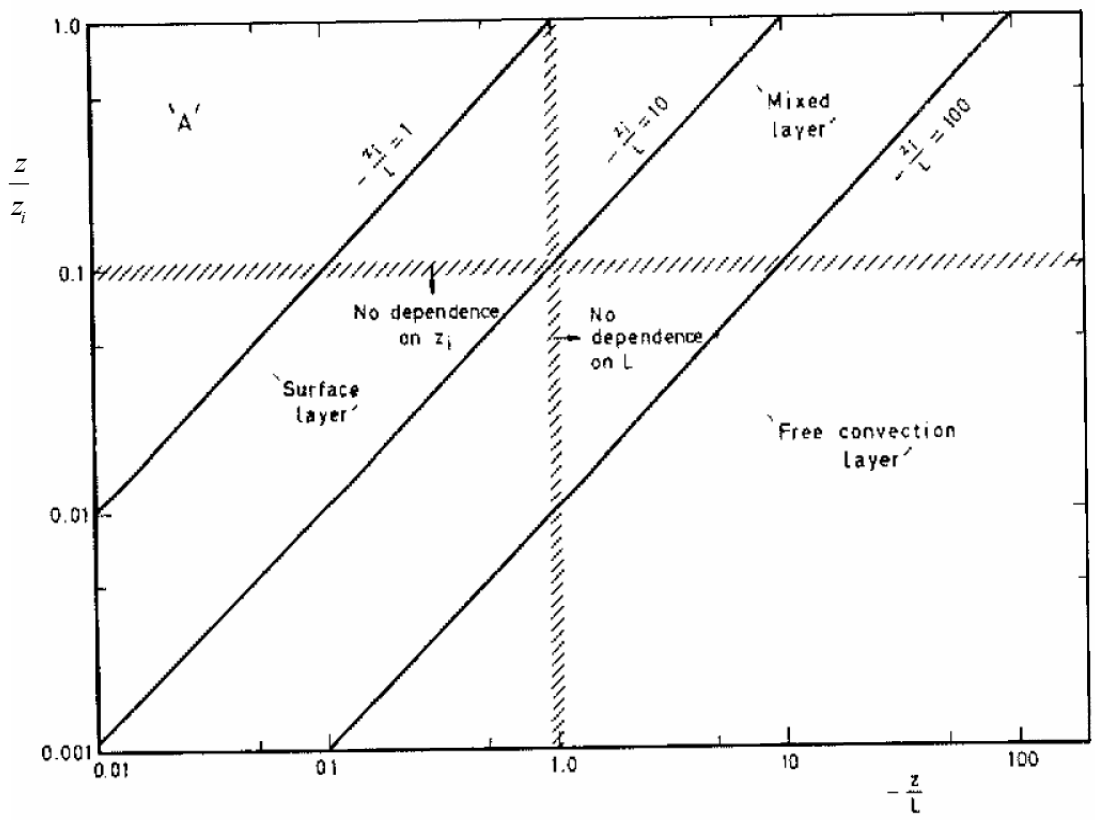

Fig. 5.1. Schematic diagram showing idealized limits of validity of certain scaling techniques. See Figure 2 in Nicholls and Readings (1979).

All the present data were collected in hurricane conditions over ocean with $-z_i/L < 1$, indicating the boundary layer is nearly neutral, where both the surface layer scaling and mixed layer scaling is important. So it is logical to use u_*, t_*, q_* and z/z_i to scale the present data. The scaling parameters were calculated using the surface values of the turbulent fluxes. The variance of the wind velocities, temperature and humidity are computed for each flux run. The Monion-Obukhov length is also calculated using an iteration method. The mixed layer depth was determined from the potential temperature profile. Note that to avoid the error induced by the extrapolation of the flight level flux

as to the surface, the surface layer scaling parameters t_* and q_* are not used when the vertical profiles of parameters related to potential temperature and humidity are shown.

5.2.2 Vertical Profiles of Turbulent Fluxes

The fluxes of momentum, heat, humidity and enthalpy have been calculated using the eddy correlation method and are presented in Chapter 3. However, emphasis was made on the determination of the surface fluxes. During the 2004 hurricane season, 2 flights were flown near and right above the surface layer. These provided data (as listed in Table 3.1) that could be used to extend our study of the structure to the whole boundary layer and above. There are a total of 23 flux runs taken at the height above the mixed layer with 19 of them conducted in 2004 and 4 in 2003. Data used here to describe the flux profiles are all taken in the similar wind regime with surface wind speed in the range of 20-30 m s^{-1}, and they are measured in the rain free region between the rainbands. Note that the 2002 data were not used here because they were measured in the lower wind speed regime.

Fig. 5.2 shows the profiles of the scaled momentum fluxes. The asterisks represent average values in the vertical bins of 150 m, and the bars show 95% confidence intervals. The blue line is from Nicholls and Reading (1979) and the red line is from Tjerstrom and Smedman (1993). The alongwind component of the vertical momentum flux shows a nearly linear profile, while the crosswind component is positive with a curvature that has the maximum value of around 0.5 u* at the height of the mixed layer

(z/zi=1). One interesting feature shown in Fig. 5.2 is that the momentum flux does not vanish at the top of the mixed layer height z_i.

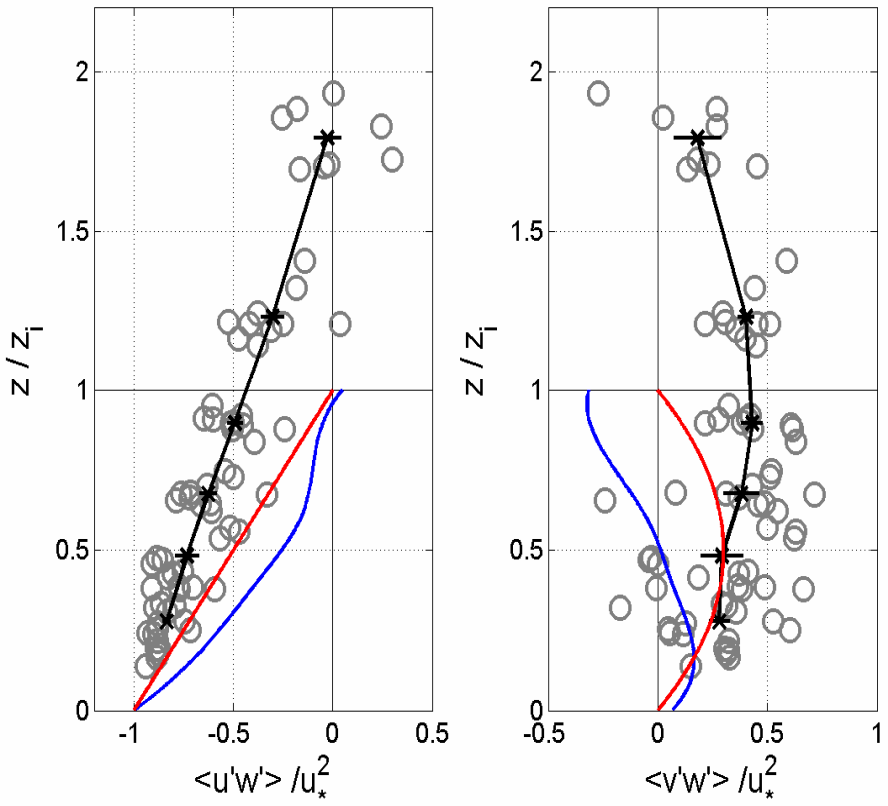

Fig. 5.2. Dimensionless profiles of the covariances of *uw* and *vw*. Black lines show the averages of the covariances. Blue line is from Nicholls and Reading (1979) and red line is from Tjernstrom and Smedman (1993). The covariances have been normalized by the square of the surface friction velocity (u_*) and the altitude is normalized by the mixed layer depth z_i.

Fig. 5.3 shows the normalized vertical profiles of the sensible heat and latent heat flux. Again, the black lines show the best fit by the vertically bin-averaged values. The averaged sensible heat flux profile shows a curvature with negative values mostly above z/zi=0.2. Extrapolation of this curve toward the surface tends to show a positive sensible heat flux near the surface. The latent heat flux decreases with the increasing height above

the mixed layer. Below the boundary layer, the latent heat flux is nearly constant with height as discussed in Chapter 3. Both of the sensible and latent heat flux vanish at z/zi=1.9, same as the behavior of the momentum flux profile. This is different from the flux measurements by Moss (1978) who found that the momentum flux vanishes at the top of the mixed layer. Unfortunately, there was no sensible heat or latent heat flux measurements conducted by Moss. If we define the boundary layer depth as the height where the momentum flux is zero, then the boundary layer height should be around twice of the mixed layer depth. This indicates that other physical mechanisms, such as entrainment, must exist to account for the non-zero momentum flux near the top of the mixed boundary layer.

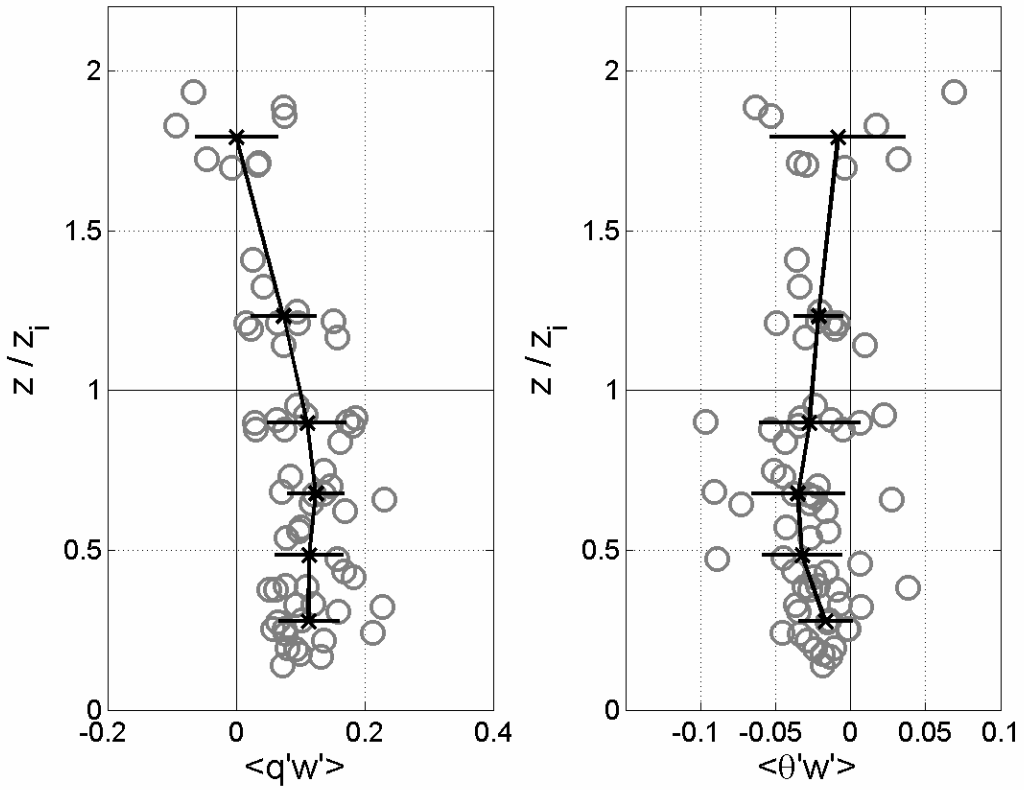

Fig. 5.3. Normalized profiles of the covariances of qw and θw. Black lines show the averages of the covariances. z_i is the mixed layer depth.

5.2.3 Vertical Profiles of Variances

Studies of variances in the atmospheric boundary layer are important because they provide the direct test of similarity predictions and indirect estimates of vertical fluxes. In addition, these turbulent properties are very important parameters for the study the atmospheric dispersion which is dependent on the intensity of turbulence, stability and boundary layer height. The standard deviations and variances are related with each other in the form, $\overline{s'^2} = \sigma_s^2$, where s is any one of u, v, w, θ and q. The nondimensional variances or standard deviation normalized by the surface layer scaling parameters ($u_*, \theta_*,$ and q_*) are universal functions of z/L if Monin-Obukhov scaling is correct (Stull 1988). In neutral conditions when z/L=0, the normalized variances should be constants, independent of height or surface roughness.

The standard deviations of temperature, absolute humidity, horizontal and vertical velocities are calculated for all the flux runs. Fig. 5.4 shows the distribution of the standard deviations of wind velocity with height normalized by the mixed layer depth z_i. Previous turbulence measurements by Nicholls and Reading (1979) and Tjernstrom and Smedman (1993) are also shown. The horizontal velocity variances scaled by the surface friction velocity and the mixed layer depth show a slight maximum near the surface. The standard deviation of the alongwind component velocity shows a slightly decrease with the increasing height, while that of the crosswind component stays relatively invariant with the height. The vertical velocity variance exhibits nearly constant behavior with height within the mixed layer but decreases with height above that.

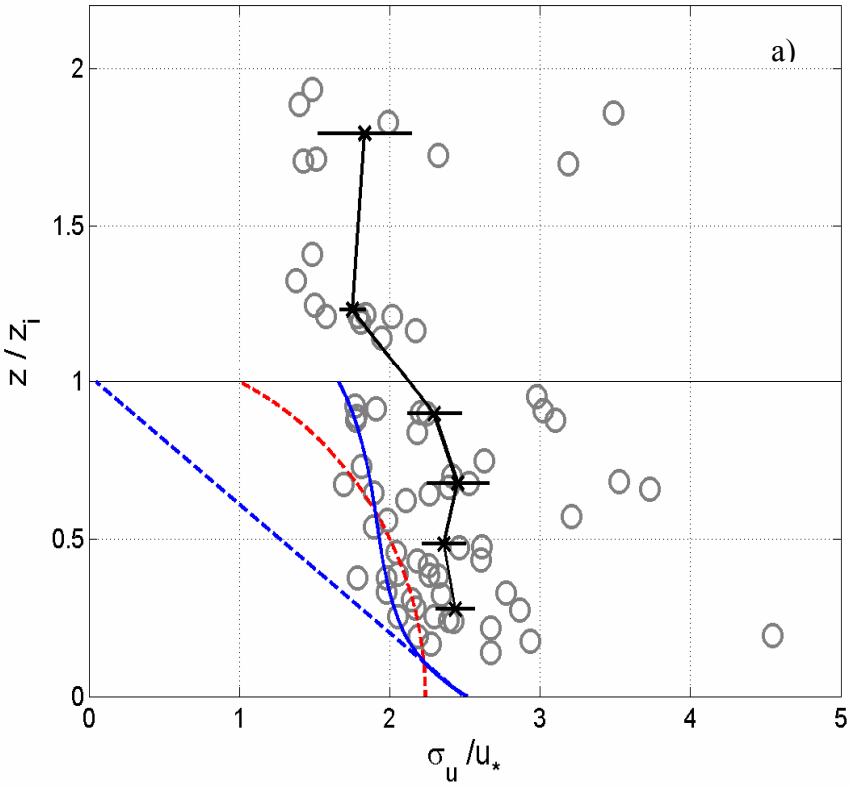
a)
z / z_i
σ_u /u_*
0
0.5
1
1.5
2
0
1
2
3
4
5

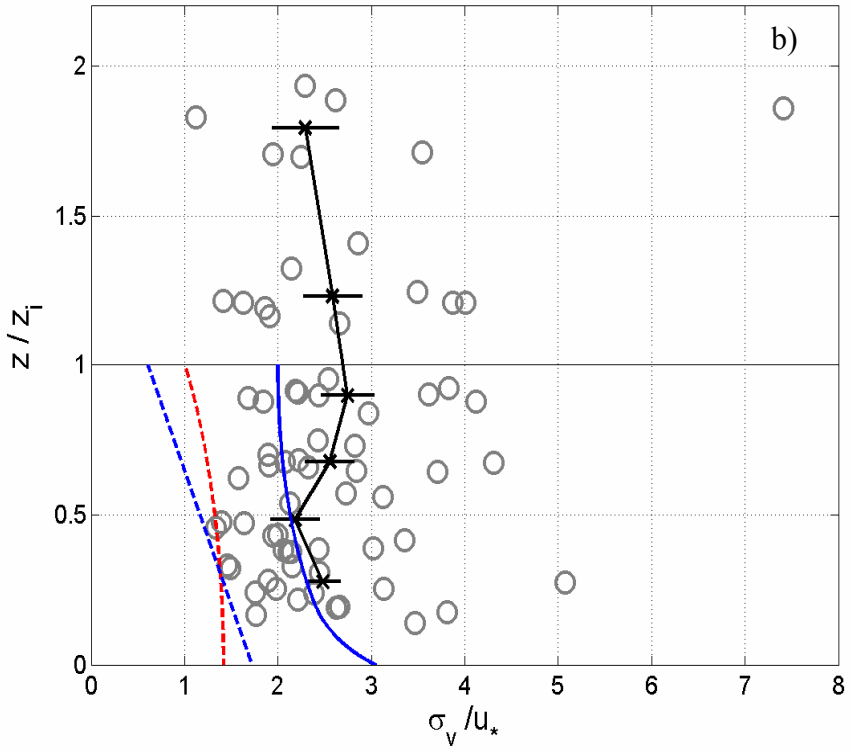
b)
z / z_i
σ_v /u_*
0
0.5
1
1.5
2
0
1
2
3
4
5
6
7
8

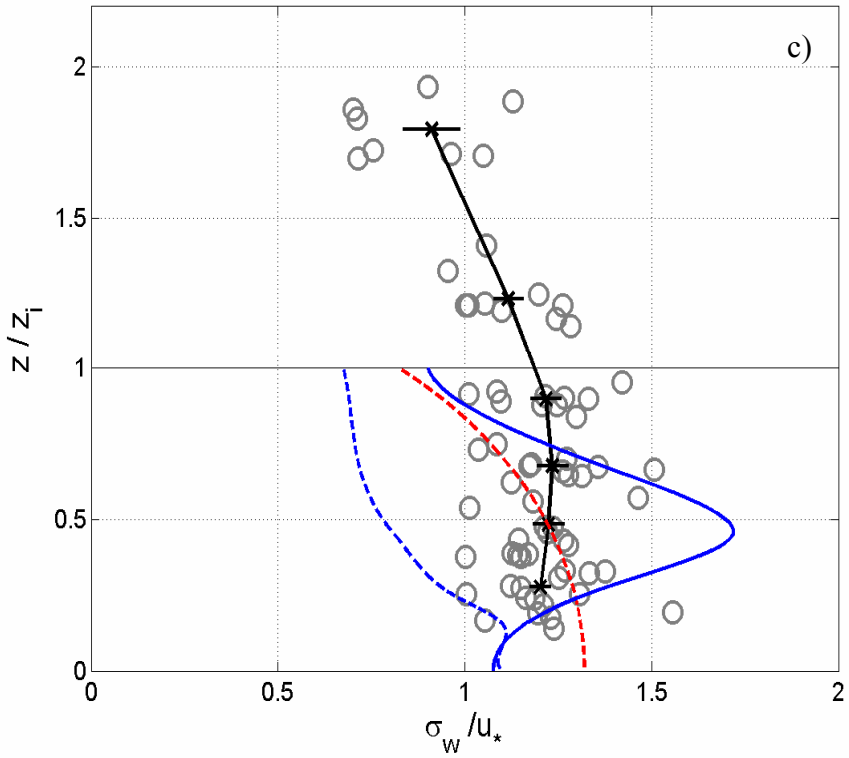

Fig. 5.4. Dimensionless profiles of velocity variances of the three wind components (u, v and w in panels a, b and c, respectively). The black curves show the averages of the variances. The blue lines are from Nicholls and Reading (1979) for data taken over the ocean at moderate wind speeds. The solid blue line represents data in nearly neutral conditions, while the dashed blue line represents data in slightly convective conditions. The red line is from Tjerstrom and Smedman (1993) for data in nearly neutral conditions near taken in the coastal ocean. The variaces are normalized by the frictional velocity (u_*) and the altitude is normalized by the mixed layer depth (z_i).

The surface layer form for $\sigma_{u,v}^2 / u_*^2$, proposed by Panofsky et al. (1977) in the unstable limit from its value of 4 at neutral is as following:

$$\frac{\sigma_{u,v}^2}{u_*^2} = 4 + 0.6\,(\frac{z_i}{|L|})^{2/3} \qquad (5.2).$$

In this study, the extrapolated surface layer values of the scaled variances for the CBALST data are as follows:

$$\frac{\sigma_u^2}{u_*^2} = 6.25\,,\ \ \frac{\sigma_v^2}{u_*^2} = 6.7\,,\ \ \frac{\sigma_w^2}{u_*^2} = 1.5 \qquad (5.3).$$

The values of $\sigma_{u,v}^2 / u_*^2$ are significantly higher that those calculated from (1).

The surface layer form for σ_w / u_*, essentially derived from the Kansas data (Businger et al., 1971), then reexamined and refined through comparisons with other observations by Hogstrom (1988), is given by:

$$\frac{\sigma_w}{u_*} = \begin{cases} 1.25(1+3|z/L|)^{1/3}, -2 \le z/L \le 0 \\ 1.25(1+0.2z/L),\ \ 0 \le z/L \le 1 \end{cases} \qquad (5.4).$$

The σ_w / u_* value derived from the CBLAST data is consistent with the above Monin-Obukhov scaling functions, indicating that the surface layer could be parameterized using the Monin-Obukhov similarity theory up to hurricane force for the boundary layer in the rain free region between the rainbands.

The vertical profiles of the standard deviation of potential temperature and specific humidity are shown in Fig. 5.5. The scatter is substantial larger here than the variance plots for wind velocity. Both the variances of the potential temperature and specific humidity increase with the increasing height. However, the variance of humidity shows smaller variation with height which is consistent with the humidity flux profiles. The large increase of the variance of potential temperature above the mixed layer suggests that entrainment processes may occur there transporting dry air from the stable layer above.

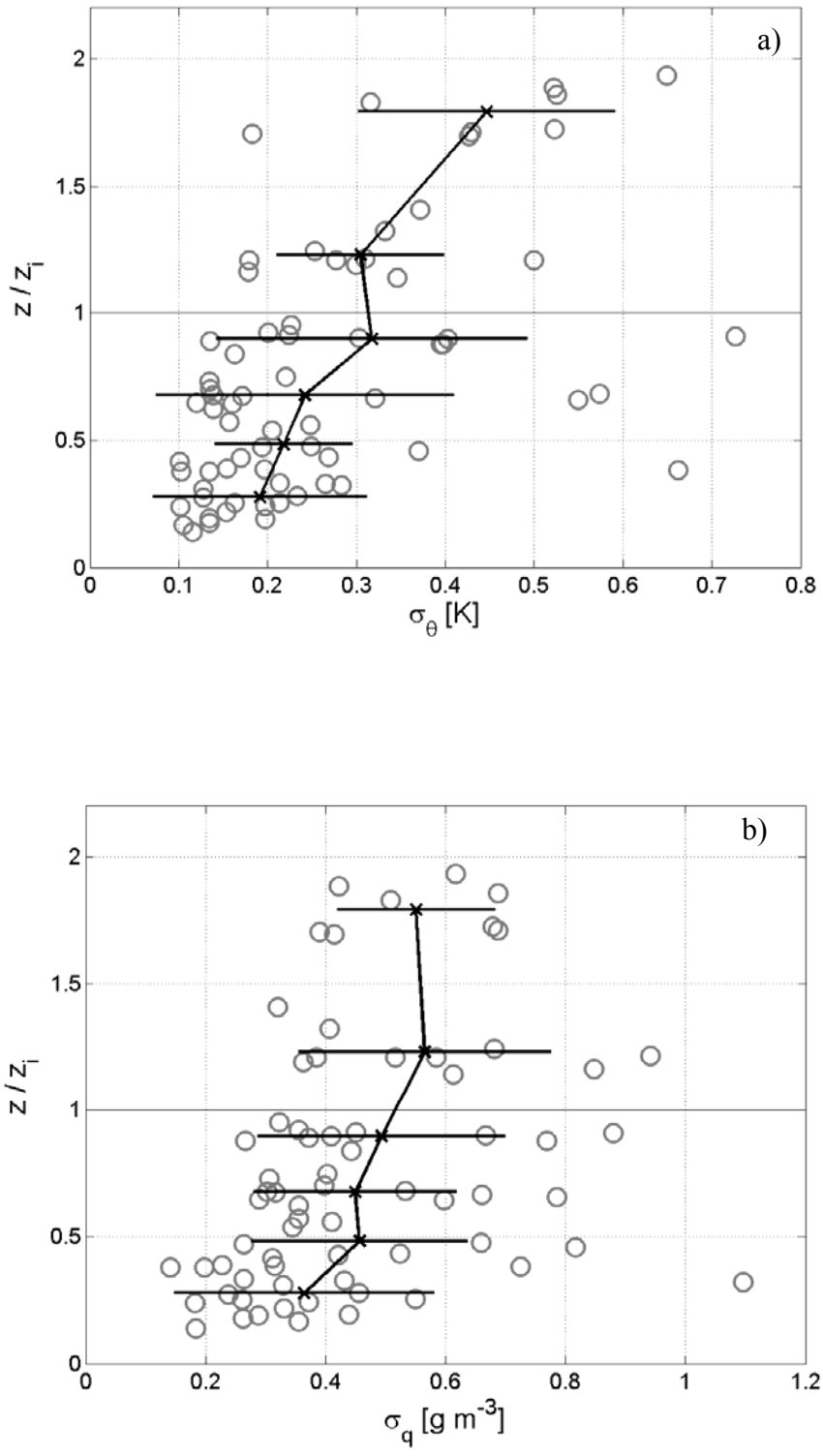

Fig. 5.5. Vertical profiles of variances of temperature (a) and humidity (b) normalized by the mixed layer height. The black curves show the averages of the variances.

5.3 Characteristics of Spectra and Cospectra

Turbulent flows like those in the atmospheric boundary layer can be thought of as a superposition of coherent eddy patterns of velocity, vorticity, and pressure spread over a wide range of sizes (Kaimal and Finnigan, 1994). These eddies interact constantly with the mean flow exchanging energy with each other. Most of the kinetic energy is contained by the large eddies that are subject to instabilities. In order to understand the conversion of mean kinetic energy into turbulent kinetic energy in the large eddies, the eddy cascade processes, and its final conversion to heat by viscosity, different scales of turbulent motion must be isolated. This could be completed using the Fourier spectra and cospectra of the turbulence that are associated with scales of motion in kinetic energy, variance and eddy flux and represent the boundary layer structure. This section discusses the characteristics and variability of the spectra and cospectra of wind velocity and the scalar parameters.

5.3.1 Spectra and Cospectra

Fig. 5.6 shows the spectral behavior of the vertical and horizontal along-wind velocities. The spectra estimates are normalized by the square of the friction velocity. Data from the second stepped descent measurements on 14 September 2003 are shown here. Evidently the frequency at the spectra peak increases with height, suggesting that the data are scaled well by the surface layer scheme. Given the aircraft speed is around

110 m s^{-1}, the equivalent peak wavelengths in the alongwind and vertical wind velocity spectra increase from 300 m to around 1 km as the attitude increases from 70 m to 400 m.

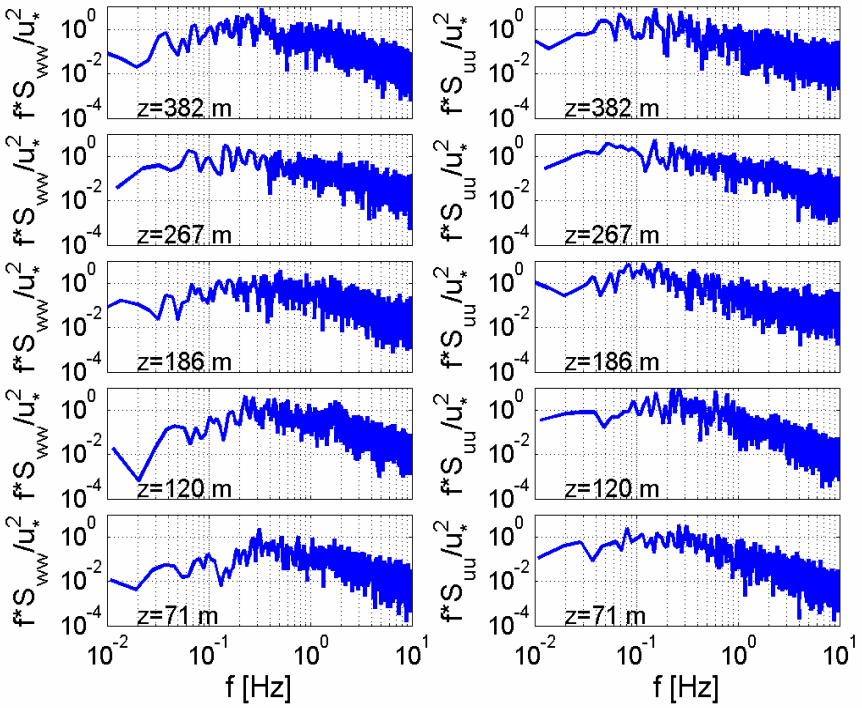

Fig. 5.6. Vertical variation of the spectra of the vertical velocity (left) and along-wind horizontal wind velocity (right). Data are from the second stepped descent flux runs after 18:50 UTC on 14 September 2003.

The along-wind component velocity spectra display a -2/3 slope at high frequency. This slope occurs at frequencies corresponding to scale sizes which are three to four times larger than the distance from the surface, indicating that the -2/3 slope of the along-wind velocity component spectra is not sufficient evidence for the existence of an inertial subrange which depends on the flow being locally isotropic. But at sufficiently high frequency where the spectra of both vertical and horizontal velocity components display a -2/3 slope and where the momentum transfer is negligible, isotropy may exist.

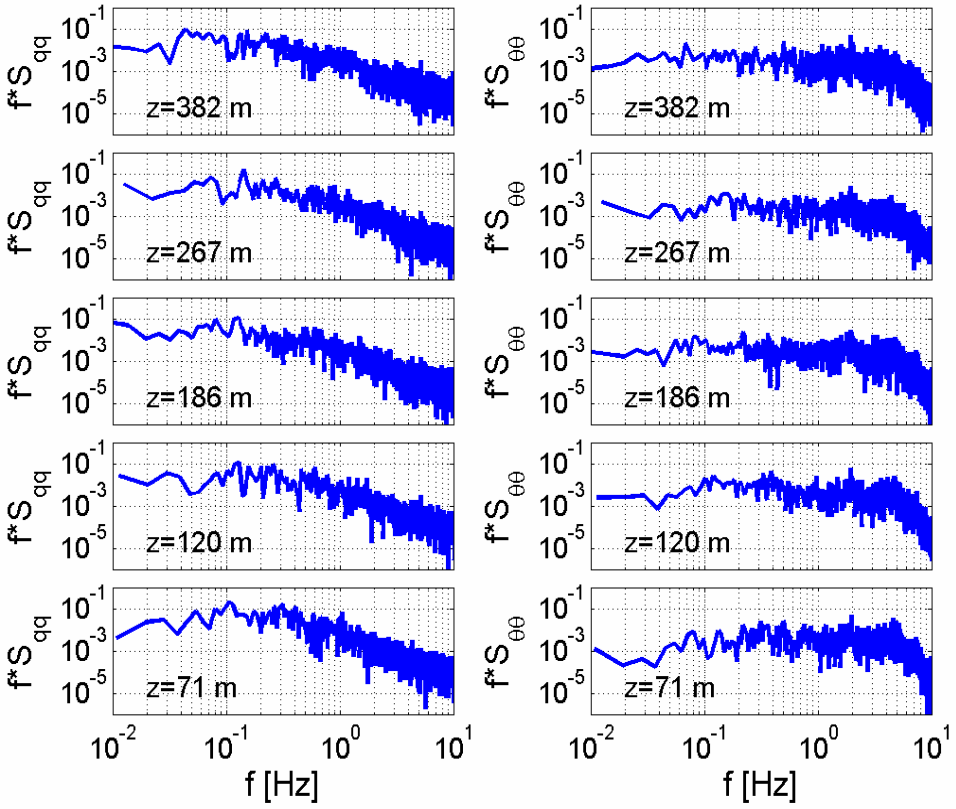

Fig. 5.7. Vertical variation of the spectra of the specific humidity (left) and potential temperature (right). Data are from the second stepped descent flux runs after 18:50 UTC on 14 September 2003.

Fig. 5.7 shows the spectral behavior of humidity and potential temperature. The data are from the same flight as those used in Fig. 5.6. For the humidity spectra, it shows similar shapes compared to the spectra of the along-wind component wind velocity. The peak wavelength of the humidity spectra also increases with the measurement height, indicating the scales of the turbulent eddies transporting humidity increase as the distance from the surface increases. However, the potential temperature spectra demonstrate dissimilarity with the humidity flux, showing a broad band of the energy containing range

with nearly no inertial subrange. This makes it difficult to identify the peak wavelength of the potential temperature spectra.

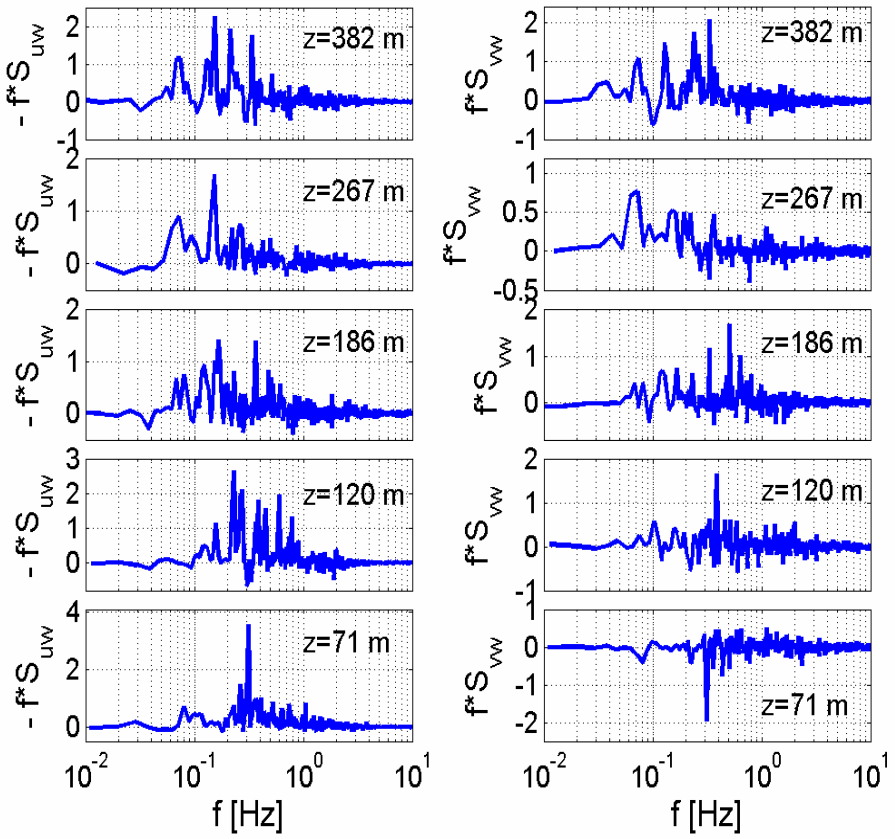

Fig. 5.8. Vertical variation of the cospectra of the along wind (left) and cross wind (right) momentum fluxes. Data are from the second stepped descent after 18:50 UTC on 14 September 2003.

Fig. 5.8 represents the height dependence of the cospectra of *uw* and *vw* that are equivalent to the momentum flux cospectra. Note that in the analysis trends are removed from both velocity components. It is shown that most of the energy for the cospectra of momentum flux is well contained in the frequency range of 0.1- 1 Hz that corresponds to wavelengths about 300 m - 1000 m. Similar to the spectra plots, the peak wavelength

increases with height. The sign of the along wind component momentum flux always is negative, indicating momentum is transported downward toward the sea surface. The sign change in the cross wind component cospectra may be due to the rotation scheme itself, but shows the variation of the transport direction of the cross wind momentum flux within the stronger rotation flow of a hurricane.

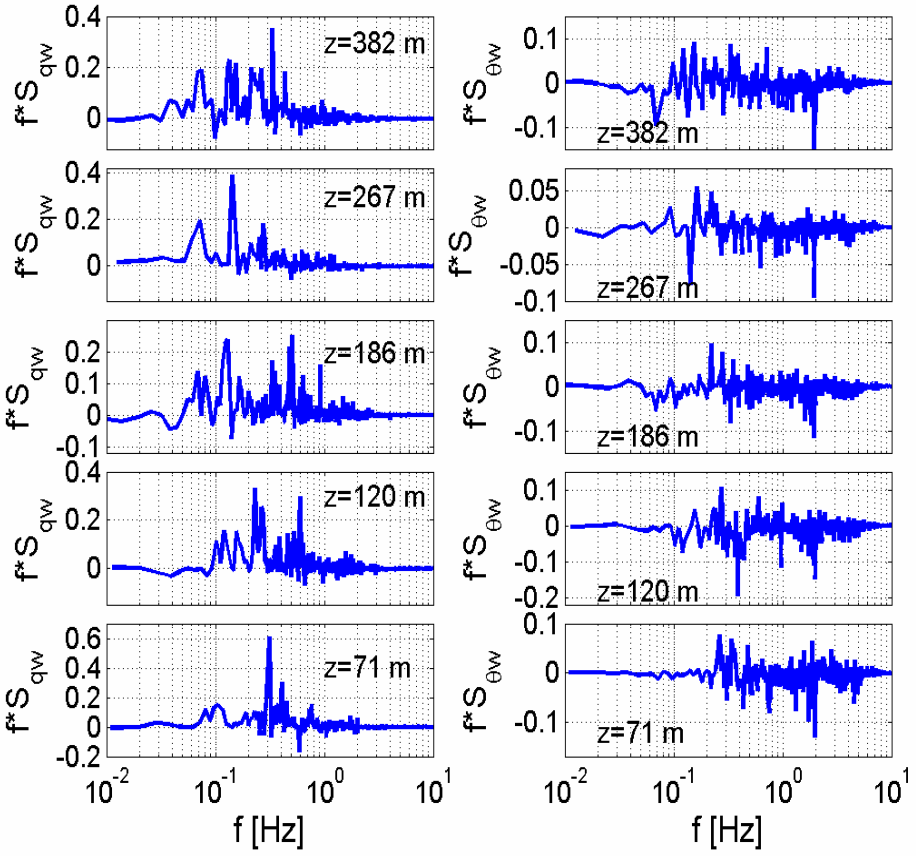

Fig. 5.9. Vertical variation of the cospectra of the humidity flux (left) and sensible heat flux (right). Data are from the second stepped descent after 18:50 UTC on 14 September 2003.

Fig. 5.9 shows the vertical variation of the cospectra of the humidity and sensible heat flux. Again, the humidity cospectra shows similarity with the along wind component velocity cospectra in shape, however, the potential temperature cospectra shows a different characteristic. The sign of the humidity flux is always positive, showing the moisture is transported upward. Most of the energy in the potential temperature flux is from the low frequency range. The overall heat flux is mostly negative.

5.3.2 Universal Shape Spectra and Cospectra

A consequence of Monin-Obukhov similarity theory is that, in some frequency or wavenumber range, the spectra of wind velocity, temperature and humidity are expected to follow some universal shape when scaled in the appropriate manner (Busch, 1973). Considerable efforts have been made in determining the universal forms in previous experimental studies. Kaimal et al. (1972), using data profiles from the 1968 Kansa experiment over land, normalized the velocity spectra by spectral density energy in the inertial subrange and by surface fluxes. Their results present the classic universal shapes of the wind velocity, temperature and humidity spectra as a function of the dimensionless frequency, fz/U, and stability index, z/L. The spectra of Miyake et al. (1970) based on near-neutral data over the coastal sea demonstrate similar universality of the spectral shape over the ocean. Other marine data sets, e.g., Nicholls and Readings, Smith and Anderson (1984), support the Miyake curves.

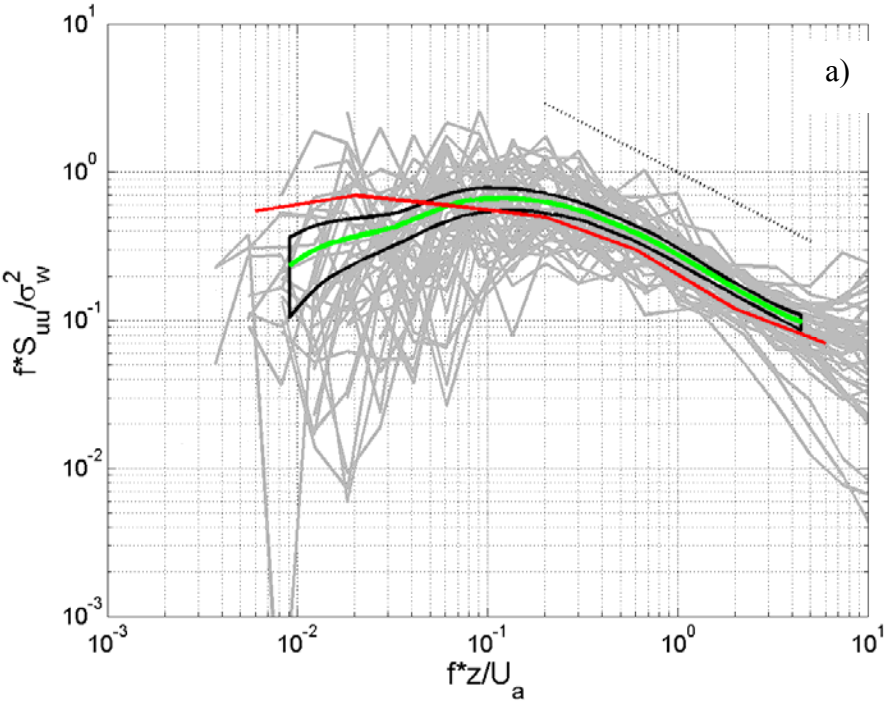
a)
f^*S_{uu}/σ_w^2
f^*z/U_a
10^{-3}
10^{-2}
10^{-1}
10^{0}
10^{1}

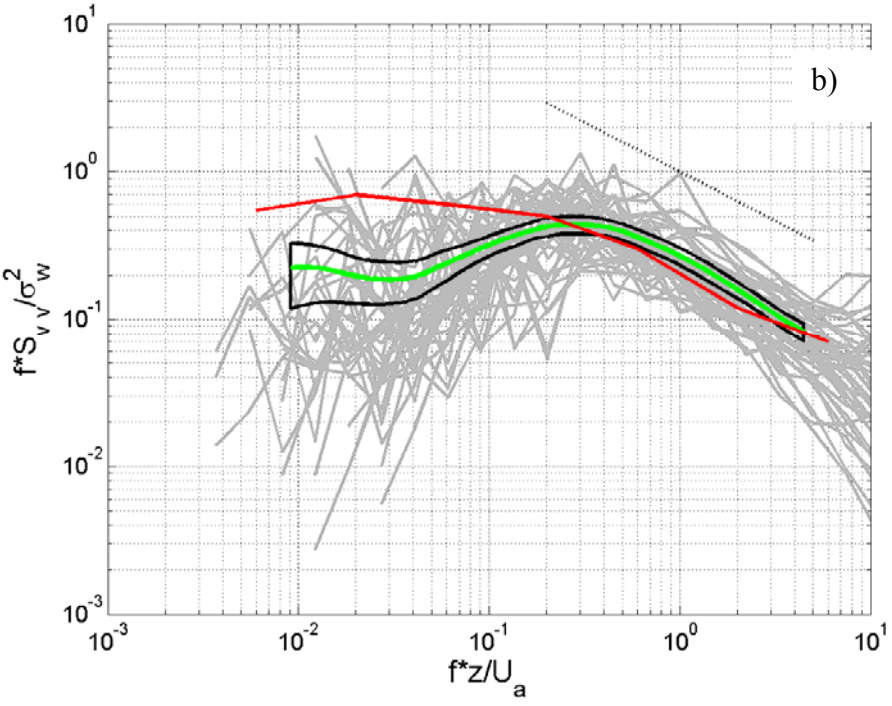
b)
f^*S_{vv}/σ_w^2
f^*z/U_a
10^{-3}
10^{-2}
10^{-1}
10^{0}
10^{1}

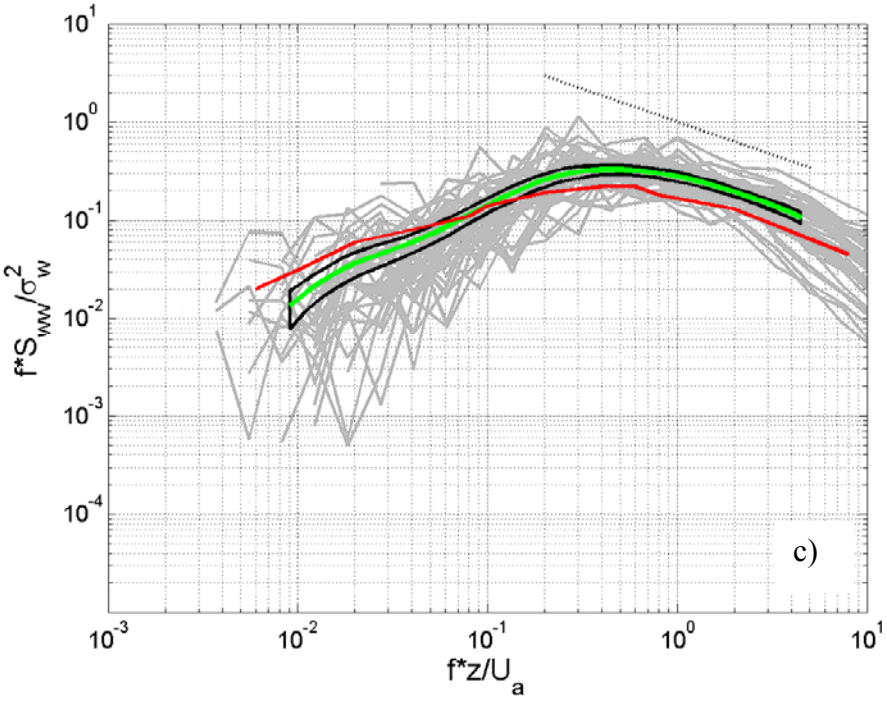

Fig. 5.10. Curves of universal spectra in the scaling of Miyake et al. (1970). The three panels show spectra of the alongwind component (a), crosswind component (b), and vertical velocity. The grey lines are the spectra plots for the 43 flux runs during the stepped descent measurements in Hurricanes Fabian and Isabel. Areas enclosed by the black lines denote 1 standard error from the mean green curve. Also shown are the Miyake et al. (1970) curves (red) and lines showing the inertial subrange slope (dotted). U_a is the true air speed; f the frequency [Hz]; z the aircraft altitude; and σ_w the standard deviation of vertical velocity.

In Fig. 5.10, the universal S_{uu}, S_{vv}, and S_{ww} spectra using the scaling of Miyake et al. (1970) are shown. The curves of Miyake et al., derived from visual fits to their plots, are also shown (red). The dashed line drawn on each plot has a slope of -2/3 that corresponds to the Kolmogoroff -5/3 law. Firstly, the scaled spectra curves in this study (using the CBLAST 2003 data) fall into a universal shape. This confirms the conclusion made in the previous section that discussed the vertical structure of the velocity variance, that the boundary layer between the rain bands in major hurricanes is consistent with the

Monin-Obukhov similarity theory even if the wind there is higher up to 30 m s^{-1}. Secondly, the Miyake et al. curves fall outside one standard error of the CBLAST universal curves. Although they are generally similar in shape to the CBLAST universal curves, they are shifted to the larger frequency band. This indicates that the characteristics of the turbulent transport of momentum in the high wind hurricane boundary layer are somewhat different in scale, smaller to those in the lower wind speed regime outside hurricanes.

As with the data used by Miyake et al. (1970), the response of the turbulent gust probes used here is limited for the dimensionless frequencies higher than 10, hence the data for fz/U>10 are not shown. Other than that, Fig.5.10 shows the consistency of the wind velocity measurements throughout the whole experiment. This also demonstrates the convincing ability of the Rosemount turbulent gust probe and the BAT probe to measure the three-dimensional wind velocity in hurricane conditions.

Fig. 5.11 shows the universal spectra of the specific humidity. The Miyake et al. curves are also shown. Below the peak frequency fz/U=0.4, the Miyake curves fall within one standard error of the CBLAST universal curves. Above that, the humidity spectra seem to be steeper than that slope. This may be due to the loss of response inherent in the humidity signal at high frequency since the air passes a nearly 1 m tube before it reaches the LICOR hygrometer. Note that the scatter of the potential temperature spectra (not shown) is much larger than that of the humidity spectra, indicating the difficulty in measuring temperature in hurricane conditions since the temperature sensors are more easily affected by rain droplets.

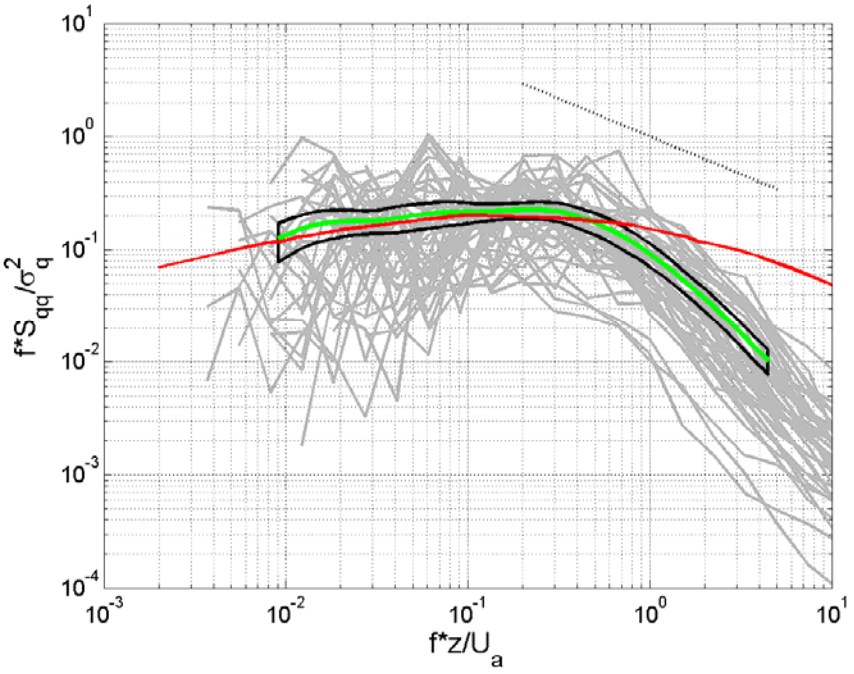

Fig. 5.11. Curves of universal spectra of the specific humidity. Curves are as in Fig. 5.10.

The cospectrum is inherently more difficult to measure than the power spectrum because the correlations between the variables are sometimes very small. The cospectra are also very sensitive to instrumental errors such as caused by the time lag between them. Fig. 5.12 shows the behavior of the cospectra of uw and vw. These are essentially the cospectra of the along wind and cross wind component momentum fluxes, respectively. For the uw cospectra, the Miyake curves fall within one standard error of the CBLAST universal curve. However, the peak frequency of the CBLAST universal curve is at fz/U=0.3, which is higher than that of the Miyake curves.

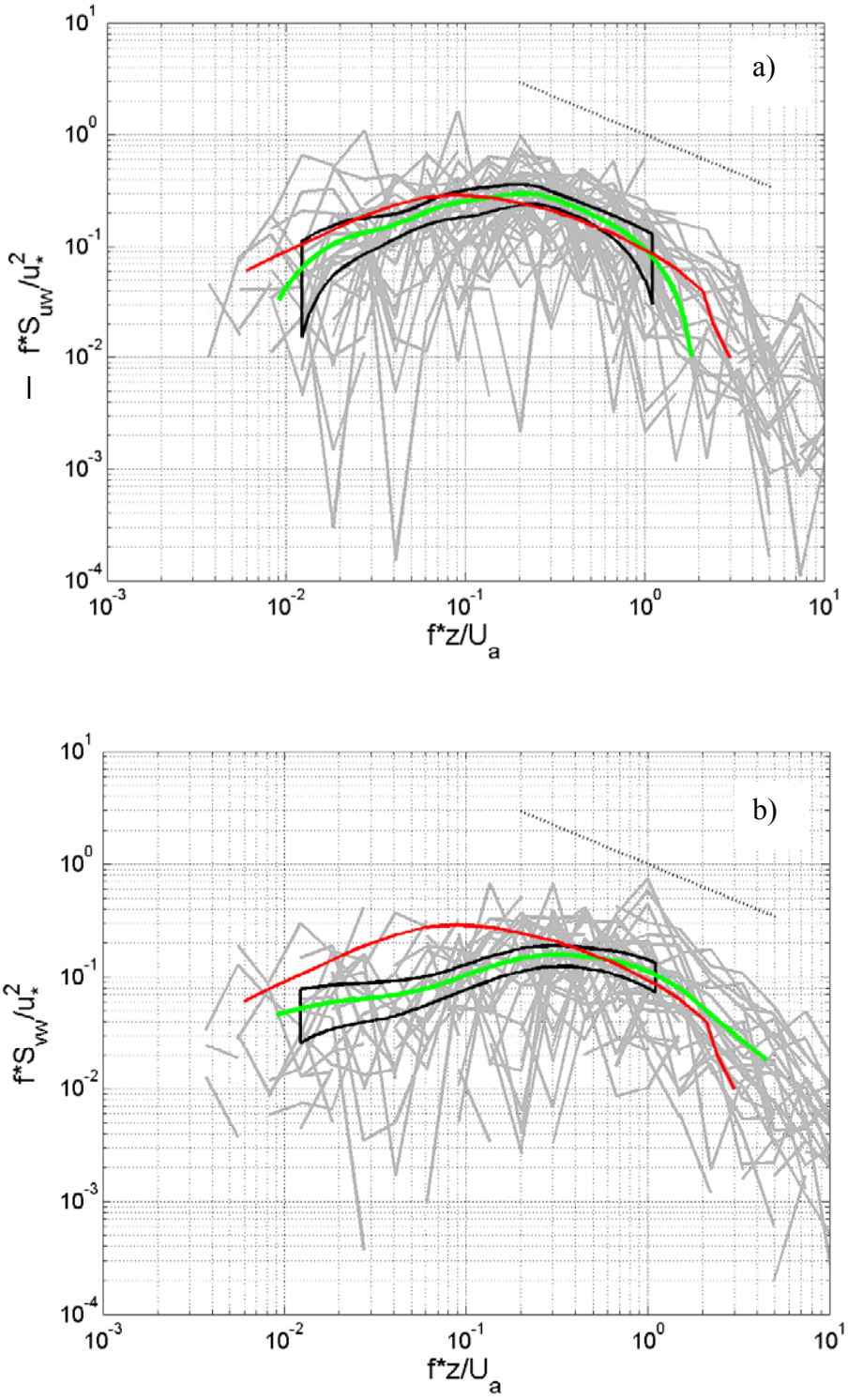

Fig. 5.12. Curves of universal cospectra of the alongwind component (a) and crosswind component (b) momentum flux. Curves are as in Fig. 5.10.

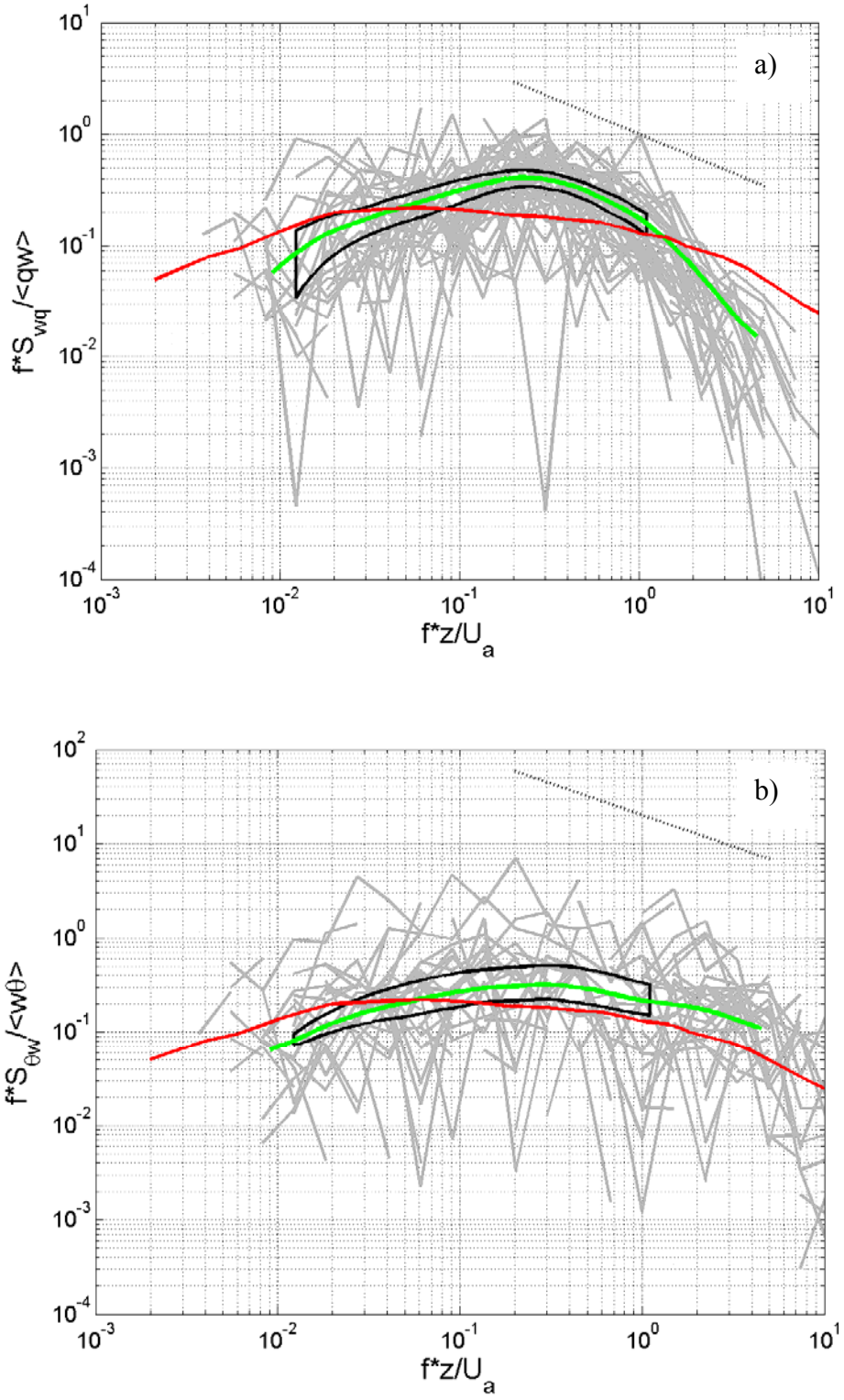

Fig. 5.13. Curves of universal cospectra of the humidity (a) and sensible heat (b) flux. Curves are as in Fig. 5.10.

Fig.5.13 shows the universal cospectra of qw and θw which describe humidity and sensible heat transport. The cospectra of the humidity flux are quite similar to the cospectra of uw, although there is a slight departure from the Miyake curves. The cospectra of the sensible heat flux agree well with the Miyake curves. However, it should be noted that in the logarithmic plots, the negative values of the sensible heat flux are not shown.

Above all, the CBLAST data gathered within rain free region between the outer rainbands in major hurricanes can be grouped into universal spectra and cospectra, with peaks at somewhat higher frequencies than the Miyake et al. curves. The high frequency spectra and cospectra behavior is consistent with local isotropy. In the inertial subrange, the spectra fall at the -5/3 slope, but the cospectra fall off faster. The CBLAST data are mostly taken under near neutral conditions with slightly variation of stability. Thus it is difficult to separate the spectra and copsectra according to z/L as done by Kaimal et al. (1972). In the studies of Kaimal et al., they used the surface flux and surface layer dissipation rate as the scaling parameters, however, the CBLAST measurements were mostly conducted above the surface layer such that the surface fluxes are extrapolated from the flight level data. The use of the Kaimal et al. scaling to the CBLAST data introduces much larger fluctuations in the universal spectra and cospectra plots. On the other hand, the Miyake et al. scaling works well for the CBLAST data. Conclusion can made from Figs. 5.10-13 that the measurements throughout the CBLAST experiment are consistent.

Chapter 6

TKE Budget

6.1 Introduction

The turbulent kinetic energy budget of horizontally homogeneous turbulence with a mean wind shear in the vertical and modified for the effect of moist convection can be given by

$$\frac{De}{Dt} = -\overline{u'w'}\frac{\partial \bar{u}}{\partial Z} - \overline{v'w'}\frac{\partial \bar{v}}{\partial Z} + (g/\bar{\Theta})\overline{w'\theta'} + 0.61g\overline{w'q'} - \frac{\partial \overline{w'e}}{\partial Z} - \frac{1}{\rho}\frac{\partial \overline{w'p'}}{\partial Z} - \varepsilon, \qquad (6.1)$$

where e is the turbulent kinetic energy (TKE) and is defined as $e = \frac{1}{2}(u'^2 + v'^2 + w'^2)^{1/2}$, ε is the dissipation rate of turbulent kinetic energy, the overbar represents the mean over a certain period of time, and Z is the altitude. The left hand side of equation 1 is the local rate of change of TKE, the right hand side first and second terms together are the shear production, the third term and fourth terms together are the buoyancy production, the fifth term is the transportation of TKE, the sixth term is the pressure transport, and the last term is the dissipation. An examination of the terms in the turbulent kinetic energy equation could help our understanding of the nature of turbulent production and destruction in the boundary layer.

The measurements made during CBLAST provide estimates of most terms in the kinetic energy budget. Some of the terms are measured directly, while others are inferred from the data based on previously obtained relations. The terms that are generally believed to be small are ignored. For example, the pressure transport term could not be accurately measured but is inferred indirectly as a residual after measurements of all other terms.

The dissipation term is estimated from the spectral density of the longitudinal velocity component at high wave numbers, when the spectral velocity components exhibit a -5/3 power law in their spectra. The dissipation of TKE is given by

$$\varepsilon = \alpha_u^{-3/2} \frac{2\pi f}{U} [f S_{uu}(f)]^{3/2}, \tag{6.2}$$

where α_u is the Kolmogoroff one dimensional wave number constant, f is frequency, U is the relative air speed, S_{uu} is the spectral of the horizontal along wind speed. In the past the published values of α_u were around 0.48 (Pond et al., 1963). In this study, we use α_u =0.5 following Drennan et al. (2005).

Since the mean wind gradient cannot be accurately determined from the aircraft wind measurements, the first two terms on the right hand side of equation 1 are not directly accessible. The second of these is neglected on the grounds that at low levels where there may be an appreciable wind gradient $\overline{v'w'}$ is negligible. The first shear production term is estimated by $u_*^3 / \kappa z$, a relation which, strictly speaking, is only valid under neutral conditions.

The buoyancy production consists of two parts; one is due to the sensible heat and the other due to the moisture flux. Both of these are directly measured as discussed in the

above sections. The pressure transport term has been measured over water and found to be about 10% of the shear production term at levels between 1 m and 4 m (Donelan, 1990). The TKE transport and pressure transport terms have about the same magnitudes and opposite signs (Donelan 1990). At the levels being considered here it is probable that these terms are more important either jointly or singly. In this study the TKE transport term is directly measured. However, as the aircraft measurements cannot provide any direct estimates of the pressure transport term it is convenient to treat it together with any other terms (i.e. advection terms) as a combined residual term D.

As the flux runs in this study were qualitatively chosen with the criteria of stationarity, the turbulent field in each run is assumed to be locally horizontally homogeneous. Hence the local rate of change of energy may be neglected. Generally under these conditions it is two orders of magnitude less than the production and dissipation terms. For the purpose of accuracy, we put this term in the residual term D.

In this Chapter the turbulent kinetic energy budget is investigated in two ways: 1) The height dependence of each term in the TKE budget equation for all the 2003 and 2004 flights analyzed; 2) The TKE budget for the rain free region between the rainbands. They are shown in section 2 and 3, respectively. The TKE budget for the hurricane boundary layer between the rainbands is also compared with that from the previous measurements in the atmospheric boundary layer elsewhere.

6.2 Height Dependence of Terms in TKE Budget

6.2.1 Mechanical production

Fig. 6.1 shows that the shear production decreases rapidly with increasing altitude. This indicates that the measured stress decreases with height and the wind gradient that is inferred from the ratio of friction velocity to altitude also rapidly decreases with height. Evidently the importance of mechanical production is restricted to the first 200 meters only.

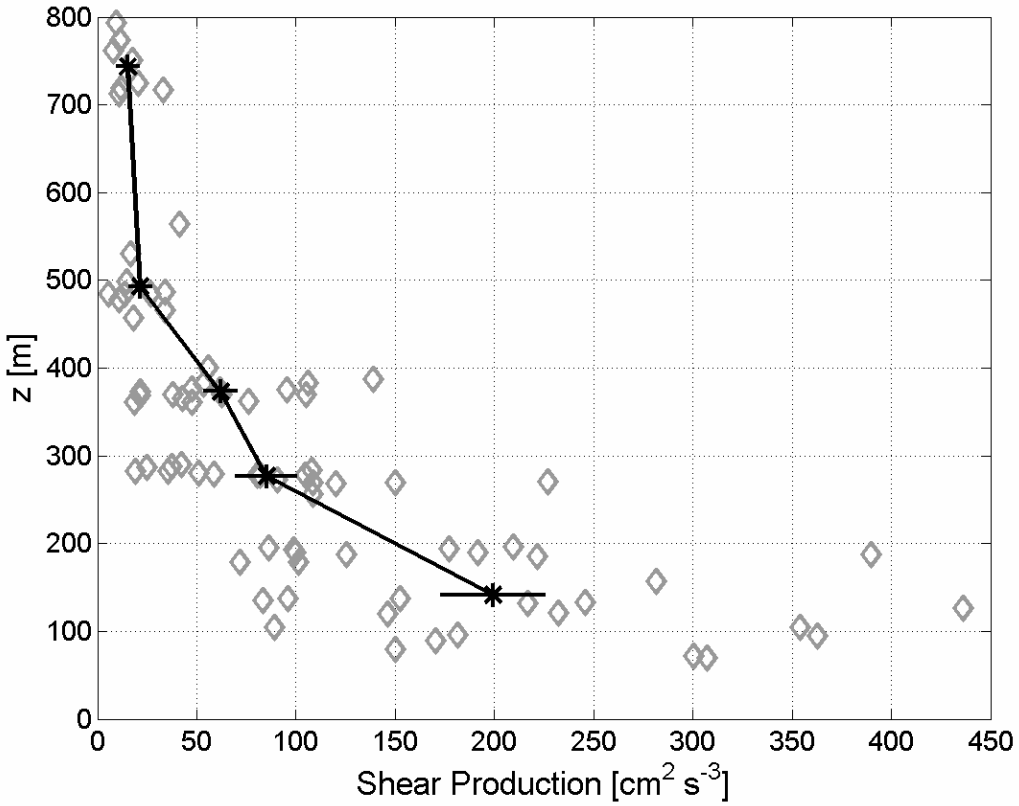

Fig. 6.1. Vertical profiles of the shear production. Black lines show the averages of the shear production and one standard error.

6.2.2 Buoyancy Production

Fig. 6.2 shows the buoyancy production terms for all the flights. At the lowest level, the buoyancy term is generally an order of magnitude smaller than the shear production term, but while the latter decreases rapidly with height the buoyancy production term changes little. At intermediate and higher levels the overall enthalpy flux may be negative, but in these cases the buoyancy production due to the moisture flux is larger than the negative contribution due to the sensible heat flux. Thus the total buoyancy production in the mean was positive between 100 m and 400 m during this experiment.

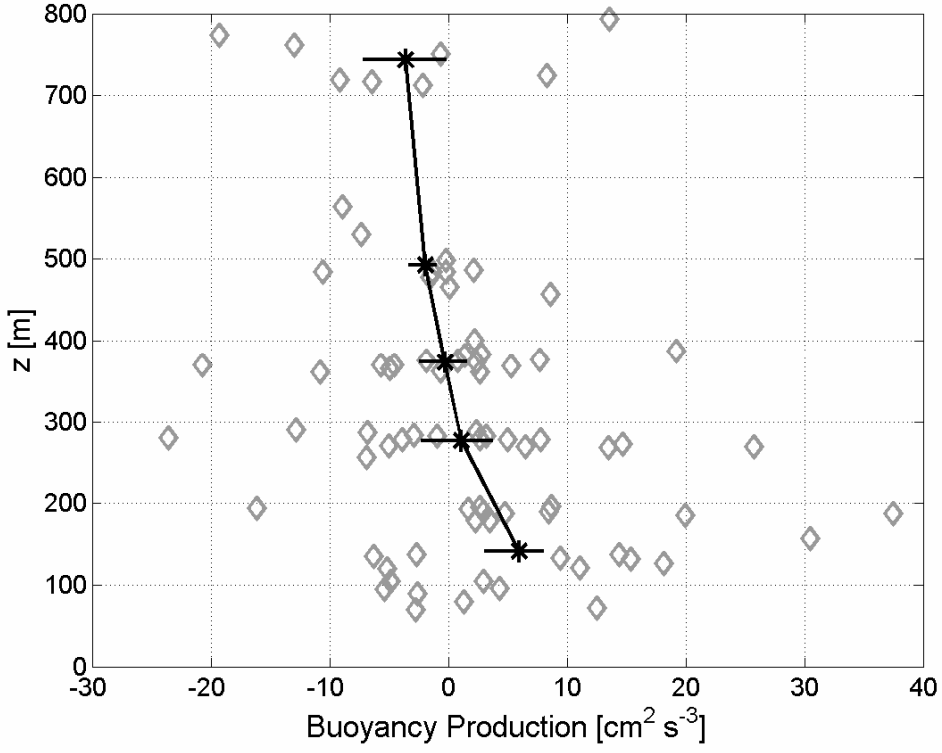

Fig. 6.2. Vertical profiles of the buoyancy production. Black lines show the averages of the buoyancy production and one standard error.

6.2.3 Dissipation

Fig. 6.3 shows the variation of the rate of dissipation with height. Apparently the rate of decrease of ε is much more rapid at low levels than at the higher levels. This behavior at low levels indicates that of the shear production term is also being dissipated. The question of whether or not all the shear produced energy is dissipated locally will be approached through height dependence of the residual term D.

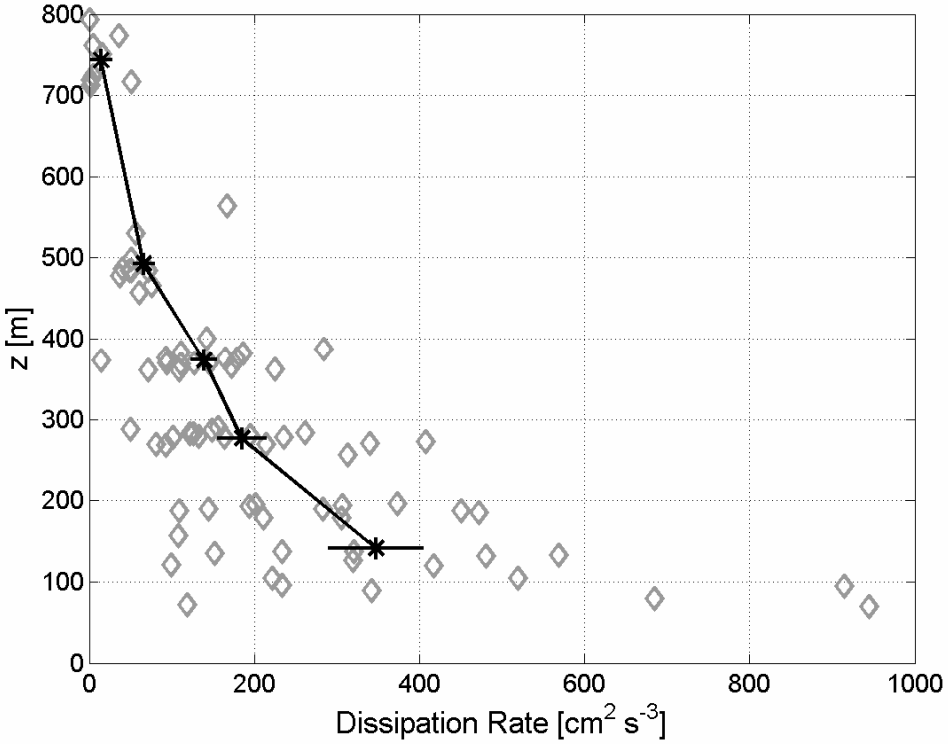

Fig. 6.3. Vertical profiles of the rate of dissipation. Black lines show the averages of the rate of dissipation and one standard error.

6.2.4 The TKE Transport

Fig. 6.4 illustrates the gradually decrease of TKE flux <*w'e'*> with increasing altitude. The TKE transport term represents the flux divergence of TKE for a layer since it depends on the vertical gradient of the TKE flux. So, for a given layer, if more flux in entering the layer than leaving it, there is a net convergence of the vertical flux, and therefore, the TKE of the layer will increase. The TKE transport term is calculated based on the TKE flux data, and found to be small as shown in Fig. 6.5.

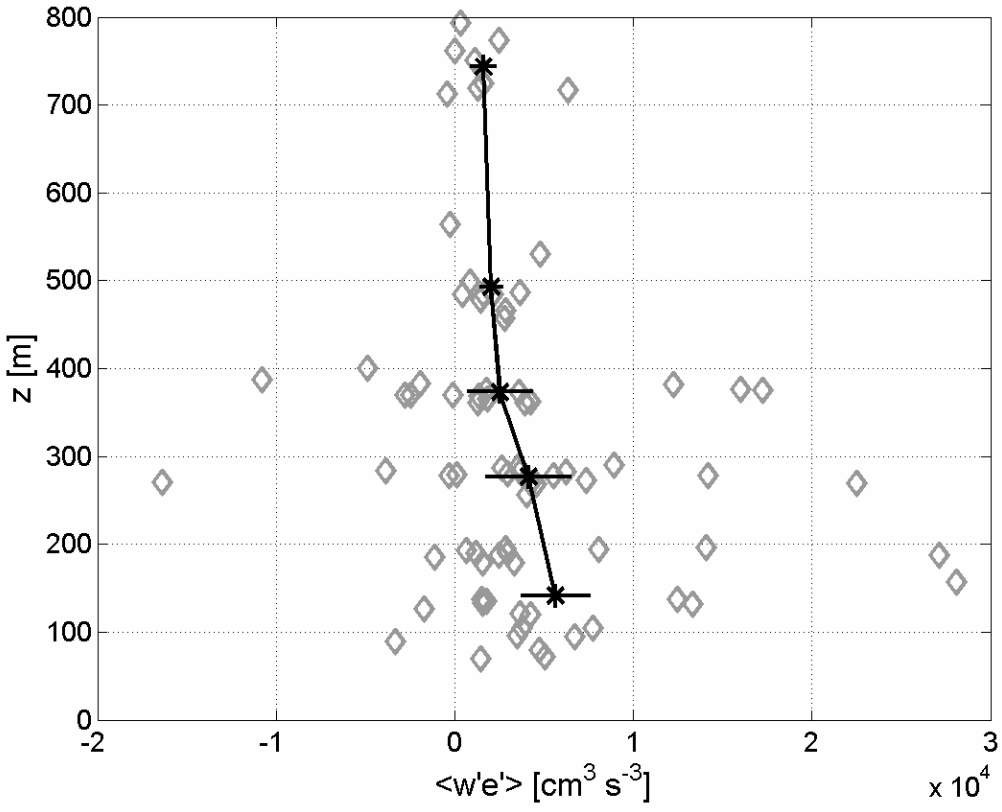

Fig. 6.4. Vertical profiles of the TKE flux <*w'e'*>. Black lines show the averages of the TKE fluxes and one standard error.

6.3 The TKE Budget

The TKE is one of the most important variables since it measures the intensity of turbulence. It is directly related to the momentum, heat and moisture transport from the surface through the boundary layer. Combining the previous discussions of the terms in the TKE budget equation, Fig. 6.5 shows the TKE budgets of the boundary layer in the rain free region between the rainbands. Here data from the boundary layer flights of 2003 and 2004 hurricane seasons are used. The residual term is calculated by subtracting the rest terms from the rate of dissipation, assuming the TKE balance.

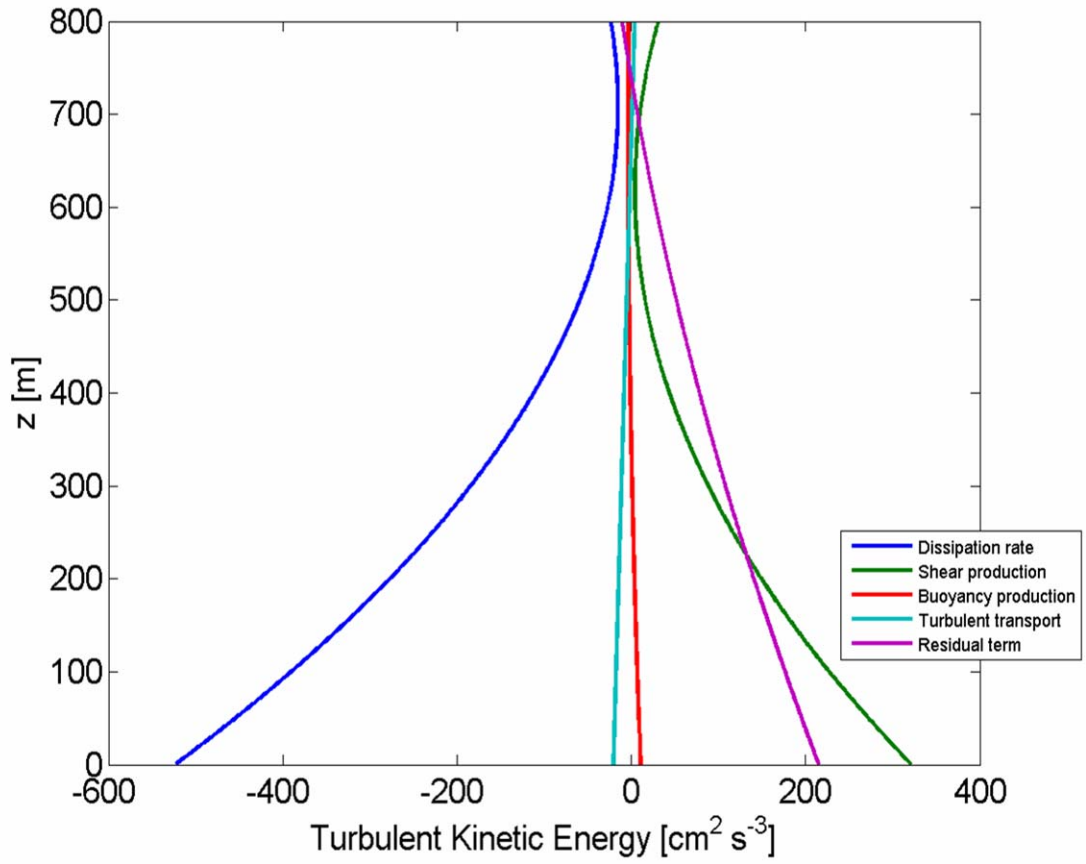

Fig. 6.5. Vertical profiles of shear production, buoyancy, turbulent transport, rate of dissipation and the residual term of the TKE budget.

From Fig. 6.5, the TKE budget is primarily dominated by the shear production and the buoyancy is nearly zero confirming the near-neutrality of the boundary layer. It is also found that the dissipation term is larger than the shear production, indicating the residual term is relatively large compared to previous measurements. The pressure transport term is usually assumed to be small, but it is shown here that the sum of pressure transport term and the nonlinear local transport term are the important source for the turbulent kinetic energy. That is to say the hurricane boundary layer is not ideally homogeneous even in the rain free region between the rainbands. Mesoscale structures such as roll vortices (discussed ealier) could contribute the turbulent transport and may be put into the parameterization of the boundary layer flux and vertical mixing as discussed in Chapter 4. Dissipation heating could also be another energy source to intensify hurricanes (Bister and Emanuel, 1998).

Chapter 7

Summary of Conclusions

7.1 Conclusions

The CBLAST dataset has provided the first direct turbulent flux measurements for hurricane conditions with wind speed higher than 20 m s^{-1} up to 30 m s^{-1}, the first investigation of the turbulence structure in the hurricane boundary layer in the hurricane force wind regime, the first study of hurricane boundary layer rolls using in-situ flight level data, and the first estimate of the turbulent kinetic energy budget for the atmospheric boundary layer between the outer rainbands. The main conclusions of this dissertation are as follows:

1. Direct measurements of turbulent fluxes were made in the boundary layer of major hurricanes; Bulk parameterizations of momentum and enthalpy fluxes were extended up to near hurricane force winds; The C_Ds estimated from this work show a leveling off with wind speed near 25 m s^{-1}, which is a considerably lower threshold than the 33 m s^{-1} value of Donelan et al. (2004); The C_Ks are constant with wind speed up to hurricane force with a value of 0.00115, in close agreement with modified HEXOS and

COARE 3.0 estimates; The resulting C_K/C_D ratio of about 0.7 is significantly less than the Emanuel threshold of 0.75 for hurricane development.

2. The vertical structure of turbulence and fluxes are presented for the entire boundary layer in the rain free region between the outer rainbands. The alongwind component of momentum flux decreases linearly with height, while the crosswind component of momentum flux has a curvature with a maximum value at the height of the mixed layer. The humidity flux is nearly constant with height within the mixed layer and decreases with increasing height above that. The sensible heat flux increases linearly with decreasing height in the mixed layer, and is mostly negative above 0.2 z/zi, where z_i is the mixed layer height.

3. The depth of the layer in which turbulent mixing was observed defined from the turbulent flux profiles is nearly twice the height of the mixed layer defined using the thermodynamic profiles.

4. Measurements of terms in the turbulent kinetic energy budget imply that the major source, the shear production, is dissipated locally with the buoyancy and turbulent transport terms unimportant. The budget indicated that the sum of the production terms is smaller than the dissipation term. That means the unmeasured terms (i.e. advection term) are also important for the generation of turbulent kinetic energy in the hurricane boundary layer.

5. Universal spectra and cospectra normalized following the methods discussed by Miyake et al. (1970) are confirmed, indicating the measurements of turbulence in the hurricane boundary layer between the rainbands follows the standard Monin-Obukhov scaling laws.

6. Boundary layer rolls rescale the sensible heat flux transport and enhance the momentum flux transport about 30%, well below the prediction of Morrison et al. (2005).

7.2 A Conceptual Model for the Hurricane Boundary Layer Height

As discussed in Chapter 1, the boundary layer height is a crucial parameter in numerical models. The height of atmospheric boundary layer represents the height at which turbulent fluxes vanish, i.e., above the boundary layer geostrophic balance or gradient balance (in hurricanes) can be assumed. In numerical models, the atmospheric boundary layer height also determines the upper and lower limits for numerical stability. In the boundary layer schemes used in numerical models, the atmospheric boundary layer height is related to the formation and maintenance of the low level clouds and the vertical transport of heat, moisture and turbulent kinetic energy.

In numerical models, the atmospheric boundary layer height (h) is generally defined as follows: 1). If the boundary layer is unstable or nearly neutral, h is generally defined as the height of the lowest inversion in the potential temperature profile or the lowest cloud base; 2). If the boundary layer is stable, h is usually defined as the height (starting from near surface) where the bulk Richardson number first becomes greater than a critical value, typically around 0.3 (Vogelezang and Holtslag, 1996). However, no matter how the boundary layer height is defined, h represents the height where the influence of the surface friction is negligible.

In this study, the turbulent fluxes of momentum and enthalpy were directly measured for the hurricane boundary layer between the outer rainbands. Thus the boundary layer height can be determined directly from the flux profiles. Since mean profiles are also measured using both the flight level and dropsonde data, the boundary layer height defined using the potential temperature profile can also be calculated. Moreover, using the CBLAST data, the scaling parameter for the boundary layer height that is used in theoretical or numerical models can be computed.

Fig. 7.1 shows a schematic conceptual model for the hurricane boundary layer height for the rainfree region between the outer rainbands. In Fig. 7.1, h_i represents the boundary layer height in the idealized slab model such as used by Emanuel (1986); the black h represents the boundary layer height defined using the flux profile; h_{inflow} represents the inflow layer height; z_i is the boundary layer height defined using the potential temperature profile, and is also called the mixed layer depth; and δ is the scaling depth used in the theoretical models. Here, δ is defined as the square root of the ratio of $2K$ over I, where K is the eddy viscosity and I is the inertial instability parameter, and $I^2 = (f + 2V/r)(f + V/r + \partial V/\partial r)$. The inflow layer height is defined using the radial wind velocity (V_r) profile as the height at which V_r=0. The inflow is essentially caused by the imbalance between the horizontal pressure gradient, Coriolis force, centrifugal force and surface friction.

All the boundary layer height scales in Fig. 7.1 are calculated using the CBLAST data. Fig. 7.1 indicates that the height scales for the boundary layer between the rainbands show differences between each other. There is a clear separation of boundary layer layers defined thermal-dynamically and mechanically, respectively. The turbulent

fluxes do not vanish at the top of the mixed layer; instead, they tend to vanish at nearly twice z_i. On the other hand, the height scales show similarities for the mixed layer depth and the scaling parameter δ, and, separately, for the boundary height defined using the flux profile and the inflow layer height.

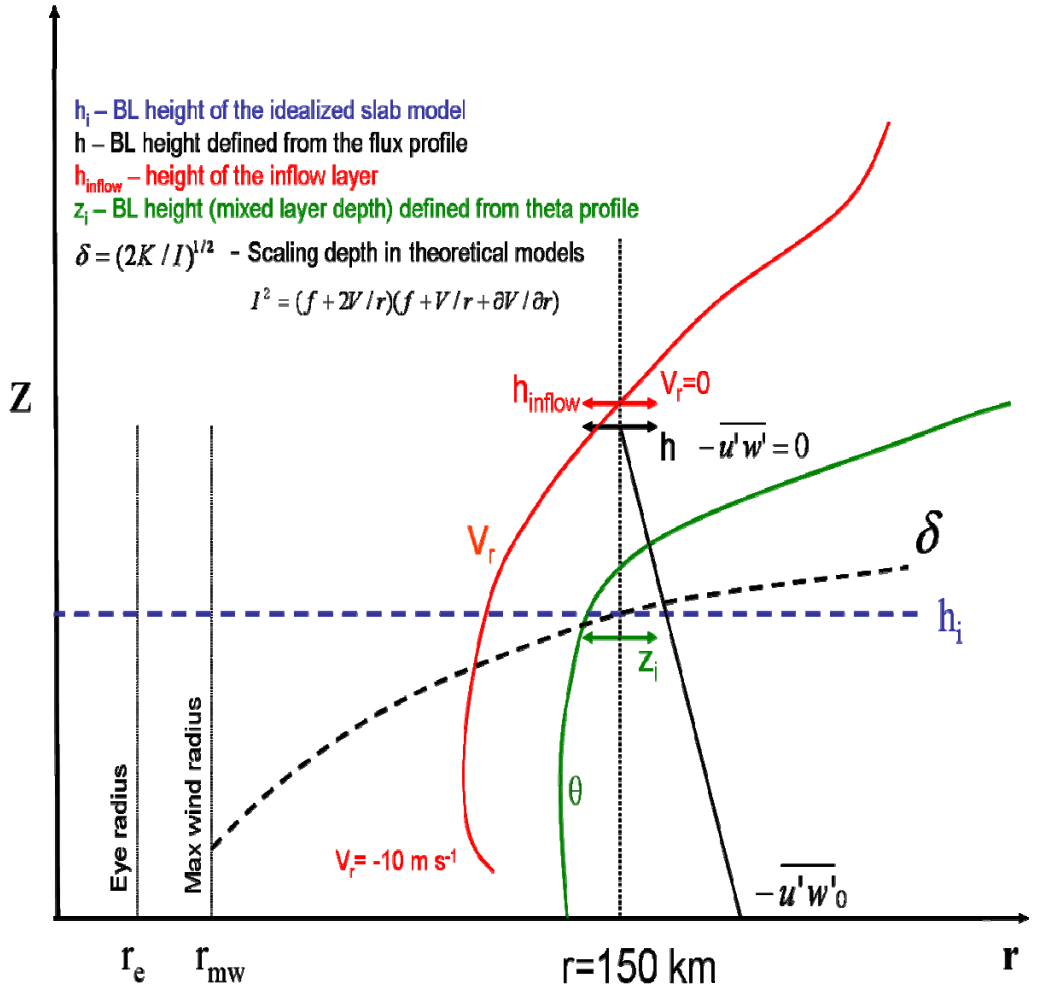

Fig. 7.1. A conceptual model for the hurricane boundary layer height between the rainbands. h_i represents the boundary layer height in the idealized slab model; black h represents the boundary layer height defined using the flux profile; h_{inflow} represents the inflow layer height; z_i is the boundary layer height defined using the potential temperature profile, and is also called the mixed layer depth; and δ is the scaling depth used in the theoretical models.

Both the differences and similarities in the height scales defined in Fig. 7.1 indicate the complicated energy transport processes in the boundary layer of major hurricanes. Apparently turbulent transport processes through turbulent eddies in the forms of momentum and enthalpy flux can not be fully explained only by the exchange coefficients. Other processes such as boundary layer rolls or entrainment processes are also important; especially the horizontal advection can not be neglected as shown by the turbulent kinetic energy budget in Chapter 6.

Dropsonde data analyses focusing on the variation of the mixed layer depth and the inflow layer height by storm radius indicate that they both decrease toward the storm center. This behavior is also confirmed by the numerical model study of Kepert (2001, 2006). In numerical models where model scales could not resolve the smaller scale turbulent eddies, the mixed layer depth is usually assumed to be same as the boundary layer height. But the CBLAST data indicate that this assumption is not valid in the hurricane conditions. We hypothesize that the inflow layer height is a better representation of the boundary layer height in hurricanes. Given that the turbulent fluxes vanish at z_i in the ambient flow of hurricanes (Moss, 1978), a second hypothesis of this work is that the inflow layer height and the mixed layer depth may coincide there, as shown in Fig. 7.2.

There are several question marks in Fig. 7.2, which indicate that some physical processes not well understood until now. These include the variation of the boundary layer height near the rainband regions, turbulent transport processes near the eye wall region, and the entrainment processes at the top of the boundary layer, etc. Moreover, in hurricane conditions, the sea surface is covered by sea spray especially at higher wind

speeds. Although we show that the sea spray effect on the air-sea exchange coefficients for momentum and enthalpy transfer is not significant up to 30 m s^{-1}, the magnitude of the sea spray effect on air-sea exchange coefficients at higher wind speed is still unknown. We need more field experiment to address all these questions. Fortunately, the CBLAST experiment provided a successful framework for us to follow in the future to investigate the hurricane boundary layer structure and to understand the complex energy transport processes near the air-sea interface across the boundary layer at higher wind speeds.

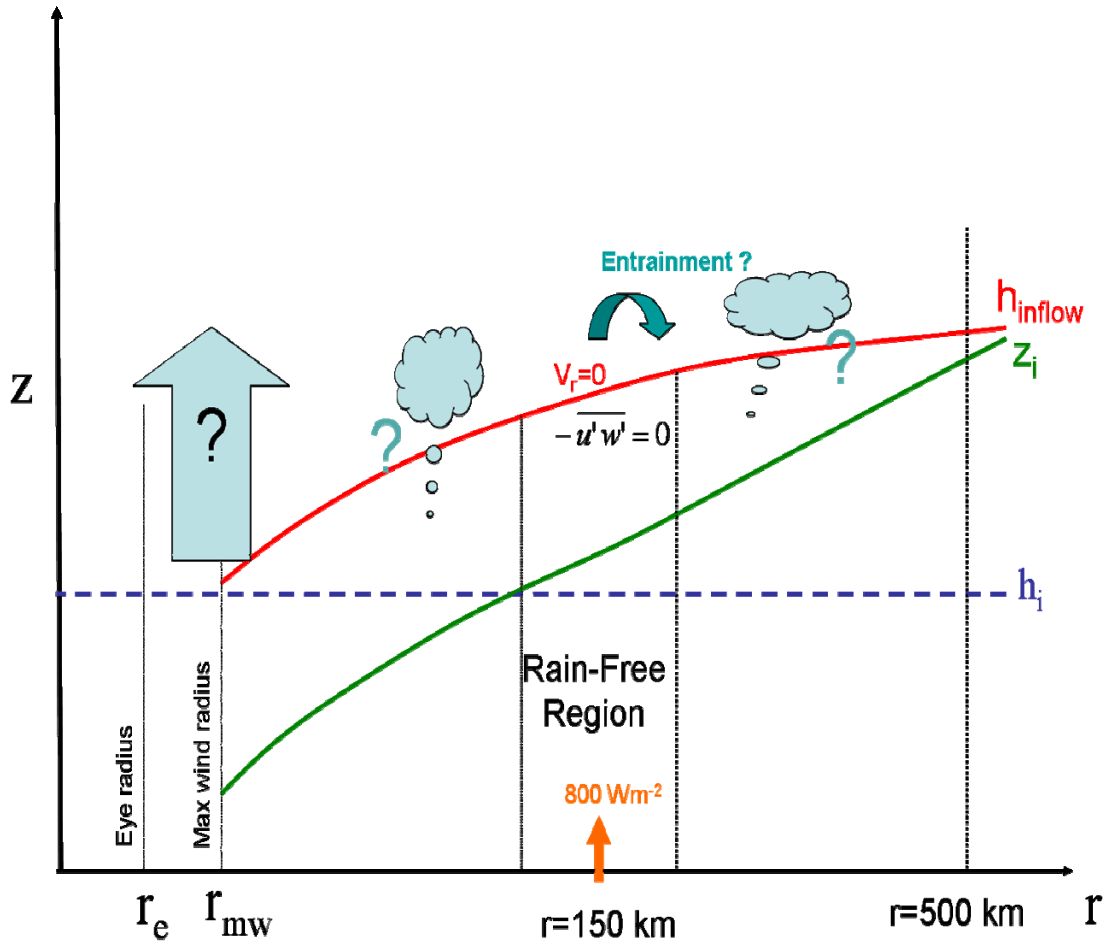

Fig. 7.2. A conceptual model for the hurricane boundary layer height varying with storm radius. h_i represents the boundary layer height in the idealized slab model; h_{inflow} represents the inflow layer height; and z_i is the boundary layer height defined using the potential temperature profile, and is also called the mixed layer depth. Question marks indicate the processes not understood.

7.3 Future work

The CBLAST data provided an invaluable perspective on the evaluation and development of boundary layer parameterizations suited for the hurricane models. These unique datasets could partially meet the requirements for the new generation of advanced coupled models for data in the hurricane at the air-sea interface and the atmospheric boundary layer. Integration of the existing and anticipated CBLAST results on air-sea flux parameterizations into high resolution coupled hurricane models such as Chen et al. (2007), as well as the new HWRF models, is promising.

To verify the bulk parameterization of the exchange coefficients for momentum and enthalpy flux in higher wind speed, measurements from unmanned aircraft deployed aerosonde may help increase the number of flux runs for statistical analysis and quality control. Work will continue on the diagnosis of boundary layer linear features (possible secondary circulations or roll vortices) and their role in air-sea fluxes, including variability by storm quadrant. Studies on entrainment processes above the mixed layer and turbulent transport processes induced by the inflow are also recommended in the future.

Bibliography

Aberson, S. D., M. L. Black, R. A. Black, R. W. Burpee, J. J. Coine, C. W. Landsea and F. D. Marks Jr., 2006: Thirty years of tropical cyclone research with the NOAA P-3 aircraft. *Bull. Amer. Meteorol. Soc.,* **87**, 1039-1055.

Alpers, W., and B. Brümmer, 1994: Atmospheric boundary layer rolls observed by the synthetic aperture radar aboard the ERS-1 satellite. *J. Geophys. Res.*, **99**, 12,613-12,621.

Amorocho, J., and J. J. DeVries, 1980: A new evaluation of the wind stress coefficient over water surfaces. *J. Geophys. Res.*, **85**, 433–442.

Andreas, E. L., and K. A. Emanuel, 2001: Effects of sea spray on tropical cyclone intensity. *J. Atmos. Sci.*, **58**, 3741-3751.

Anthes, R. A., 1971: Iterative solutions to the steady-state axisymmetric boundary layer equations under an intense pressure gradient. *Mon. Wea. Rev.*, **99**, 261-268.

Anthes, R. A., 1974: The dynamics and energetics of mature tropical cyclones. *Rev. Geophys. Space Phys.*, **12,** 495-522.

Anthes, R. A., and S. W. Chang, 1978: Response of the hurricane boundary layer to changes of sea surface temperature in a numerical model, *J. Atmos. Sci.* **35**, 1240–1255.

Banner, M. L., W. Chen, E. J. Walsh, J. B. Jensen, S. Lee, and C. Fandry, 1999: The Southern Ocean Waves Experiment. Part I: Overview and mean results. *J. Phys. Oceanogr.*, **29,** 2130-2145.

Barnes, G. M., and P. B. Bogner, 2001: Comments on 'Surface observations in the hurricane environment'. *Mon. Wea. Rev.*, **129**, 1267–1269.

Barnes, G. M., and G. J. Stossmeister, 1986: The structure and decay of a rainband in Hurricane Irene (1981). *Mon. Wea. Rev.*, **114**, 2590–2601.

Barnes, G. M., E. J. Zipser, D. P. Jorgensen and F. D. Marks, Jr., 1883: Mesoscale and convective structure of a hurricane rainband. *J. Atmos. Sci*, **40,** 2125-2137.

Bister, M., and K. A. Emanuel, 1998: Dissipative heating and hurricane intensity. *Meteor. Atmos. Physi.*, **50**, 233-240.

Black, P. G., E. D'Asaro, W. M. Drennan, J. R. French, P. P. Niiler, T. B. Sanford, E. J. Terrill, E. J. Walsh and J. A. Zhang, 2007: Air-sea exchange in hurricanes: Synthesis of observations from the Coupled Boundary Layer Air-Sea Transfer experiment. *Bull. Amer. Meteorol. Soc.,* **88**, 357-374.

Black, P. G. and Holland, G. J., 1995: The boundary layer of tropical cyclone Kerry (1979). *Mon. Wea. Rev.*, **123**, 2007-2028.

Blackadar, A. K., 1976: Modeling the nocturnal boundary layer. Preprints, *Third Symp. on Atmospheric Turbulence, Diffusion, and Air Quality,* Raleigh, NC, Amer. Meteor. Soc., 46–49.

Blackadar, A. K., 1979: High resolution models of the planetary boundary layer. *Advances in Environmental Science and Engineering,* J. Pfafflin and E. Ziegler, Eds., Vol. 1, No. 1, Gordon and Breach, 50–85.

Bode, L., and R. K. Smith, 1975: A parameterization of the boundary layer of a tropical cyclone. *Boundary-Layer Meteorology*, **8**, 3-19.

Braun S. A., and W.-K., Tao, 2000: Sensitivity of high-resolution simulations of hurricane Bob (1991) to planetary boundary layer parameterizations. *Mon. Wea. Rev.*, **128**, 3941–3961.

Brooks, I. M., and D. P. Rogers, 1997: Aircraft Observations of boundary layer rolls off the coast of California. *J. Atmos. Sci.,* **54**, 1834-1849.

Brown, R. A., 1970: Seven-day flow model for the planetary boundary layer. *J. Atmos. Sci.*, **27**, 742-757.

Brown, R. A., 1980: Longitudinal instabilities and secondary flows in the planetary boundary layer: a review. *Rev. Geophys. Space Phys.*, **18**, 683-697.

Brown, E. N., C. A. Friehe, and D. H. Lenschow, 1983: The use of pressure fluctuations on the nose of an aircraft measuring air motion. *J. Climate App. Meteor.*, **22**,171-180.

Brümmer, B., 1999: Roll and Cell convection in winter-time arctic cold-air outbreaks. *J. Atmos. Sci.,* **29**, 850-895.

Burns, S. P., and Coauthors, 2000: Comparisons of aircraft, ship and buoy radiation and SST measurements from TOGA COARE. *J. Geophys. Res.*, **101,** 12 001-12 016.

Busch, N. E., 1973: *On the mechanics of atmospheric turbulence.* In D. A. Haugen (ed.), Workshop on Micrometeorology, Amer. Meteorolo. Soc., 1-65.

Businger, J.A., J. C. Wyngaard, Y, K. Izumi, and E. F. Bradley, 1971: Flux-profile relationships in the atmosphere surface layer. *J. Atmos. Sci*, **28**, 181-189.

Burk, S. D., and W. T. Thompson, 1989: A vertically nested regional numerical weather prediction model with second-order closure physics. *Mon. Wea. Rev.,* **117,** 2305–2324.

Charnock, H., 1955: Wind Stress on a water surface. *Quart. J. Roy. Meteor. Soc.*, **81**, 639-640.

Chang, S. W., and R. A. Anthes, 1979: The mutual response of the tropical cyclone and the ocean. *J. Phys. Oceanogr.,* **9,** 129-135.

Chen, W., M. L. Banner, E. J. Walsh, J. Jensen, and S. Lee, 2001: The Southern Ocean Waves Experiment, part II, Sea surface response to wind speed and wind stress variations. *J. Phys. Ocean*., **31,** 174-198.

Chen, S. S., J. F. Price, W. Zhao, M. A. Donelan, and E. J. Walsh, 2007: The CBLAST-Hurricane Program and the next-generation fully coupled atmosphere-wave-ocean models for hurricane research and prediction. *Bull. Amer. Meteor. Soc*, **88**, 311-317.

Chou, S.-H., and M. D., Ferguson, 1991: Heat fluxes and roll circulations over the Western Gulf Stream during an intense cold-air outbreak. *Boundary-Layer Meteorology*, **55**, 255-282.

Cione, J. J., P. G. Blasck and S. H. Houston, 2000: Surface Observation in hurricane environment. *Mon. Wea. Rev.*, **128**, 1550-1561.

Crawford, T. L., and R. J. Dobosy, 1992: a sensitive fast-response probe to measure turbulence and heat flux from any airplane. *Boundary-Layer Meteorology*, **59**, 257-278.

Deardorff, J. W., 1972: Parameterization of the planetary boundary layer for use in general circulation models. *Mon. Wea. Rev.,* **100,** 93–106.

DeCosmo, J., K.B. Katsaros, S. D. Smith, R. J. Anderson, W.A. Oost, K. Bumke, and H. Chadwick, 1996: Air-sea exchange of water and sensible heat: The Humidity Exchange over the Sea (HEXOS) results. *J.Geophys. Res.*, **101**, 12,001-12,016.

Donelan, M.A., and M. Miyake, 1973: Spectra and fluxes in the boundary layer of the Trade-wind zone. *J. Atmos. Sci*, **30**, 444-464.

Donelan, M.A., 1990: Air-Sea Interaction. *The Sea: Ocean Engineering Science*, 9, eds. B. LeMéhauté and D. Hanes, John Wiley and Sons, Inc., New York, 239-292.

Donelan, M. A., F. W. Dobson, S. D. Smith, and R. J. Anderson, 1993: On the dependence of sea surface roughness on wave development. *J. Phys. Oceanogr.*, **23**, 2143-2149.

Donelan, M. A., and W. M. Drennan, 1995: Direct field measurements of the flux of carbon dioxide. In: *Air-water gas transfer*, (Eds. B. Jähne and E.C. Monahan), Aeon-Verlag, 677-683.

Donelan, M. A., W. M. Drennan, and K. B. Katsaros, 1997: The air-sea momentum flux in mixed wind sea and swell conditions. *J. Phys. Oceanogr.*, **27**, 2087-2099.

Donelan, M. A., B. K. Haus, N. Reul, W. J. Plant, M. Stiassnie, H. C. Graber, O. B. Brown, and E. S. Saltzman, 2004: On the limiting aerodynamic roughness of the ocean in very strong wind. *Geophys. Res.Lett.*, **31**, L18306, doi: 10.1029/2004GL019460.

Drennan, W. M., H. C. Graber, D. Hauser, and C. Quentin, 2003: On the wave age dependence of wind stress over pure wind seas, *J.Geophys. Res.*, **108(C3)**, 8062, doi: 10.1029/2000JC000715.

Drennan, W. M., K. K. Kahma, and M. A. Donelan, 1999: On momentum flux and velocity spectra over waves, *Boundary-Layer Meteorology*, **92**, 489-515.

Drennan, W. M., and L. K. Shay, 2006: On the variability of the fluxes of momentum and sensible heat. *Boundary-Layer Meteorology*, **119**, 81-107.

Drennan, W.M., P. K. Taylor, and M. J. Yelland 2005: Parameterizing the sea surface roughness, *J. Phys. Oceanogr.*, **35**, 835-848.

Dudhia, J., 1993: A nonhydrostatic version of the Penn State–NCAR mesoscale model: Validation tests and simulation of an Atlantic cyclone and cold front. *Mon. Wea. Rev.,* **121,** 1493–1513.

Dyer, A. J, and B. B. Hicks, 1970: Flux-gradient relationships in the constant flux layer. *Quart. J. Roy. Meteor. Soc.*, **96**, 715-721.

Eliassen, A., 1971: On the Ekman layer in a circular vortex. *J. Meteorol. Soc. Jpn.*, **49**, 784-789.

Eliassen, A. and M. Lystad, 1977: The Ekman layer in a circular vortex: A numerical and theoretical study. *Geophysical Norvegica,* **31,** 1-16.

Etling, D., and R. A. Brown, 1993: Roll vortices in the planetary boundary layer: a review. *Boundary-Layer Meteorology*, **65**, 215-248.

Emanuel, K. A., 1986: An Air-Sea Interaction Theory for Tropical Cyclones. Part I: Steady-State Maintenance. *J. Atmos. Sci*, **43**, 585-605.

Emanuel, K.A., 1991: A scheme for representing cumulus convection in large-scale models. *J. Atmos. Sci.*, **48**, 2313-2335.

Emanuel, K. A., 1995: Sensitivity of tropical cyclones to surface exchange coefficients and a revised steady-state model incorporating eye dynamics. *J. Atmos. Sci*, **52**, 3969-3976.

Emanuel, K.A., 1999: Thermodynamic control of hurricane intensity. *Nature*, **401**, 665-669.

Emanuel, K. A., 2000: A statistical analysis of hurricane intensity. *Mon. Wea. Rev.*, **128**, 1139-1152.

Emanuel, K., 2003: A similarity hypothesis for air-sea exchange at extreme wind speeds. *J. Atmos. Sci.*, **60**, 1420-1428.

Emanuel, K., 2003: Tropical cyclones. *Ann. Rev. Earth Planet. Soc.*, **31**, 75-104.

Fairall, C. W., E. F. Bradley, D. P. Rogers, J. B. Edson, and G. S. Young, 1996: Bulk parameterization of air-sea fluxes for tropical ocean-global atmosphere coupled-ocean atmosphere response experiment. *J. Geophys. Res.*, **101**, 3747-3764.

Fairall, C. W., E. F. Bradley, J. E. Hare, A. A. Grachev and J. B. Edson, 2003: Bulk parameterization of air-sea fluxes: updates and verification for the COARE algorithm. *J. Climate*, **16**, 571-591.

Farge, M., 1992: Wavelet transforms and their applications to turbulence. *Annual Review of Fluid Mechanics*, **24**, 395-458.

Foster, R.C., 2005: Why rolls are prevalent in the hurricane boundary layer. *J. Atmos. Sci.*, **62**, 2647-2661.

Franklin, J. L., M. L. Black, and K. Valde, 2003: GPS dropwindsonde wind profiles in hurricanes and their operational implications. *Wea. Forecasting,* **18,** 32–44.

French, J. R., W. M. Drennan, J. A. Zhang and P.G. Black, 2007: Turbulent fluxes in the hurricane boundary layer. Part I: Momentum flux. *J. Atmos. Sci.,* **63***,* 1089-1102.

Friedman, K. S., P. W. Vachon, and K. B. Katsaros, 2004: Mesoscale storm systems. In *SAR Marine Users Manual*, Chapter 15.

Friehe, C. A., and D. Khelif, 1992: Fast-response aircraft temperature sensors. *J. Atmos.Oceanic Technol.*, **9**, 784-795.

Friehe, C. A., W. J. Shaw, D. P. Rogers, K. L. Davidson, W. G. Large, S. A. Stage, G. H. Crescenti, S. J. S. Khalsa, G. K. Greenhut, and F. Li, 1991: Air-sea fluxes and surface turbulence around a sea surface temperature front. *J. Geophys. Res.,* **96(C5)**, 8593-8609.

Fujita, T. T., 1992: Damage survey of Hurricane Andrew in south Florida. *Storm Data,* Vol. 34, No. 8, 176pp.

Geernaert G. L., K. L. Davidson, S. E. Larsen, and T. Mikkelson, 1988: Wind stress measurements during the Tower Ocean Wave and Radar Dependence Experiment. *J. Geophys. Res.*, **93,** 13913–13923.

Glendening, J. W., 1996: Linear eddy features under strong shear conditions. *J. Atoms. Sci.*, **53**, 3430-3449.

Grachev A. A., C. W. Fairall, J. E. Hare, J. B. Edson, and S. D. Miller, 2003: Wind stress vector over ocean waves. *J. Phys. Oceanogr.*, **33,** 2408–2429.

Grell, G. A., J. Dudhia, and D. R. Stauffer, 1995: A description of the fifth-generation Penn State/NCAR Mesoscale Model (MM5). *NCAR Tech. Note*, NCAR/TN-398 1 STR, 122 pp.

Grossmann, A., and J. Morlet, 1984: Decomposition of Hardy functions into square integrable wavelets of constant shape. *Siam J. Math. Anal.,* **15**, 723-736.

Hacker, J. M, and T. L. Crawford, 1999: The BAT-probe: The ultimate tool to measure turbulence from any kind of aircraft (or sailplane), *J. Technic. Soaring*, **23**, 43-46.

Hawkins, H. F., and D. T. Rubsam, 1968: Hurricane Hilda Part II: structure and budgets of the Hurricane on 1 Oct. 1964, *Mon. Wea. Rev.*, **96**, 617-636.

Hock, T. F., and J. L. Franklin, 1999: The NCAR GPS dropwindsonde. *Bull. Amer. Meteor. Soc.,* **80,** 407–420.

Högström, U., 1988: Nondimensional wind and temperature profiles in the atmospheric surface layer: A reevaluation. *Boundary-Layer Meteorology*, **42**, 55-78.

Högström, U., 1996: Review of some basic characteristics of the atmospheric surface layer. *Boundary-Layer Meteorology*, **78**, 215-246.

Hong, S.-H., and H.-L. Pan, 1996: Nonlocal boundary layer vertical diffusion in a medium-range forecast model. *Mon. Wea. Rev.,* **124,** 2322–2339.

Janssen, J. A. M., 1997: Does wind stress depend on sea state or not? A statistical error analysis of HEXMAX data. *Boundary-Layer Meteorology*, **83**, 479-503.

Johnson, H. K., J. Hojstrup, H. J. Vested, and S. E. Larsen, 1998: On the dependence of sea surface roughness on wind waves. *J. Phys. Oceanogr.*, **28**, 1702-1716.

Jorgensen, D. P., 1984: Mesoscale and convectivescale characteristics of mature hurricanes. Part 1: general oberservations by research aircraft. *J. Atmos. Sci*, **41**, 1268-1285.

Kaimal, J. C., and J. J. Finnigan, 1994: *Atmospheric Boundary Layer Flows*. Oxford University Press, 10-56 pp.

Kaimal, J. C., J. C. Wyngaard, D. A. Haugen, O. R. Coté, Y. Izumi, S. J. Caughey, and C. J. Readings, 1976: Turbulence structure in the convective boundary layer, *Ibid,* **33,** 2152-2169.

Kaimal, J. C., J. C. Wyngaard, Y. Izumi, and O. R. Coté, 1972: Spectral characteristics of surface-layer turbulence. *Quart. J. Roy. Meteor. Soc.*, **98,** 563-589.

Katsaros, K. B., M. A. Donelan and W. M. Drennan, 1993: Flux measurements from a Swath ship in SWADE. *J. Mar. Sys.* **4**, 117-132.

Katsaros, K.B., P.W. Vachon, P. G. Black, P. P. Dodge, and E. W. Uhlhorn, 2000: Wind fields from SAR: Could they improve our understanding of storm dynamics? *Johns Hopkins APL Technical Digest*, **21**(1), 86-93.

Katsaros, K.B., P.W. Vachon, W.T. Liu, and P.G. Black, 2002: Microwave remote sensing of tropical cyclones from space. *J. of Oceanography*, **58**, 137-151.

Kepert, J. D., 2001: The dynamics of boundary layer jets within the tropical cyclone core. Part I: Linear theory. *J. Atmos. Sci*, *J. Atmos. Sci*, **58**, 2469-2484.

Kepert, J. D., 2006: Observed boundary layer wind structure and balance in the Hurricane core. Part I: Hurricane Georges. *J. Atmos. Sci*, **63**, 2169-2192.

Kepert, J. D. and Y. Wang, 2001: The dynamics of the boundary layer jets within the tropical cyclone core. Part II: Nonlinear enhancement. *J. Atmos. Sci*, **58**, 2485-2501.

Khelif, D., S. P. Burns, and C. A. Friehe, 1999: Improved wind measurements on research aircraft. *J. Atmos. Oceanic Technol.*, **16**, 860-875.

Koch, W., 2004: Directional analysis of SAR images aiming at wind direction. *IEEE Trans. Geosci. Remote Sens.,* **42,** 702–710.

Kraus, E. B., and J. A. Businger, 1994: *Atmosphere-Ocean Interaction*, 49-55 pp.

Kurihara, Y., R. E. Tuleya, and M. A. Bender, 1998: The GFDL hurricane prediction system and its performance in the 1995 hurricane season. *Mon. Weath. Rev.*, **126**, 1306-1322.

Large, W. G., and S. Pond, 1981: Open ocean momentum flux measurements in moderate to strong winds. *J. Phys. Oceanogr.*, **11**, 324-336.

Laur, H., P. Bally, P. Meadows, S. J. B. Schättler, and E. Lopinto, 1998: Derivation of the backscattering coefficient_0 in ESA ERS- 1/2.SAR.PRI data products. *Tech. Note ES-TN-RSPM- HL09*, issue 2, Revision 5b, ESA, Frascati, Italy, 47 pp.

Lehner, S., J. Horstmann, W. Koch, and W. Rosenthal, 1998: Mesoscale wind measurements using recalibrated ERS SAR images. *J. Geophysi. Resea.*, **103**, 7847- 7856.

Lehner, S., J. Schulz-Stellenfleth, J. B. H. Schtler, H. Breit, and J. Horstmann, 2000: Wind and wave measurements using complex ERS-2 wave mode data. *IEEE Transactions on Geoscience and Remote Sensing*, **38**(5), 2246-2257.

LeMone, M. A., 1973: The structure and dynamics of horizontal roll vortices in the planetary boundary layer. *J. Atmos. Sci.*, **20**, 1077-1091.

LeMone, M. A., 1976: Modulation of turbulent energy by longitudinal rolls in an unstable boundary layer. *J. Atmos. Sci.*, **33**, 1308-1320.

Lenschow, D. H., 1986: Aircraft measurements in the boundary layer. *Probing the Atmosphere Boundary Layer,* D. H. Lenschow, Ed., American Meteorological Society, 39-55.

Leslie, L. M., and R. K. Smith, 1970: The surface boundary layer of a hurricane-Part II. *Tellus*, **22,** 288-297.

Levy, G., 2001: Boundary layer roll statistics from SAR. *Geophys. Res. Lett.*, **28(10)**, 1993–1996.

Lilly, D. K., 1966: On the instability of Ekman Boundary Flow. *J. Atmos. Sci.*, **23**, 481-484.

Liu, W. T., K. B. Katsaros, and J. A. Businger, 1979: Bulk parameterization of air-sea exchanges of heat and water vapor including the molecular constraints at the interface. *J. Atmos. Sci*, **36,** 1722-1735.

Mahrt, L., 1998: Flux sampling errors from aircraft and towers. *J. Atmos. Oceanic Technol.*, **15,** 416-429.

Mahrt, L., D. Vickers, W. M. Drennan, H. C. Graber, and T. L. Crawford, 2005: Displacement measurement errors from moving platforms. *J. Atmos. Oceanic Technol.*, **22,** 860-868.

Mann, J., and D. H. Lenschow, 1994: Errors in airborne flux measurements. *J. Geophys. Res.*, **99,** 14 519-14 526.

Malkus, J. S., and H. Riehl, 1960: On the dynamics and energy transformations in steady-state hurricanes. *Tellus,* **12,** 1-20.

Marks, Jr. F. D., and R. A. Houze, 1987: Inner core structure of Hurricane Alicia from airborne Doppler radar observations. *J. Atmos. Sci*, **44,** 1296-1317.

McGillis, W. R., J. B. Edson, C. J. Zappa, J. D. Ware, S. P. McKenna, E. A. Terray, J. E. Hare, C. W. Fairall, W. Drennan, M. Donelan, M. D. DeGrandpre, R. Wanninkhof and R. A. Feely, 2004: Air-sea CO_2 exchange in the equatorial Pacific, *J. Geophys. Res.*, **109**, C08S02, doi:10.1029/2003JC002256.

Mestayer P. G., and C. Lefauconnier, 1988: Spray droplet generation, transport, and evaporation in a wind wave tunnel during the Humidity Exchange over the Sea Experiments in the Simulation Tunnel. *J. Geophys. Res.*, **93**, 572-586.

Miller, B. I., 1964: A study of the filling of Hurricane Donna(1960) over land. *Mon. Weath. Rev.*, **92**, 389-406.

Miyake, M.., Stewart, W., & Burling, R.W., 1970: Spectra and cospectra of turbulence over water. *Quart. J. Roy. Meteor. Soc.*, **96**, 138-143.

Montgomery, M. T., H. D. Snell, and Z.Yang, 2001: Axisymmetric spindown dynamics of hurricane like vortices. *J. Atmos. Sci.*, **58**, 421-435.

Montgomery, M. T., M. M. Bell, S.Aberson, and M. Black, 2006: Hurricane Isabel (2003): New insights into the physics of intense storms. Part I. Mean vortex structure and maximum intensity estimate. *Bull. Amer. Meteorol. Soc.*, **87**, 1335-1347.

Monin, A. S., and A. M. Obukhov, 1954: Basic laws of turbulent mixing in the ground layer of the atmosphere. *Akad. Nauk. SSSR Geofiz. Inst. Tr.* **151**, 163-187.

Morrison, I., S. Businger, F. Marks, P. Dodge, and J.A. Businger, 2005: An observational case for the prevalence of roll vortices in the hurricane boundary layer. *J. Atmos. Sci.*, **62**, 2662-2673.

Moss, M. S., 1978: Low-level turbulence structure in the vicinity of a hurricane. *Mon. Wea. Rev.*, **106**, 841–849.

Moss, M. S. and F. J. Merceret, 1977: A comparison of velocity spectra from hot film anemometer and gust-probe measurements. *J. Appl. Meteo.,* **16**, 319–320.

Moss, M. S. and F. J. Merceret, 1976: A note on several low-layer features of Hurricane Eloise (1975). *Mon. Wea. Rev.*, **104**, 967–971.

Mourad, P. D., 1996: Inferring multiscale structure in atmospheric turbulence using satellite-based synthetic aperture radar. *J. Geophys. Res.,* **101**, 18,433-18,449.

Mourad, P. D., and B. A. Walter, 1996: Viewing a cold air outbreak using satellite-based synthetic aperture radar and advanced very high resolution radiometer imagery. *J. Geophys. Res.,* **101**, 16,391-16,400.

Mourad, P. D., D. R. Thompson, and D. Vandemark, 2000: Extracting fine-scale wind fields from synthetic aperture radar images of the ocean surface. *Johns Hopkins APL Tech. Dig.,* **21**, 108-115.

Müller, G., B. Brümmer, and W. Alpers, 1999: Roll convection within an Arctic cold-air outbreak: interpretation of in situ aircraft measurements and spaceborne SAR imagery by a three-dimensional atmospheric model. *Mon. Wea. Rev.*, **127**, 363-380.

Neuyen, C. M., R. K., Smith, H. Zhu, and W. Ulrich, 2002: A minimal axisymmetric hurricane model. *Quart. J. Roy. Meteorol. Soc.*, **128,** 2641-2661.

Nicholls, S., and C. J. Readings, 1979: Aircraft observations of the structure on the lower boundary layer over the sea. *Quart. J. Roy. Meteor. Soc.*, **105,** 785-802.

Ocampo-Torres, F. J., M. A. Donelan, N. Merzi, and F. Jia, 1994: Laboratory measurements of mass transfer of carbon dioxide and water vapour for smooth and rough flow conditions. *Tellus, Ser. B.*, **46,** 16-32.

Oncley, S. P., and J. Dudhia, 1995: Evaluation of surface fluxes from MM5 using observations. *Mon. Wea. Rev.,* **123,** 3344–3357.

Ooyama, K. V., 1969: Numerical simulation of the life cycle of tropical cyclones. *J. Atmos. Sci*, **26**, 3-40.

Palmen, E., and H. Riehl, 1957: Budget of angular momentum and energy in tropical cyclones, *J. Meteor.*, **14**, 150-159.

Palmen and Newton, 1969: Newton, *Atmospheric Circulation Systems*, Academic Press, New York and London, 51-75 pp.

Panofsky, H. A., 1978: Matching in the convective boundary layer. *J. Atmos. Sci.*, **35,** 272-276.

Panofsky, H. A., H. Tennekes, D. H. Lenschow, and J. C. Wyngaard, 1977: The characteristics of turbulent velocity components in the surface layer under convective conditions. *Boundary-Layer Meteorology*, **11,** 355-361.

Pond, S., R. W. Stewart, and R. W. Burling, 1963: Turbulence spectra in the wind over waves. *J. Atmos. Sci.*, **20,** 319-324.

Powell, M. D., 1980: Evaluation of diagnostic marine boundary layer models applied to hurricanes. *Mon. Wea. Rev.*, **108**, 757-766.

Powell, M. D., 1990: Boundary layer structure and dynamics in outer hurricane rainbands. Part I: Mesoscale rainfall and kinematic structure. *Mon. Wea.Rev.*, **118**, 891-917.

Powell, M. D., 1990: Boundary layer structure and dynamics in outer hurricane rainbands. Part II: Downdraft modification and mixed layer recovery. *Mon. Wea. Rev.*, **118**, 918-938.

Powell, M. D., and P. G. Black, 1984: Airborne Doppler radar observations of the boundary layer of Hurricane Debby (1982). *Preprints, 22nd Conf. on Radar Meteorology,* Zurich, Switz, Amer. Meteor. Soc., Boston, 584-588.

Powell, M. D., T. A. Reinhold, and R. D. Marshall, 1999: in *Proc. 10th Int. Conf. Wind Eng. (Copenhagen, 21-24June)*, (eds Larsen, A., G. L. Larose, and F. M. Livesey), 307-314.

Powell, M. D., Vickery, P. J., and Reinhold, T. A., 2003: Reduced drag coefficient for high wind speeds in tropical cyclones. *Nature*, **422**, 279-283.

Riehl, H., 1954: *Tropical Meteorology*. New York: McGraw-Hill, 392 pp.

Robe, F. R., and K. Emanuel, 2001: The effect of vertical wind shear on radiative-convective equilibrium states. *J. Atmos. Sci*, **58**, 1427-1445.

Rosenthal, S. L., 1962: *A Theoretical Analysis of the Field of Motion in the Hurricane Boundary Layer*, National Hurricane Research Project Rep. 56, Washington, DC, 12 pp.

Rosenthal, S. L., 1971: The response of a tropical cyclone model to variations in boundary layer parameters, initial conditions, lateral boundary conditions and domain size. *Mon. Wea. Rev.*, **99**, 767-777.

Rotunno, R., 1979: A study of tornado-lick vortex dynamics. *J. Atmos. Sci*, **36,** 140-155.

Rotunno, R., and K.A. Emanuel, 1987: An air-sea interaction theory for tropical cyclones, Part II: Evolutionary study using axisymmetric nonhydrostatic numerical model. *J. Atmos. Sci.*, **44**, 542-561.

Rouault, M. P., P. G. Mestayer, and R. Schiestel, 1991: A model of evaporating spray droplet dispersion. *J. Geophys. Res.*, **96**, 7181-7200.

Savtchenko, S., 1999: Effect of large eddies on atmospheric surface layer turbulence and the underlying wave field. *J. Geophys. Res.,* **104**, 3149-3157.

Schade, L. R., 1997: A physical interpretation of SST-feedback. *Preprints of the 22nd Conf. on Hurricanes and Tropical Meteorology*, 439–440.

Schade, L. R., and K. A. Emanuel, 1999: The ocean's effect on the intensity of tropical cyclones: Results from a simple coupled atmosphere-ocean model. *J. Atmos. Sci.*, **56**, 642-651.

Shapiro, L. J., 1983: The asymmetric boundary layer under a translating hurricane. *J. Atmos. Sci*, **40,** 1984-1998.

Shay, L. K., 1999: Upper ocean response to tropical cyclones. *RSMAS Tech. Note*, *99-003*, (University of Miami, Rosenstiel School of Marine and Atmospheric Science, Florida).

Shay, L.K., 2001: Upper Ocean Structure: Response to Strong Forcing Events. In*: Encyclopedia of Ocean Sciences*, ed. R.A. Weller, S.A. Thorpe, J. Steele, Academic Press International, London, UK, 3100 - 3114.

Smith, R. K. 1968: The surface boundary layer of a hurricane. *Tellus*, **20**, 473-483.

Smith, S. D., 1980: Wind stress and heat flux over the ocean in gale force winds. *J. Phys. Oceanogr.*, **10**, 709-726.

Smith, S. D., and R. J. Anderson, 1984: Spectra of humidity, temperature and wind over the sea at Sable Island, Nova Scotia. *J. Geophys. Res.*, **89,** 2 029-2 040.

Smith, S.D., R. J. Anderson, W. A. Oost, C. Kraan, N. Maat, J. DeCosmo, K. B. Katsaros, K. L. Davidson, K. Bumke, L. Hasse and H. M. Chadwick, 1992: Sea surface wind stress and drag coefficients: the HEXOS results. *Boundary-Layer Meteorology* **60**, 109-142.

Sikora, T. D., and S. Ufermann, 2004: Marine atmospheric boundary layer cellular convection and longitudinal roll vortices. *SAR Marine Users Manual*, Chapter 14.

Sreenivasan, K. r., A. J. Chambers, and R. A. Antonia, 1978: Accuracy of moments of velocity and scalar fluctuations in the atmospheric surface layer. *Boundary-Layer Meteorology*, **14,** 341-359.

Stull, R. B., 1988: *An Introduction to Boundary Layer Meteorology.* Kluwer Academic, 1-50 pp.

Tjernström, M., and A.-S Smedman, 1993: The vertical structure of the coastal marine atmospheric boundary layer. *J. Geophys. Res.*, **98**, 4809-4826.

Uhlhorn E. W., and P. G. Black. 2003: Verification of remotely sensed sea surface Winds in hurricanes. *J. Atmos. Oceanic Technol.*, **20**, 99–116.

Uhlhorn, E. W., P. G. Black, J. L. Franklin, M. Goodberlet, J. Carswell, and A. S. Goldstein, 2007: Hurricane surface wind measurements from an operational stepped frequency microwave radiometer. *Mon. Wea. Rev.*, in press.

Vachon, P. W., and K.B. Katsaros, 1999: Atmospheric cyclones from spaceborne SAR. *Backscatter*, **10**(4), 14-19.

Vandemark, D., P. D. Mourad, S. A. Bailey, T. L. Crawford, C. A. Vogel, J. Sun, and B. Chapron, 2001: Measured changes in ocean surface roughness due to atmospheric boundary layer rolls. *J. Geophys. Res.*, **106**(C3), 4639-4654, doi: 10.1029/1999JC000051.

Vogelezang, D. H. P., and A. A. M. Holtslag, 1996: Evaluation and model impacts of alternative boundary-layer height formulations. *Boundary-Layer Meteorology,* **81,** 245–269.

Wakimoto, R. M., and P. G. Black, 1994: Damage survey of Hurricane Andrew and its relationship to the eyewall. *Bull. Amer. Meteor. Soc.*, **75**, 189-200.

Wang, Y., J. D. Kepert, and G. Holland, 2000: On the effect of sea spray evaporation on tropical cyclone boundary-layer structure and intensity. *23rd Conference of Hurricane and Tropical Meteorology*, Dallas, Texas.

Weckwerth, T. M., J. W. Wilson, R. M. Wakimoto, and N. A. Crook, 1997: Horizontal convetive rolls: Determing the environmental conditions supporting their existence and characteristics. *Mon. Wea. Rev.,* **125**, 505-526.

Willoughby, H. E., 1990: Gradient balance in tropical cyclones. *J. Atmos. Sci*, **47,** 265-274.

Willoughby, H. E., J. A. Clos and M. G. Shoreibah, 1982: Concentric eyewalls, secondary wind maxima, and the evolution of the hurricane vortex. *J. Atmos. Sci*, **39,** 395-411.

Wurman, J., and J. Winslow, 1998: Intense sub-kilometer boundary layer rolls in Hurricane Fran. *Science,* **280**, 555-557.

Wyngaard, J. C., 1973: *On surface turbulence, Workshop on micrometeorology*, D. A. Haugen (ed.), *Amer. Met. Soc.*, Boston, Mass., 101-149.

Yelland, M. J., B. I. Moat, P. K. Taylor, R. W. Pascal, J. Hutchings and V. C. Cornell, 1998: Wind stress measurements from the open ocean corrected for airflow distortion by the ship. *J. Phys. Oceanogr.* **28**, 1511-1526.

Young, G. S., D. A. R. Kristovich, M. R. Hjelmfelt, and R. C. Foster, 2002: Rolls, streets, waves, and more: A review of quasi-two-dimensional structures in the atmospheric boundary layer. *Bull. Amer. Meteor. Soc.*, **83**, 997-1001

Zhang, D.-L., and R. A. Anthes, 1982: A high-resolution model of the planetary boundary layer—Sensitivity tests and comparisons with SESAME-79 data. *J. Appl. Meteor.,* **21,** 1594–1609.

Zhang, J., 2005: Humidity flux measurements in hurricane conditions. Master Thesis, University of Miami, 40-61 pp.

VITA

Jun Zhang was born in Fengrun, Hebei Province, P. R. China, on March 20th, 1978. His parents are Guwen Zhang and Cuofeng Cao. His wife is Yuhui Wen. He received his elementary and secondary education at Fengrun, China. He graduated from Dalian University of Technology with a Bachelor Degree of Engineering in Naval Architecture in July 2000. Then he was enrolled to the graduate school of Dalian University of Technology majoring in Computer-aided Manufacture of Naval Architecture without exam. As a graduate student, he volunteered to teach at Qinghai Hualong No. 4 Middle School for a year in a remote and very poor town of Qinghai Province in China. In August 2001, he moved back to Dalian University of Technology and studied there as a graduate research assistance for a year.

In August 2002 he was admitted to the Graduate School of the University of Miami at the Rosenstiel School of Marine and Atmospheric Science where he was granted the degree of Master of Science in Applied Marine Physics in May 2005, and the degree of Doctor of Philosophy in Applied Marine Physics in December 2007.